Preliminary Sizing and Structural Design of a Drag Sail Deorbiting System for CubeSats in Low Earth Orbit

Claudia Rodríguez del Río

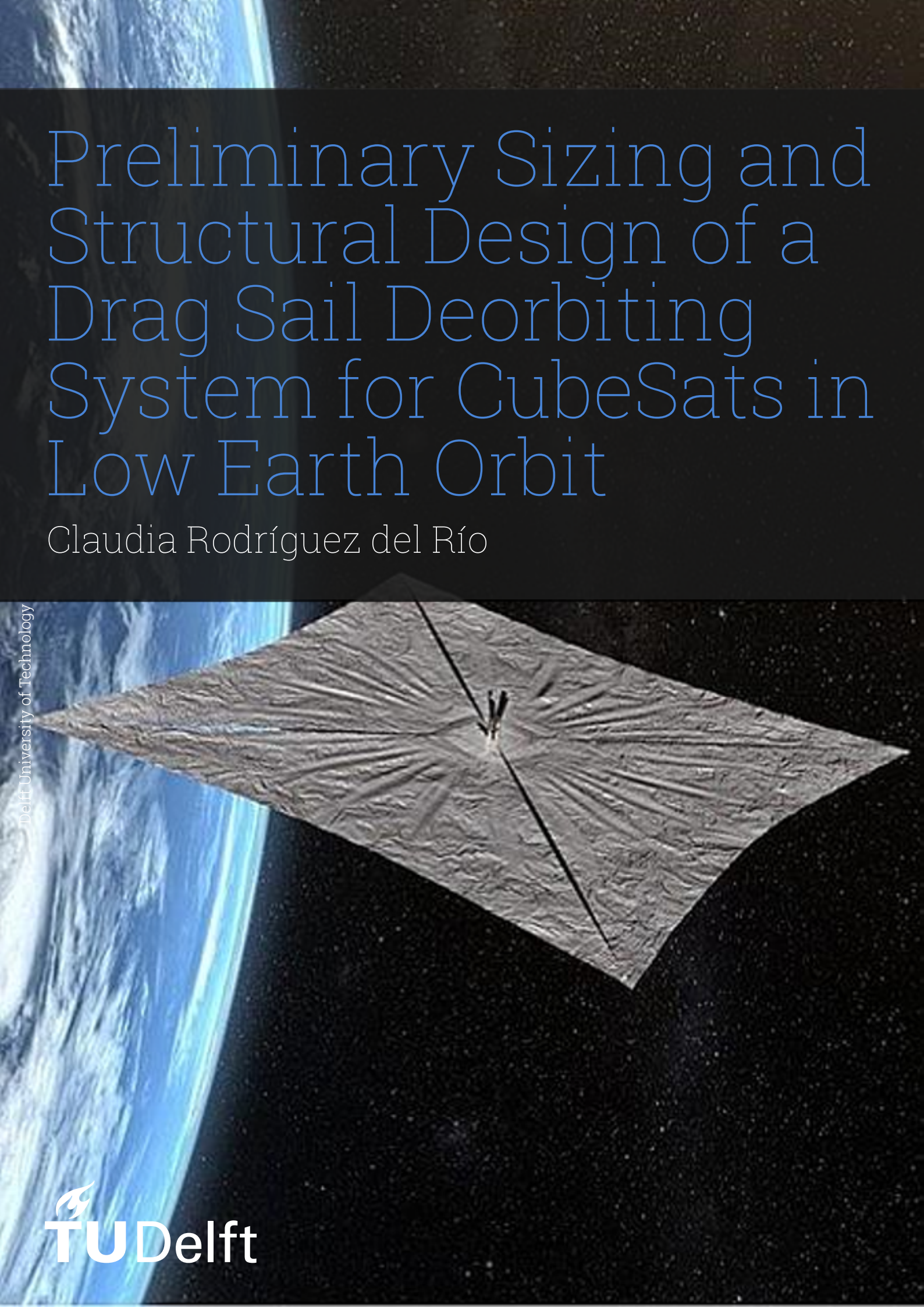

Delft University of Technology

TU Delft

Preliminary Sizing and Structural Design of a Drag Sail Deorbiting System for CubeSats in Low Earth Orbit

Master of Science Thesis

MSc. Aerospace Engineering
Delft University of Technology

by

Claudia Rodríguez del Río

TU Delft supervisor: Ines Uriol Balbin
Company supervisor: Bart van de Laar

November 2024

Cover: Overview and Key Technology of the Membrane Drag Sail for Low Earth Orbit Satellite Deorbit [76].

TU Delft

Preface

This MSc. thesis is the final product of my research on mitigating actions for space debris. The choice of this field of research is derived from a combination of factors. First and foremost, it reflects my dual interest in structural design and space systems. These interests motivated me to pursue a master's degree in Aerospace Structures & Materials, with a specialization in Structures for Space.

Another significant influence was the opportunity to build upon a topic I had previously explored during my internship. During my time at Demcon High-Tech Systems, I had the privilege of contributing to the development of their deorbiting system for CubeSats in Low Earth Orbit. The research aims to address the pressing issue of sustainability in the space environment, which is increasingly threatened by the high density of space debris in orbit. I hope this work supports the ongoing efforts to preserve space as a shared and accessible resource for future generations.

I want to express my gratitude to my academic supervisor Ines Uriol Balbin, for her guidance throughout this process. I greatly appreciated her approachability and the open communication we shared, which made it easy to discuss ideas and address challenges. I would also like to extend my gratitude to my company supervisor, Bart van de Laar, for his involvement in this project. His dedication and commitment were evident through our regular, and often more than weekly, meetings, during which his insights and feedback greatly enriched my work. I am especially grateful for both of my supervisor´s recognition of the quality of my research, which was deemed worthy of submission to international conferences. Together, we submitted an abstract that was not only accepted into one but two conferences: the 75th International Astronautical Congress (IAC) in Milan, where we presented our findings on orbital decay, and the European Conference on Spacecraft Structures, Materials, and Environmental Testing (ECSSMET) 2024, where we shared our work on the structural design of the system, both resulting in conference papers.

I also wish to thank my colleagues for their insightful feedback and discussions. And last but certainly not least, I am deeply grateful to my family for their support during this period. A special mention goes to my boyfriend Roberto, for his consistent encouragement and support. He was there to celebrate my successes and to provide reassurance during the more challenging moments.

Claudia Rodríguez del Río
Delft, November 2024

Abstract

The growing accumulation of space debris poses a significant threat to the long-term sustainability of space activities. A drag sail system presents a passive, post-mission disposal solution that utilizes the low atmospheric density in Low Earth Orbit to accelerate the re-entry and disintegration of satellites. This study focuses on the sizing and structural design of a drag sail system based on a preliminary design provided by Demcon High-tech Systems.

A numerical orbital decay model was developed in Python using Tudat libraries to determine the drag sail area that complies with the decay time requirement. The conservative perturbing forces, such as the Earth's gravitational field (including oblateness effects) and third-body gravitational influences, as well as non-conservative perturbing forces, such as atmospheric drag and solar radiation pressure, were included. The atmospheric density was estimated using the US76 neutral model and the NRLMSISE-00 dynamic model, with the latter yielding a more accurate result. Furthermore, two aerodynamic flow models: free molecular and continuum flow, were analyzed, showing a minor 4% difference in decay time. The results reveal that an accurate representation of atmospheric density is more critical than the drag coefficient due to the high variability in density predictions between models. Through validation of the model, it was found that using the average outer surface area of the CubeSat as the effective drag area offers a conservative yet reliable estimate for decay prediction.

The natural decay time of the host spacecraft was estimated at 31.4 years. The drag sail was designed to reduce this to 6.3 years, meeting the mission's fivefold reduction target. Analysis of the area-to-mass ratio indicated a ratio of 54 cm^2/kg, corresponding to a drag sail area of 0.2 m^2, will comply with the decay requirement time.

For the structural design of the booms, inflatable deployable structures were selected due to their compactness and long shelf-life, with strain rigidization as the post-deployment stiffening technique. Localized low rigidization near the boom end caps was observed. The sail configuration limited out-of-plane deflection to 2 mm, ensuring no effective drag area reduction or decay time increase. Stresses on the sail were well below failure thresholds, and its lowest natural frequency was 200 times greater than the highest frequency of the drag load, eliminating resonance risk.

Boom analysis revealed that bending is the primary failure mode. Lower inflation pressures enhanced bending performance, with the lowest pressure studied allowing the boom to withstand over five times the applied drag load before yielding. This significant safety margin accommodates potential imperfections, such as residual creases remaining after rigidization. Additionally, vibrational coupling between the sail and booms was avoided, thanks to a sufficient frequency separation of four times between the subsystems.

A final full system analysis indicated the deorbit system could survive the mechanical stresses induced by the drag load down to an altitude of 120 km. However, further investigation is needed to account for thermal loading at lower altitudes.

Contents

Nomenclature

Abbreviations

Abbreviation	Definition
ADAM	Able Deployable Articulated Mast
ADS-B	Automatic Dependent Surveillance-Broadcast
AGI	Analytical Graphics, Inc.
AU	Astronomical Unit
BC	Boundary Conditions
C	Compliant
CFRP	Carbon Fiber-Reinforced Plastic
CGG	Cold gas generator
DOM	De-Orbit Mechanism
EoL	End of Life
ESA	European Space Agency
FE	Finite Element
FEM	Finite Element Method
FFT	Fast Fourier Transform
GMAT	General Mission Analysis Tool
HPOP	Precision Orbit Propagator
HPS	High Performance Space
I	Imperfections
IAE	Inflatable Antenna Experiment
ISIS	Inflatable Sunshield in Space
KDF	Knockdown Factor
LEO	Low Earth Orbit
MLI	Multi-Layer Insulation
MoS	Margin of Safety
MPF	Mass Participation Factor
MS	Maximum Stress Failure Criteria
MSS	Maximum Strain Failure Criteria
NAIF	NASA's Navigation and Ancillary Information Facility
NASA	National Aeronautics and Space Administration
NC	Non-Compliant
NGST	Next Generation Space Telescope
NR	Non-Rigidized
NRLMSISE-00	Naval Research Laboratory Mass Spectrometer and Incoherent Scatter Radar Extended 2000
OBC	On Board Computer
PC	Partially Compliant
RC	Requirement Company
RK	Runge-Kutta
RS	Requirement Stakeholder
SF	Safety Factor
SFL	Space Flight Laboratory
SMM	Shape Memory Material
STK	Systems Tool Kit
TLE	Two-Line Element
TRAC	Triangular Rollable and Collapsible Booms

Abbreviation	Definition
Tudat	TU Delft Astrodynamics Toolbox
UHMWPE	Ultra-High-Molecular-Weight Polyethylene
US76	US Standard Atmosphere 1976
U	Displacement
UV	Ultraviolet

Symbols

Symbol	Definition	Unit
A	Cross-section area normal to the airflow	[m^2]
A_p	Geomagnetic index	[-]
A_{Sail}	Effective drag area of the drag sail	[m^2]
A_{Sat}	Effective drag area of the drag satellite	[m^2]
a	Length of the semi-major axis	[km]
a_d	Deceleration due to the drag force	[m/s^2]
a_p	Acceleration due to perturbing forces a	[m/s^2]
C_d	Drag coefficient	[-]
C_{dsail}	Sail drag coefficient	[-]
C_{dsat}	Satellite´s drag coefficient	[-]
C_P	Pressure coefficient normal to the surface	[-]
C_r	Radiation pressure coefficient	[-]
C_T	Shear pressure coefficient	[-]
D	Wall flexural stiffness per unit width	[N·m]
DT	Deorbit time	[years]
E	Young's modulus	[MPa]
e	Eccentricity	[-]
$F10.7$	Solar flux index	[W/m^2/Hz]
$F10.7_{ADJ}$	Adjusted solar flux index	[W/m^2/Hz]
$F10.7_{AVG}$	Average solar flux index	[W/m^2/Hz]
$F10.7_{OBS}$	Observed solar flux index	[W/m^2/Hz]
F_{boom}	Sail reaction force in the boom's local coordinate system	[N]
$F_{boom,a}$	Applied force on the boom in boom's local coordinate system	[N]
F_d	Drag force	[N]
F_{sail}	Sail reaction force in the sail's local coordinate system	[N]
G_{12}	Shear modulus	[MPa]
I	Second moment of inertia	[m^4]
i	Inclination	[$^\circ$]
Kn	Knudsen number	[-]
k	Constant dependent on boundary conditions for critical bending load	[-]
k_x	Buckling coefficient	[-]
L	Cylinder length	[m]
L_{ref}	Characteristic length of the entry object	[m]
LE	Logarithmic strain	[-]
LE_1	Hoop logarithmic strain	[-]
LE_2	Longitudinal logarithmic strain	[-]
M	Molar mass	[kg/mol]
M_{Boom}	Mass of the booms	[kg]
M_{Chasis}	Chassis mass	[kg]
M_{CGG}	Mass of the cold gas generator	[kg]

Symbol	Definition	Unit
$M_{DeployMech}$	Mass of the systems´s deploying mechanism	[kg]
M_{HostSC}	Mass of the host spacecraft	[kg]
$M_{Structural}$	Structural mass of the drag sail system	[kg]
M_{Sail}	Mass of the sail	[kg]
$M10.7$	Medium wavelength solar index	[W/m^2/Hz]
$M10.7_{AVG}$	Average medium wavelength solar index	[W/m^2/Hz]
m	Mass of the spacecraft	[kg]
m_p	Atmospheric particle mass	[kg]
N_A	Avogadro's number	[mol^{-1}]
N_x	Critical shell buckling line load	[N/m]
n_i	Number density	[m^{-3}]
P	Inflation pressure	[Pa]
P_B	Bending load that yields the material	[N]
P_{BH}	Bending load that fails the material after yielding	[N]
P_{CB}	Column buckling critical load	[N]
P_d	Drag pressure	[Pa]
P_{SB}	Critical shell buckling load	[N]
P_y	Inflation pressure that yields the material	[Pa]
R	Radius of the boom	[m]
R_e	Radius of the Earth	[m]
R_{gas}	Gas constant	[J/(kg·K)]
r	Vector from the Earth to the spacecraft	[km]
$\dot{r}$	Satellite's velocity relative to the center of the Earth	[km/s]
$\ddot{r}$	Satellite's acceleration relative to Earth´s the center of the	[km/s^2]
r_p	Perigee radius	[km]
r_a	Apogee radius	[km]
S	Stress	[Pa]
S_1	Hoop stress	[Pa]
S_2	Longitudinal stress	[Pa]
$S10.7$	Short-wavelength solar index	[W/m^2/Hz]
$S10.7_{AVG}$	Average short-wavelength solar index	[W/m^2/Hz]
s	freestream molecular speed	[-]
T	Orbital period	[s]
T_g	Glass transition temperature	[K]
T_w	Wall temperature	[K]
T_∞	freestream temperature	[K]
t	Thickness of the boom	[μm]
t_{Al}	Thickness of the aluminum	[μm]
t_{My}	Thickness of the Mylar	[μm]
UTS	Ultimate tensile strength	[GPa]
V_∞	freestream velocity	[m/s]
X	Maximum allowable stress in the X-direction	[Pa]
Y	Maximum allowable stress in the Y-direction	[Pa]
Z	Curvature parameter	[-]
α	Angle of the boom with the vertical	[$^\circ$]
Γ	KDF (Knockdown factor)	[-]
γ_{12}	Shear strain	[-]
δ	Angle applied force w.r.t. horizontal	[$^\circ$]
θ	Angle between the stream flow and the surface of the satellite	[$^\circ$]
ϵ	Relative error	[%]
ε	Strain	[-]
ε_1, ε_2, ε_3	Strain in the principal directions	[-]

Symbol	Definition	Unit
λ_{mol}	Mean free path length of air molecules	[m]
μ	Gravitational constant of Earth	[$m^3 s^{-2}$]
ν	True anomaly	[$^\circ$]
Ω	Right ascension of the ascending node	[$^\circ$]
ρ	Atmospheric density	[kg/m^3]
ρ_{Al}	Density of aluminum	[kg/m^3]
ρ_{My}	Density of Mylar	[kg/m^3]
σ	Particle collision diameter	[pm]
σ_1, σ_2, σ_3	Principal stresses	[Pa]
σ_c	Compressive strength	[Pa]
σ_h	Circumferential or hoop stress	[Pa]
σ_l	Longitudinal stress	[Pa]
σ_N	Normal momentum accommodation coefficient	[-]
σ_r	radial stress	[Pa]
σ_y	Yield strength of the material	[Pa]
ω	Argument of periapsis	[$^\circ$]

1

Introduction and Literature Review

This chapter provides the Introduction and Literature Review for this research. The Literature Review addresses the problem of space debris, covering its current state, mitigation strategies, and the fundamentals of orbital decay. It then focuses on drag sail systems, highlighting some state-of-the-art missions, and deployable structural designs, with emphasis on inflatable structures and post-deployment rigidization techniques.

1.1. Introduction

"Space debris can be defined as all man-made objects including fragments and elements thereof, in Earth orbit or re-entering the atmosphere, that are non-functional" [29]. The ongoing launch of satellites without active End of Life (EoL) removal measures contributes to an exponential increase in space debris. This issue is particularly concerning in Low Earth Orbit (LEO), where the high density of debris poses a significant risk of collisions with other debris or operational satellites. Such collisions could trigger a chain reaction, endangering the sustainability of the space environment and the safety of space missions [17].

This research project, in collaboration with the company Demcon High-tech Systems, aims to advance the understanding and application of drag sail systems as post-mission disposal systems for CubeSat in LEO. The project is based on the European Space Agency (ESA) tender 1-11988 [16]. The principal requirement is to reduce the natural decay time of a small satellite in LEO by a factor of 5, to a maximum of 10 years. A faster deorbiting rate reduces the probability of debris collisions and consequently the amount of debris generation.

Drag sails are post-mission disposal systems that increase the effective drag area of the host spacecraft, while marginally increasing its weight. These systems use the low atmospheric density in the upper atmosphere to increase the drag force in the opposite direction of the satellite's motion. This force decelerates the system, causing it to spiral toward Earth and disintegrate in the atmosphere due to the high thermal loads [73]. Drag sails have been successfully tested in space through demonstrator missions such as NanoSail-D2 [32] or CanX-7 [9].

The novelty of this research lies in the use of inflatable deployable structures to deploy and hold the drag sail in place during the deorbiting phase. Inflatable structures offer a low packaging ratio, low mass, and design versatility. However, due to their risk of gas leakage and sometimes complex deployment, it has not been a popular choice for space applications [31]. Over the years, numerous studies have been done on rigidization techniques to improve the mechanical properties and durability of inflatables in space [31]. One example of these rigidization techniques is mechanical rigidization by work hardening of the material. To rigidize the structure, the system is overpressurized, surpassing the yield stress of the metallic material, the plastically deformed metal maintains its shape and increased rigidity even after the inflating gas has leaked [31]. This rigidization technique was used in the spherical antenna ECHO 2 developed by the National Aeronautics and Space Administration (NASA) [14].

This report is organized as follows: Chapter 1 presents a literature review, addressing the issue of space debris, the fundamentals of orbital decay, the operating principles of drag sail systems, and the structural design options for deployment. Chapter 2 outlines the company's preliminary design and system requirements. Additionally, this chapter introduces the research objectives and questions derived from this preliminary design.

The two key aspects of the preliminary design that require further investigation are divided into Part I: *Orbital Decay* and Part II: *Structural Analysis*. Part I focuses on estimating the decay time and the drag sail surface area to comply with the tender´s decay time requirement. In this part, Chapter 3 presents a Python-based numerical model, developed using the TU Delft Astrodynamics Toolbox (Tudat) [11] and validated, to estimate the orbital decay time of a CubeSat in LEO. Next, Chapter 4 applies this decay model to size the drag sail, ensuring compliance with end-of-life disposal requirements. This process determines the drag load during the decay phase, which serves as input for subsequent structural analyses.

The focus of Part II is on ensuring the structure withstands the mechanical drag loads during decay. This analysis begins in Chapter 5, where the system's definition, including the chosen materials and rigidization technique. In Chapter 6 a static structural analysis is conducted to evaluate the system under the maximum drag load, with compression and bending identified as key failure modes. This analysis also examines the effectiveness of the selected rigidization technique. In Chapter 7, a modal analysis is performed to evaluate the system's dynamic response to aerodynamic forces. The final system design, incorporating insights from the design iterations, is detailed in Chapter 8. The report concludes with a summary of the findings and recommendations for future work in Chapter 9.

1.2. Literature Review

This section begins with an overview of the problem of space debris, including its current state and mitigation strategies aimed at reducing the high density of non-functional objects in orbit. Next, the fundamentals of orbital decay are presented, along with a discussion of existing software tools used to calculate the decay time and trajectories.

As the focus of this study is on drag sail systems, their definition and key state-of-the-art missions are explored. Since the structural design is a central theme of this report, various deployable structures are reviewed, with particular attention to inflatable designs and their rigidization techniques after deployment

1.2.1. Space Debris

"Space debris can be defined as all man-made objects including fragments and elements thereof, in Earth orbit or re-entering the atmosphere, that are non-functional" [29].

Since 2016, the European Space Agency (ESA) has released an Annual Space Environmental Report, to assess the evolution of the numerous non-functional objects orbiting the Earth and the effectiveness of the mitigating actions taken by the different organisms in the matter. Figure 1.1 was taken from 2023's Annual Space Environmental Report [17]. The image shows the space debris density for the different orbital ranges.

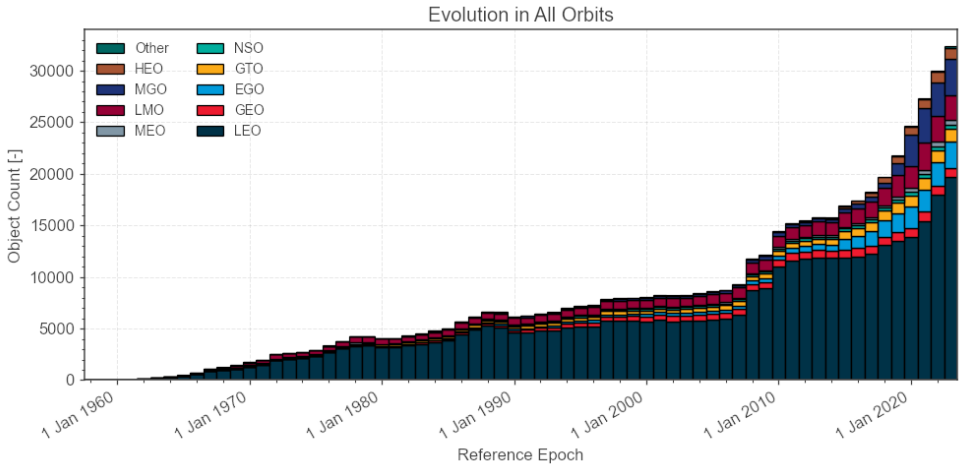

Figure 1.1: Evolution of the number of objects by orbit range [17].

LEO has always been a targeted orbit for satellite deployment, resulting in a significant accumulation of space debris. The combination of low altitude and short orbital periods make LEO suitable for high-resolution Earth imagery, remote sensing, and research, allowing fast data transmission and lowering the launch expenses [62].

The number of satellites launched last year was dominated by commercial satellite constellations in LEO [17]. A satellite constellation is a coordinated network of multiple satellites that operate together to achieve continuous coverage, solving the coverage limitations of individual satellites at low altitudes [62]. An example of this system arrangement is Starlink, a satellite constellation with more than five thousand interconnected satellites orbiting LEO, providing global Internet coverage [65].

The high density of non-functional systems or fragments of these systems raises the likelihood of collisions with operational satellites. Space debris is found in a broad range of masses, from fractions of milligrams to tons. Their effects on the impacting satellite can be classified into non-catastrophic and catastrophic. In non-catastrophic impacts, small debris causes local damage in the impacting satellite, although the satellite is still functioning, failure of components can shorten its lifespan. In catastrophic impacts, the high-impact energy due to the high mass of the debris results in the complete destruction of a satellite or major system [7].

The increasing amount of space debris not only threatens current spacecraft operations but also presents severe risks for future missions. Each collision generates additional debris fragments, thereby increasing the likelihood of further collisions. This chain reaction was studied by NASA's scientist Donald J. Kessler in 1978. Kessler proposed a theoretical scenario where the debris environment in LEO could reach a tipping point, leading to a self-sustaining cycle of collisions that would make certain orbital altitudes unusable [50].

Solutions to Space Debris

Different organizations have proposed diverse mitigation actions. The *2023's Annual Space Environmental Report* [17] divides these mitigation actions into four categories:

- **Limitation of space debris released during operation**. Avoid the release of space debris from launchers and payloads during their operational phase. An example of an action taken in this matter is the American company SpaceX, which is working towards full reusability of its rockets. As of today, their last launcher model, Falcon 9, recovers both stages, resulting in the recovery of nearly the total mass of the vehicle [6].
- **Minimization of the potential on-orbit break-ups**. Minimize breakups during operational phases, e.g. increase the system's reliability. Minimize EoL break-ups due to stored energy, e.g. actions to safely dispose of residual propellant, and avoidance of missions with the intentional goal of other systems destruction.
- **Post mission disposal**. Decrease the natural deorbit time of non-functional payloads or rocket fragments or relocate them to a "graveyard" or disposal orbit. An example of a sub-system used to accelerate the natural deorbit time is a drag-sail, This drag augmentation system is a good solution for small satellites at LEO, due to the simplicity of the mechanism, high package ratio, and low cost.
- **Prevention of in-orbit collisions**. Mission design accounting for probable collisions with known in-orbit objects. In the case there is collision risk, use avoidance maneuvers in the form of ignition of boosters or passive mechanisms.

Due to the already high number of space debris present in orbit, even if all future missions will fully comply with the mitigating actions listed above, persistent growth of space debris is still expected. This means that the number of space debris has reached a critical stage, and active debris removal technologies are also necessary [29].

The European Space Agency has officially authorized the world's first space debris removal project called ClearSpace-1 [18]. This mission will capture, using a robotic arm, the 100 kg Vega secondary payload adapter, currently orbiting at around 800 km altitude. When the debris is secured, both systems, the adapter and the ClearSpace-1, will start the deorbiting phase where they will disintegrate in the atmosphere.

1.2.2. Fundamentals of Orbital Decay

The two-body equation of motion, as given in Equation 1.1, describes the motion of two interacting bodies under their mutual gravitational fields. This model assumes that the only forces acting on the system are those due to the gravitational attraction between their masses. It also assumes that the spacecraft's mass is negligible compared to the attracting body and that both bodies are spherical, symmetrical, and with uniform densities. For simplicity in vector differentiation, an inertial coordinate system is used in this analysis [69].

$$\ddot{\vec{r}} = -\frac{\mu}{r^2}\frac{\vec{r}}{|\vec{r}|} \tag{1.1}$$

where $\ddot{\vec{r}}$ is the satellite's acceleration relative to the center of the Earth, μ is the gravitational constant of Earth, and $\vec{r}$ is the vector from the Earth to the spacecraft.

Orbital perturbations can significantly deviate the motion of the satellite from its idealized path. These perturbations are categorized into conservative and non-conservative types. Conservative perturbations include the main body gravitational field, the third body gravitational fields, and the Earth's oblateness. Non-conservative perturbations involve atmospheric drag, solar radiation pressure, and magnetic

forces [69]. LEO satellites have natural decay times predominantly determined by atmospheric drag [73].

A common way of accounting for these perturbations in astrodynamics is using Cowell's formulation, by adding the perturbing accelerations to the two-body problem equation as described in Equation 1.2 [69].

$$\ddot{\vec{r}} = -\frac{\mu}{r^3}\vec{r} + \vec{a}_p \tag{1.2}$$

where $\vec{a}_p$ is the total acceleration due to all perturbing forces acting on the spacecraft.

To solve for Equation 1.2, Cowell's Method re-forms the three second-order differential equations of motion into six first-order differential equations as described in Equation 1.3 [69].

$$\vec{X} = \begin{bmatrix} \vec{r} \\ \dot{\vec{r}} \end{bmatrix} \qquad \dot{\vec{X}} = \begin{bmatrix} \dot{\vec{r}} \\ \frac{\mu\vec{r}}{r^3} + \vec{a}_p \end{bmatrix} \tag{1.3}$$

Different numerical methods can be used to solve this system of first-order differential equations, but the Runge-Kutta family of integrators is a popular choice [69].

The following sources of orbital perturbation are dominant at low altitudes: gravity field of the central body, atmospheric drag, solar pressure, and third-body perturbations [69].

Gravity Field of the Central Body. The Earth is not a perfect sphere. It can be approximated as an ellipsoid, flattened at the poles and bulging at the equator, an oblate spheroid. Due to this irregular distribution of the Earth's mass, the gravity field around the Earth is not uniform. The aspherical-potential function is a mathematical model used to describe the gravitational field due to the irregular geometry of the Earth. Each coefficient from the function defines a specific aspect of the non-uniformity of the Earth´s mass. The J2 coefficient accounts for most of the Earth's deviation from a sphere [69].

Atmospheric Drag. Drag is a non-conservative perturbation, where the spacecraft loses energy due to friction. Atmospheric drag acts opposite to the motion of the spacecraft, decreasing its velocity. Equation 1.4 is used to determine the deceleration of a spacecraft due to atmospheric drag [69].

$$\vec{a}_d = \frac{1}{2}\rho v_{rel}^2 \frac{C_d A}{m} \frac{\vec{v}_{rel}}{|\vec{v}_{rel}|} \tag{1.4}$$

where $\vec{a}_d$ is the deceleration due to the drag force, ρ is the atmospheric density, $\vec{v}_{rel}$ is the velocity of the spacecraft relative to the moving atmosphere, A is the cross-section area normal to the airflow, m is the mass of the spacecraft and C_d is the drag coefficient.

Atmospheric density and drag coefficient are influenced by environmental conditions, making them difficult to accurately estimate. Additionally, if the satellite lacks an attitude control system, determining the effective drag area can be challenging, as the satellite may be tumbling during its descent [69].

Third Bodies. The effect of the Sun and Moon's gravity as a conservative perturbation force on the spacecraft becomes more noticeable when the effect of the drag force diminishes. The closest the spacecraft is to the third body, the highest will be the perturbation force due to its gravity [69].

Solar Pressure. Solar pressure is a non-conservative force, acting on the satellite by transmitting the momentum carried by the photons. The reflectivity of the spacecraft describes how the incoming radiation from the Sun is reflected on the satellite´s surface. This characteristic is defined by the emissivity coefficient, whose value ranges from 0 to 2. An emissivity of 0 indicates the object is translucent, thus no momentum is transmitted. An emissivity of 1 means the radiation is fully absorbed and all the momentum is transmitted. An emissivity of 2 implies that all the radiation is reflected, thus the resulting force is twice the absorbed by the spacecraft. Solar pressure can be hard to predict due to the variability of solar activity and the change in the emissivity of the material with time due to degradation [69].

Orbital Decay Calculation Software and Libraries

This section presents three software options to estimate the orbital decay time of a satellite.

Systems Tool Kit (STK) SatPro by Analytical Graphics, Inc. (AGI). The STK SatPro module provides tools for the design and operation of satellite systems. The satellite's decay time can be estimated using the Lifetime tool. This function estimates the time the satellite remains in orbit before drag and other orbital perturbations cause it to decay. The Lifetime tool has the option to include the drag perturbation, by introducing the drag coefficient, drag area, and atmospheric density; and the solar radiation perturbation, by including the area exposed to the sun and the solar radiation pressure coefficient. A better estimation of these two perturbations will be made if the solar flux file is also included as input [4].

If the state vector is a desired output, the High Precision Orbit Propagator (HPOP) can be used. HPOP is computationally more expensive as it estimates the position and velocity of the satellite along the decay trajectory. This propagator includes the effects of central body gravity and third body gravity in the calculations [4].

General Mission Analysis Tool (GMAT) by NASA. In GMAT the decay time and state vector can be estimated by including a force model appropriate to the flight regime. The Force Model Group includes point mass and non-spherical perturbations, atmospheric drag perturbation, and solar pressure perturbation. The solar activity and magnetic index can be included for a better estimation of the density, and therefore drag acceleration [46].

TU Delft Astrodynamics Toolbox (Tudat). Tudat is a set of Anaconda libraries that support astrodynamics and space research. It enables the calculation of satellite decay profiles by incorporating various factors such as atmospheric drag, point mass and non-spherical accelerations, and solar pressure effects. The use of these libraries allows the user more flexibility in the mission design, as the code can be manipulated [11].

1.2.3. Drag Sail Systems

Drag sails are post-mission disposal systems designed to increase the drag area of a spacecraft while only slightly adding to its mass. By deploying a large sail, these systems use the low atmospheric density present at high altitudes to increase the drag force in the opposite direction of the satellite's motion. This drag force gradually decelerates the spacecraft, leading it to spiral downward and eventually burn up in Earth's atmosphere due to high thermal loads [73]. Figure 1.2 illustrates a schematic representation of this decay process, where v is the velocity vector and F_d is the drag force vector.

Figure 1.2: Drag sail working principle.

State-of-the-Art Systems

Drag sails have been studied as a post-mission disposal solution for LEO since the early 2000s. This section presents a compilation of various state-of-the-art drag sail systems.

InflateSail. InflateSail was developed by the Surrey Space Center to demonstrate the efficiency of drag sail systems as EoL disposal mechanisms and verify the functionality of the deployable systems on board. The deorbiting device consisted of a 3U CubeSat where 1U was reserved for the spacecraft's core avionics and the remaining 2U stored the 1 m inflatable-rigidizable mast and 10 m^2 drag sail [68].

InflateSail was launched to a 505 km orbit on June 23rd, 2017, and disintegrated 72 days later on September 3rd, 2017. The system's deployment started with the inflation and rigidization of a 1 m cylindrical aluminum boom, from which the drag sail deployed thanks to the uncoiling of four bistable CFRP (Carbon Fiber-Reinforced Plastic) booms. The purpose of the inflatable boom was to offset the sail's center of pressure from the system's center of mass, which results in an aerodynamic stable system [68]. Figure 1.3 shows the fully deployed configuration of the drag sail in orbit.

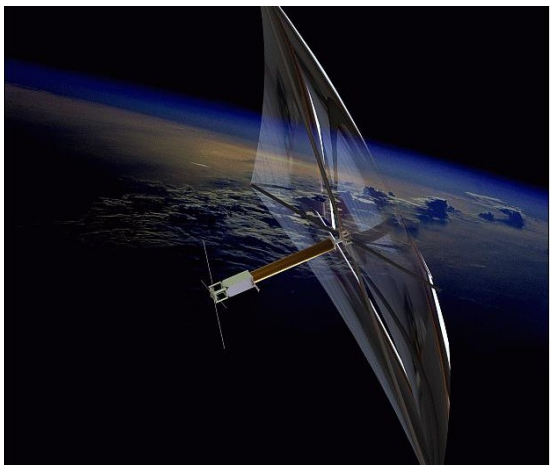

Figure 1.3: InflateSail in-orbit boom deployed configuration [68].

Icarus and DOM. Icarus and De-Orbit Mechanism (DOM) are post-mission disposal systems developed by Cranfield Aerospace Solutions to mitigate the debris generation at LEO. Icarus-1, equipped with a 6.7 m^2 sail, was launched in 2014 to an altitude of 635 km, as part of the TechDemoSat-1 mission and remains in orbit. Icarus-3, with a 2 m^2 sail, was launched in 2015 aboard the Carbonite-1 spacecraft, also still in orbit. Both Icarus modules share a similar structural design, consisting of a lightweight drag sail deployed using rigid struts connected by tape hinges [63].

Contrary to the Icarus series, the DOM module, equipped with a 0.5 m^2 sail, is not constrained by the host satellite's dimensions. DOM is an attachable module that can be mounted on any side of the host spacecraft. The boom deployment was also switched to a strain energy release mechanism, where the booms work as tape springs themselves. The DOM module was launched aboard the European Student Earth Orbiter to an initial altitude of 572 km and will be activated at the EoL of the host system [63]. Figure 1.4 shows the deployed configuration of DOM.

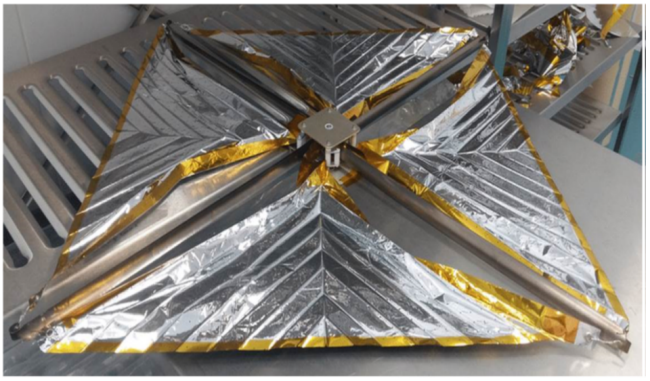

Figure 1.4: DOM deployed configuration [63].

CanX-7. CanX-7 was a demonstrator mission for two different payloads, a drag sail system as the primary payload and an Automatic Dependent Surveillance-Broadcast (ADS-B) receiver for tracking aircraft as a secondary payload. The Space Flight Laboratory (University of Toronto) developed the CubeSat and launched it into a 680 km altitude orbit on September 26th, 2016 [9].

The drag sail payload consisted of four modular independent systems, each one releasing a 1 m^2 drag sail. The total volume of the four modules occupied less than 25% of the whole 3U CubeSat. Each module consisted of two tape spring booms, which deployed a triangular section drag sail. The advantages of this modular design are the scalability of the system, being able to use a different number of modules based on the size, mass, and altitude of the host spacecraft, as shown in Figure 1.5, and its high reliability, as independent modules mitigate the risk of single-point failures [9].

CanX-7 used the same approach as InflatableSail to achieve passive aerostability. By offsetting the plane of the drag sail (center of pressure) from the spacecraft's center of mass, the system reached a favorable aero-stable attitude, increasing the effective surface area and thus the drag force [9].

After launch, the system orbited the Earth for seven months, to demonstrate the functionality of the ADS-B payload, before deploying the sail on May 5th, 2017. From the official SFL website [64], it is known that CanX-7 disintegrated in the atmosphere, but no exact date is provided.

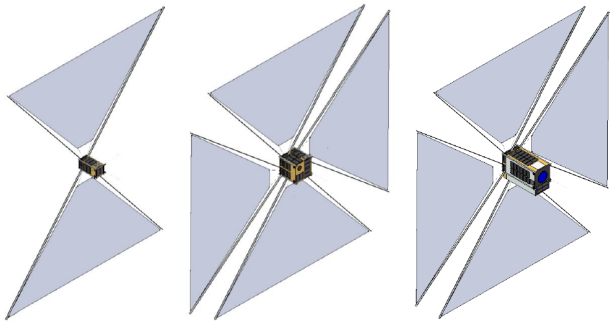

Figure 1.5: CanX-7 sail concepts for different host satellites [9].

ADEO – Deployable Deorbit Sails. ADEO is a commercial deorbiting system developed by the company High Performance Space (HPS). According to their website [28], ADEO is a scalable subsystem able to deorbit satellites of masses between 1 to 2000 kg from LEO within 5 years, to comply with the new deorbit regulations. ADEO has divided its product into five different categories which increase in drag surface area with the weight of the host spacecraft.

- ADEO-P(ico), for host spacecraft between 1 and 20 kg. Deploys a 1.4 m^2 drag sail.
- ADEO-C(ube), for host spacecraft between 5 and 50 kg. Deploys a 3.4 m^2 drag sail.
- ADEO-N(ano), for host spacecraft between 20 and 250 kg. Deploys a 5 m^2 drag sail.
- ADEO-M(edium), for host spacecraft between 100 and 700 kg. Deploys a 15 m^2 drag sail.
- ADEO-L(arge), for host spacecraft between 500 and 1500 kg. Deploys a 25 m^2 drag sail.

The structural design of the first five configurations is similar. The drag sail is deployed by tape spring deployable booms, which use the stored strain energy due to their elastic deformation in the stowed configuration. ADEO-L, shown in Figure 1.6, due to the big surface area of the sail, needs deployment control electronics to eject the passive deorbiting system [28].

ADEO-N2 was launched in 2021 on board D-Orbit's ION Satellite Carrier. The deorbiting system was successfully deployed in December 2022 after a 16-month mission. ADEO-L2 will be launched in 2025 on board an ESA In-Orbit Verification spacecraft, built by Redwire Space [28].

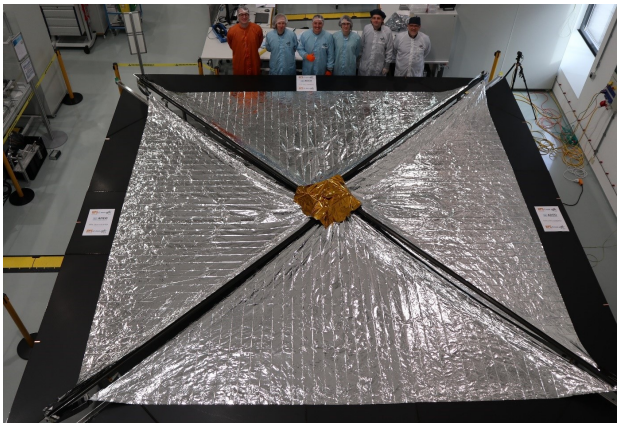

Figure 1.6: ADEO-L deployed configuration [28].

NanoSail-D2. NanoSail-D2 was a technology demonstrator mission developed by NASA in 2010 [32]. The mission's main objective was to test the deployment of a compact solar sail boom under space conditions. NanoSail-D2 succeeded NanoSail-D, which was lost in the 2008 explosion of the Falcon 1 rocket.

The demonstrator was launched into LEO (640 km altitude), even though the purpose of the solar sail is not deorbiting, the increase in surface area augmented the drag force making the system decelerate and re-enter the atmosphere. The demonstrator successfully deployed the booms and orbited the Earth for 240 days before disintegrating into Earth's atmosphere on September 17th, 2011. NanoSail-D2 performed better than expected, with a lower decay time than initially estimated [32].

The system consisted of a 3U CubeSat, where 1/3 of its volume housed the spacecraft bus, and the remaining 2/3 accommodated the 10 m^2 solar sail and Triangular Rollable And Collapsible (TRAC) booms which deployed and held the drag sail in place. The device had passive altitude stabilization magnets, to detumble and orient the system perpendicular to the incoming airflow before deploying the solar sail. The system later relied on atmospheric drag to stabilize the sail and obtain a maximum decay rate [32]. Figure 1.7 shows the deployed configuration of the drag sail.

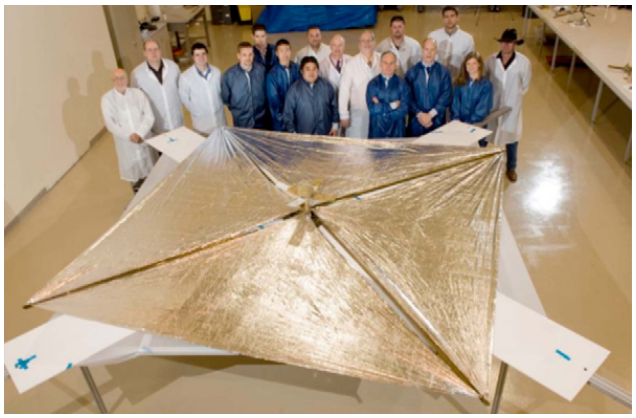

Figure 1.7: NanoSail ground deployment test [32].

Summary Table 1.1 summarizes the main characteristics of the above-discussed passive drag augmentation systems. The core information of the table was obtained from NASA's report on State-of-the-Art of Small Spacecraft Technology [72], and was extended with the previously presented information. (The system's mass was not found for every case, indicated with - in the table).

Table 1.1: State-of-the-Art drag sail systems, summary table.

System	Developer	Host	System mass [kg]	Drag area [m^2]	Orbit altitude [km]
InflateSail	Surrey Space Center	InflateSail (3.2 kg)	-	10	505
CanX-7	UTIAS-SFL	CanX-7 (3.6 kg)	-	4	688
Icarus-1	Cranfield Aerospace Solutions	TechDemoSat-1 (157 kg)	3.5	6.7	635
Icarus-3	Cranfield Aerospace Solutions	Carbonite-1 (80 kg)	2.3	2	650
DOM	Cranfield Aerospace Solutions	ESEO (45 kg)	0.5	0.5	572
ADEO-P	HPS	1-20 kg	0.45	1.4	LEO
ADEO-C	HPS	5-50 kg	0.8	3.4	LEO
ADEO-N	HPS	20-250 kg	0.8	5.0	LEO
ADEO-M	HPS	100-700 kg	4.5	15	LEO
ADEO-L	HPS	500-1500 kg	9.5	25	LEO
NanoSail-D2	NASA	FASTSAT(4.2 kg)	-	10	640

1.2.4. Deployable Structures

Volume is a key design requirement for spacecraft structures and a common constraint in spacecraft subsystem design. The effective utilization of the enclosed volume increases the payload capacity and allows for the integration of additional subsystems within the satellite [70].

Deployable structures unfold from an initial folded stage to a desired post-deployment configuration. These structures are characterized by their superior packaging efficiency, making them a suitable option for space applications. They can be categorized into three groups: pantographic structures, elastically deformed deployable structures, and inflatable deployable structures [70].

Pantographic structures

Pantographic structures consist of rigid elements like bars or rods interconnected by pivot joints such as hinges. The deployment is driven by additional mechanical movement units, which by rotation and translation of the components, unfold the rigid elements until the structure reaches its fully deployed state. These structures have good controllability during the folding and unfolding phases, high structural rigidity, and are versatile and reliable. They have a complex design and high weight due to the motor

system [70]. Figure 1.8 shows an Able Deployable Articulated Mast (ADAM), a pantographic mast developed by AEC-Able Engineering, Inc. used in the Shuttle Radar Topography Mission to extend the outboard antenna [22].

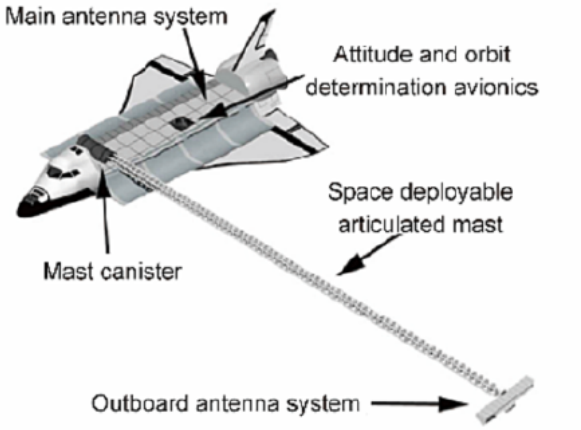

Figure 1.8: ADAM application in the SRTM mission [70].

Elastically deformed deployable structures

Elastically deformed deployable structures consist of elastic components with two main functions, structural elements and deployment-driving mechanisms. The elastic members are folded within their elastic range in the stowed configuration. When the constraining ceases, the stored strain energy drives the deployment process. This configuration is simpler and less heavy than the pantographic mechanisms. The deployment is highly dynamic and hard to control. An external device is needed for the restraint of the folded configuration. In the cases of long-term packaging, the elastic members can undergo fatigue and inelastic deformation [70]. Figure 1.9 shows the TRAC booms, elastically deformed deployable booms used for the sail deployment of the NanoSail-D drag sail [32].

Figure 1.9: Coiled TRAC boom [32].

Inflatable deployable structures

Inflatable deployable structures have a very simple design, consisting of a gas pump or inflatable device and a thin layer envelope. Its deployment is driven by the injection of pressurized gas into the thin envelope. The inside pressure given by the gas provides stiffness to the system. This system has a very high package ratio and simple design. Inflatable structures have a low deployment precision and air tightness is practically unachievable, therefore a stiffening technique post-deployment is needed to ensure long-term stiffness during the mission [70]. An example of a space inflatable structure is the antenna Spartan 207/IAE. The antenna was deployed on May 20, 1996, and recovered on May 21, 1996. The goal of the project was to demonstrate the mechanical performance of the structure in the space environment. The structure was deployed successfully but uncontrolled. Nonetheless, the mission was considered a success, as the low cost, high packing ratio, and mechanical properties demonstrated the potential of inflatable structures for space applications [23]. Figure 1.10 shows a Space Shuttle view of the L'Garde's Inflatable Antenna Experiment.

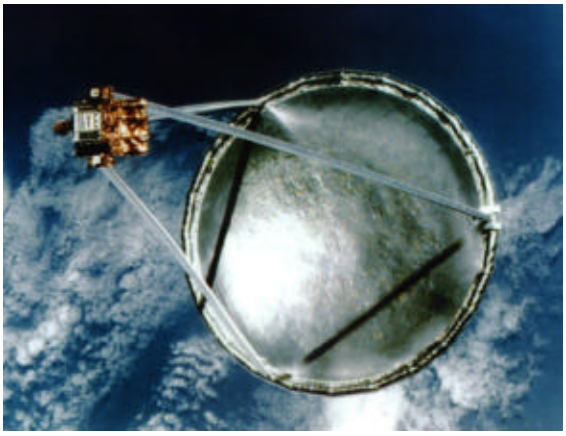

Figure 1.10: Space Shuttle view of the L'Garde's Inflatable Antenna Experiment (IAE) [5].

1.2.5. Inflatable Deployable Structures

Inflatable structures are thin-walled flexible structures that use pressurized gas for their deployment. The tender on which this design is based aims to promote the development of inflatable structures for space applications, due to their high packaging efficiency, low mass, and large deployed size [52].

Inflatable structures can be categorized according to their intended structural function as follows [52]:

- Light loaded: structures designed for the orbital environment, sized to support an internal tension of $\sim$0.1 kN/m. They can be further divided into support structures, with low accuracy of the final shape, and precision structures, where their shape has a direct impact on the operation.
- Heavy loaded: structures designed to carry loads, usually pneumatic. They are sized to have a large inner volume, moderated mass and sustain human presence. They can support $\sim$100 kN/m. A common example is inflatable habitats.
- High-temperature resistant: structures designed to support high thermal loads, mainly used for re-entry purposes.

Rigidization techniques

Achieving full airtightness of inflatable structures is nearly impossible, due to accidental piercing of the thin layer during the manufacturing process or micrometeorite impacts during the in-orbit phase. Therefore pressure control and gas supply devices are needed to restore the initial pressure over time. This solution might be feasible for short-period missions, but normally, space missions last for years or even decades, thus a permanent rigidization technique is key for their efficient use in space [52].

The rigidization techniques presented below are used for light and heavy-loaded inflatable structures, and might not be useful for high-temperature resistant structures. These techniques are categorized into mechanical, physical, or chemical rigidization [52].

Mechanical Rigidization. Aluminum work hardening by mechanically straining the material is the only technique in the category.

Aluminum Work Hardening. The structure consists of a polymeric bladder, commonly made out of Mylar or Kapton, used as a pressure barrier, and a thin aluminum outer layer. To rigidize the structure, the system is overpressurized, surpassing the yield stress of the metallic material, elevating its mechanical properties, and removing the creases from the folded configuration. Once the gas escapes the structure, the plastically deformed metal maintains its shape and increased rigidity [31]. This rigidization technique is simple, predictable and ensures fast rigidization. It does not require additional systems or power, is durable in space conditions, and is compatible with long storage. However, it needs an accurate control of the gas injection [31].

ECHO 2 by NASA is an example of this rigidization technique. The spherical antenna was manufactured from an 1100-0 aluminum foil layer and polyester film. The rigidization was a success, as the

system orbited the Earth for several years. Figure 1.11 shows the inflatable antenna in its deployed configuration.

Figure 1.11: NASA's Project ECHO II [48].

Physical Rigidization. The physically induced rigidization can be based on the phase transition of a material, shape-memory materials, or solvent evaporation.

Cold rigidization. By employing a cold rigidization process, the initially inflated polymer structure is cooled to a temperature below its glass transition temperature (Tg), the rigidization takes place by freezing the material. Sub-Tg conditions can be achieved for a wide range of missions, ranging from LEO orbits to interplanetary missions [31]. However, due to the reliance on extremely low temperatures for rigidization, a rigorous study of the thermal environment is crucial [35].

This rigidization technique was tested to be used in the Deployable Solar Sail developed by L'Garde, Jet Propulsion Laboratories, and Langley Research Center, under the direction of the NASA In-Space Propulsion office. Figure 1.12 shows the test set-up, where the boom is inside the cold box.

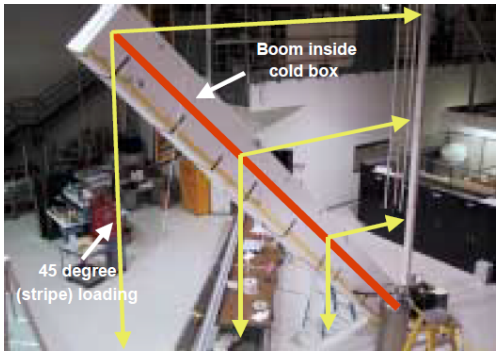

Figure 1.12: Sub-Tg solar sail boom test [35].

Shape Memory Materials. Shape memory composites can naturally recover their set geometry if they are heated above their transition temperature. To give the structure its final shape, the system is consolidated on-ground, normally at a very high temperature. To store the structure in its launch enclosure, the system is heated below its transition temperature, to be able to fold and store it. Before deployment in space, the system needs to be heated again, below its transition temperature to inflate it. Once deployed the system will reach its transition temperature, either by the high thermal loads in the space environment or heaters, and stick to its design shape [52]. The fiber-reinforced shape memory materials have high stiffness and strength and have a long storage life. However, rigidization is a very complex process, which needs uniform heating and high energy, to reach the glass-transition temperature [52].

ILC Dover fabricated and tested a composite antenna truss structure. The shape memory trusses were 45.7 mm in diameter and 1.5 m in length. The booms had one layer of IM7 carbon fiber and another layer of a shape memory polymer. Once folded, heaters were used in the test setup to unfold the booms [37]. Figure 1.13 shows the folded and unfolded state of the truss structure.

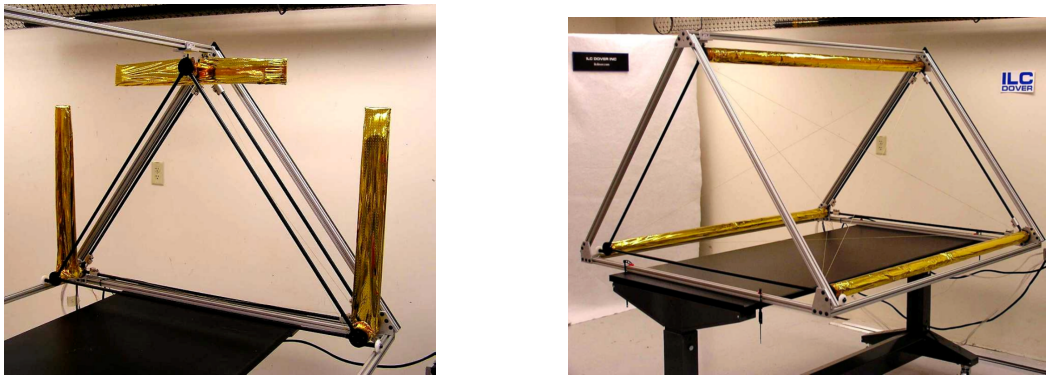

(a) Folded configuration. **(b)** Deployed configuration.

Figure 1.13: SMP Composite Truss [37].

Evaporation of a solvent or a plasticizer. Rigidization arises due to the evaporation of a solvent or a plasticizer in the matrix of a composite material. The polymeric matrix is softened by introducing a volatile component. The volatile component evaporates when exposed to the space environment [31].

An advantage of the polymer-solvent mixture is its high resistance to cosmic radiation. However, this rigidization technique is complex and requires large volumes of solvent. When the solvent evaporates, the polymer has a high mass loss and is prone to shrink, causing internal stresses and changes in the fiber reinforcement orientation [31].

This rigidization mechanism was applied by y L'Garde to develop an inflatable truss for space applications. Figure 1.14 shows the truss assembly. Each truss was made out of woven graphite fabric impregnated with a water-soluble resin. Evaporation of the water after inflation rigidizes the structure [31].

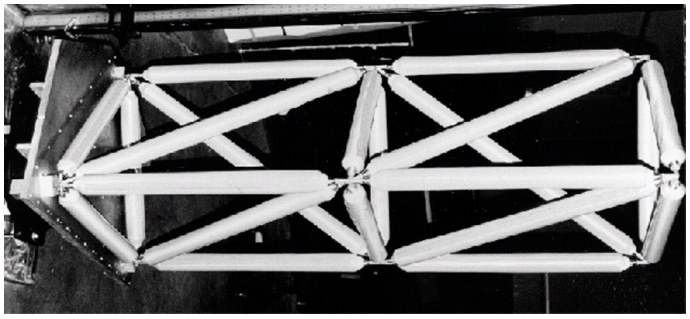

Figure 1.14: L'Garde hydro-gel truss assembly [31].

Chemical Rigidization. The chemical-based rigidization can be achieved by either thermally or ultraviolet (UV) polymerization. These techniques can always be accelerated by a catalyzer mixed in the inflation gas [31].

Thermal curing of thermoset composites. The thermal curing of thermoset composites has been used in the aeronautical sector for decades now. These composite materials consist of a fiber reinforcement within a thermoset polymer matrix. The initially elastic material undergoes a thermal-curing process in which the matrix hardens, rigidizing the composite. Even though they have been widely utilized in aircraft design, the limited shelf-life of the polymer and the need for high thermal energy for the curing process made them unsuitable for space applications [31].

Composites are low-weight, strong materials that can be tailored to optimize the performance of the structure by changing their fiber density and direction. High-performance thermosets have good resistance to space conditions and low thermal expansion. However, even after recent advances, their low-shelf life and the outgassing of the uncured state is a problem. On top of that, the thermal energy needed for the curing process is still high. When using the energy from the environment, not homogenous curing is prone to happen. Using heaters a controlled curing will be possible, but the system increases its complexity and weight [52].

This rigidization technique was in the Inflatable Sunshield in Space (ISIS). ISIS is a demonstrator mission to prove the feasibility of using inflatable systems to passively cool the aperture mirror and optical detectors for the Next Generation Space Telescope (NGST) missions. This sun shield is one-third smaller than the intended design for the NGST, and its design and manufacture is a partnership between NASA and ILC Dover. The shield contains four inflatable thermoset booms which will be deployed by inflation and rigidized using heaters to cure the composite material at 120°C for 45 minutes [36]. Figure 1.15 shows the deployed configuration of the ISIS. This demonstrator mission was unfortunately canceled [53], but ground testing proved the successful curing of the composite booms, and gave essential information for future development of such technique [36].

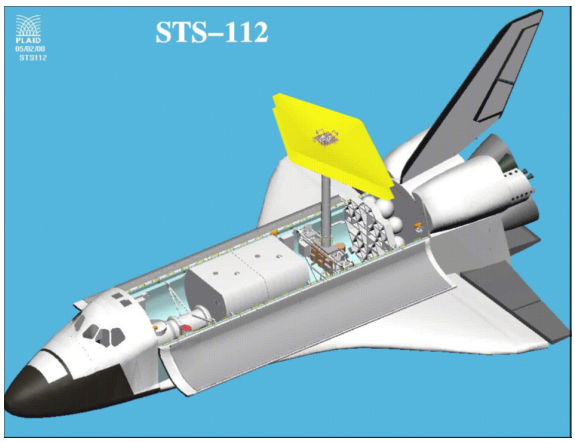

Figure 1.15: Inflatable Sunshield in Space (ISIS), deployed configuration [53].

UV curing of thermoset composites. The ultraviolet (UV) curing of thermoset composites follows a similar approach to the thermal curing explained above. In this case, the rigidization is triggered by the exposure of the composite to a range of wavelengths in the UV spectrum (between 250 nm and 380 nm). The strength of UV-cured composites is lower than the thermally cured ones. This is due to the limited selection of fiber reinforcements that can be used, as they need to be transparent to UV energy. Typical fibers used in this case are glass fibers or quartz fibers [31].

As in the case of thermally cured composites, the UV source can be either in the space environment, simplifying the design of the system, or by UV lamps installed in the spacecraft. Again, due to eclipse phases, the curing can be unequal along the structure. The use of UV sources also adds weight and complexity to the design. Tailoring and relatively high stiffness are obtained with this rigidization technique [31].

An example of a UV-rigidizable resin is the Rigidization-on-Command™ (ROC) Resin. The objective of this program was to create a family of space-qualified radiation-curing resins used for the rigidization of inflatable space structures. Testing showed the successful rigidization of the resin, with lower power requirement than the thermally cured composites. On top of that, the thermoset showed low outgassing, chemical stability for long periods, and good mechanical properties. The ROC resins have been tested with both UV sources, UV lamps, and environmental UV (process shown in Figure 1.16) [27].

Figure 1.16: ROC boom environmental curing [3].

Gaseous Catalyst. A gaseous catalyst, which can be mixed with the inflation gas or have its own pumping system, activates and sustains the curing process of the composite material. The composite is made out of fiber reinforcement impregnated with the reacting matrix. The inner ply of the structure must be impermeable to the catalyst and the thickness of the composite limited, to ensure the penetration of the acting agent [31].

No external power is needed for this rigidization technique. These materials are highly chemically stable before deployment, as the active agent and the elastic composite are separated during storage. The strength and tailoring capabilities of the material are strong advantages. However, the restrained thickness needed for efficient penetration of the catalyst can decrease its mechanical properties [31].

Some examples of this kind of polymerization are water vapor-cured polyurethanes, polyesters, and epoxies cured by different amines [31].

Foam. Foam serves not only as a method for rigidization but also as an inflating agent. There are two primary approaches for incorporating foam into the structure. The first method involves directly introducing the foam using a pump, similar to how inflation gas is applied. Alternatively, the internal walls of the structure can be coated with a material that reacts to a catalyst or specific environmental conditions to generate foam [31].

The mechanical properties of a foam rigidized structure are low in comparison with the composite options discussed above. But it still gives sufficient rigidity to the structure to be used as a low-load-bearing member. Outgassing, low storage life, and uniformity of the foam within the structure are disadvantages of this technique [31].

Rigidization technique trade-off

As seen from the previous examples, all the above-discussed rigidization techniques have been studied or even proven for space applications. A critical characteristic to take into account when selecting the rigidization method for the drag sail system is it requires a long shelf-life. The system will remain stowed until the spacecraft reaches its EoL, when the sail deploys to accelerate its re-entry and disintegration.

Rigidization of polymers via UV or thermal curing provides the highest structural strength but has a limited shelf-life, it also requires UV lamps or heaters to achieve a homogeneous rigidization, increasing the weight of the system. Similarly, rigidization by foam expansion suffers from low shelf-life and inhomogeneous rigidization and, therefore excluding them from consideration.

Cold rigidization and shape memory materials are not viable options for this design. These techniques require precise knowledge of the mission's thermal conditions to ensure the material reaches its glass transition temperature. Given the lack of a fixed mission profile or specific customer requirements for this system, these methods have been discarded.

Rigidization via solvent evaporation requires significant initial mass and volume due to the large quantities of solvent required. These factors make this approach impractical for a lightweight and compact drag sail design.

Rigidization by a gaseous catalyst requires an extremely thin envelope to allow the catalyst to penetrate effectively. Such a thin configuration might fail to withstand the stresses caused by decay loads.

The simplest and most suitable technique for this system is aluminum work hardening. Although low thickness is also necessary for proper pressurization, it can be adjusted based on the material's yield pressure. Work hardening, especially with aluminum, is a proven technique in space applications. It has been successfully implemented in projects like ECHO 2 [14] and InflateSail [68]. **Therefore, this design adopts aluminum work hardening as its rigidization method.**

2

Preliminary Design and Research Question

This chapter outlines the primary design requirements for the drag sail system and presents the initial design iteration done by the company. Following this, the research objectives and questions are introduced, as this project builds on an existing design. From the initial iteration, two key aspects of the design will be investigated. Firstly, the sail size, which involves estimating the orbital decay time, and secondly, the system's capacity to sustain the environmental mechanical loads.

2.1. Preliminary Design

Demcon High-tech Systems is working on the design of a post-mission disposal system, following the ESA tender project: *In-orbit Experiment of an Inflatable De-orbiting Drag Device for Small Satellites* [16]. This section contains the requirements from the tender project and a description of the initial design.

2.1.1. Tender Requirements

ESA requirements for the De-orbiting Drag Device are summarized in Table 2.1.

Table 2.1: Requirements given by the ESA tender description [16].

ID	Requirement	Description
RS-01	The system shall reduce the deorbit time by a factor of 5 in comparison to the natural orbit decay.	Driving purpose of the project, minimize future space debris in LEO.
RS-02	The maximum decay time shall be 10 years.	Requirement that constrains RS-01.
RS-03	The system shall be designed for an initial altitude range of 450 km to 650 km.	LEO altitude, due to high debris concentration.
RS-04	The system shall be able to deorbit small satellites (<200 kg mass).	System meant for CubeSats and small satellites, which are the current problem in LEO.
RS-05	The system shall employ an inflatable solution.	Structural design requirement.
RS-06	The system shall be designed as simple as possible.	Minimize breakdown chances.

RS-07	The system shall have a high level of reliability.	Minimize breakdown chances.
RS-08	The system shall be compatible with volume production requirements.	Intended for large volume production, thus easy manufacture.
RS-09	The system shall allow integration within the existing platform.	Independent of host satellite design. Attachable module.
RS-10	The system shall be scalable for a range of small satellite sizes.	Not designed for a specific mission, need to deorbit satellites from 1 kg to 200 kg.
RS-11	The system shall have a low mass-to-volume ratio.	Slight increase in mass due to the addition of the deorbit module.
RS-12	The system shall be able to survive micrometeorite impacts.	If hit by already existing debris, be able to deorbit and not create additional debris.
RS-13	The system shall incorporate a backup passive activation system.	Enable fail-safe actuation at the end of the mission or for out-of-control tumbling satellites.
RS-14	The actuation time shall be tuneable commensurate with the mission lifetime.	The subsystems used need to withstand long-term packaging.

2.1.2. Design Description

The company made an initial design of the deorbit system and manufactured a prototype to test the drag sail deployment concept and its manufacturing feasibility.

Deployment System Design

The deployment of the sail is actuated by four inflatable booms. The booms will eject the drag sail at the EoL of the host spacecraft, complying with RS-05. The deployment mechanism that guides the booms out of the enclosure is based on four sliding platforms where the booms rest. These platforms will carry the booms out of the enclosure and lock them with a defined angle for a correct sail deployment. The sail is folded around a center pole using a single-sheet folding pattern. This pattern was first proposed by Cambridge Consultant for a solar sail design and is based on a patent by Huso in 1960 [54].

Figure 2.1 shows the deployed configuration of the preliminary design. Figure 2.1a shows the CAD model, where the sail pole and the sliding platforms are visible, and Figure 2.1b shows the prototype after the deployment test.

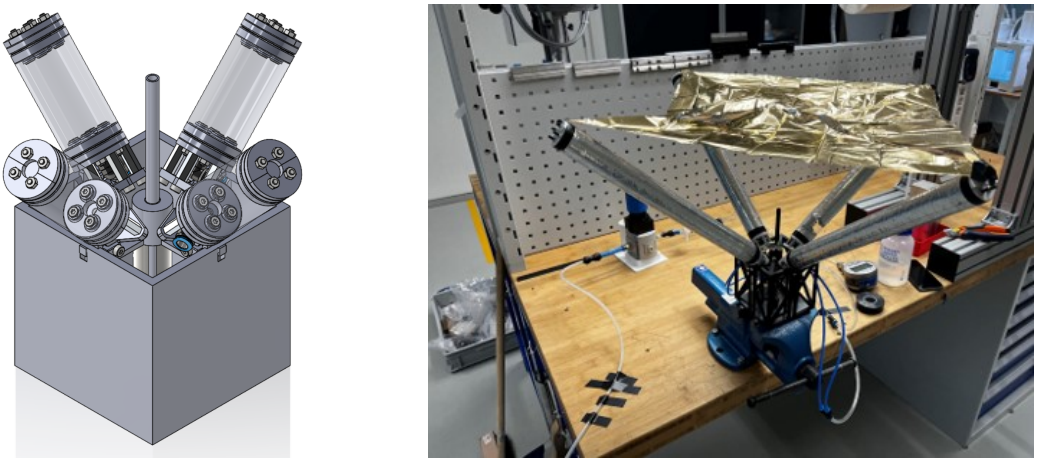

(a) CAD model. **(b)** Prototype.

Figure 2.1: Deorbiting module preliminary design.

Sail Sizing

The company adopted the following methodology to determine an initial approximation of the sail area to comply with the decay time requirement (RS-01). Atmospheric drag was taken as the only source of decay for the company's preliminary study. Thus the velocity of the system decreases as shown in Equation 2.1.

$$\vec{v_{i+1}} = \vec{v_i} + (\vec{a_d})_i dt \tag{2.1}$$

where v is the satellite's velocity, a_d is the deceleration due to the drag force, and dt is the time difference between two consecutive points. The subscript i represents the current time point, while i+1 denotes the subsequent time point.

The effective area is the design parameter for a drag augmentation system, as this geometric magnitude can be easily modifiable. For a first approximation of this sail area, the company assumed a uniformly accelerated motion of the spacecraft. And stated that increasing the acceleration by a factor of 5 would increase the velocity by the same factor, reducing the decay time to comply with RS-01. Following this reasoning, the sail was sized using Equation 2.2, and in the case of exceeding the 10-year maximum decay time, it will follow Equation 2.3.

$$A_{\text{sail}} = 5\frac{C_{d\,\text{sat}}}{C_{d\,\text{sail}}} A_{\,\text{sat}} \qquad \text{if } t_{\text{deorbit sail}} < 10 \text{ years} \tag{2.2}$$

$$A_{\text{sail}} = \frac{t_{\text{deorbit sail}}}{10}\frac{C_{d\,\text{sat}}}{C_{d\,\text{sail}}} A_{\text{sat}} \qquad \text{if } t_{\text{deorbit sail}} \geq 10 \text{ years} \tag{2.3}$$

where A_{sail} is the effective drag area of the deployed sail, A_{sat} is the effective drag area of the CubeSat before the sail is deployed, $C_{d\text{sail}}$ is the drag coefficient of the sail, $C_{d\text{sat}}$ is the drag coefficient of the satellite and $t_{\text{deorbit sail}}$ is the decay time in the case of deployed drag sail.

The sizing of the sail through this method might give a raw first estimate, but it is not realistic. First of all, even if assuming a uniformly accelerated motion of the satellite through the whole deorbiting process, the velocity will only increase by a factor of 5 if the initial velocity of the system is 0. This is not the case, as we are orbiting with an initial velocity before deploying the drag sail.

Secondly, the acceleration is not constant. As seen in Equation 1.4, the density depends on the spacecraft's altitude, and the velocity decreases with time due to the drag force. This last parameter has a high weight on the atmospheric deceleration, as it is squared, and its variation cannot be neglected.

Since this method does not accurately represent real decay conditions, in this thesis a more accurate sizing of the sail will be performed, to ensure compliance with RS-01. Moreover, an accurate estimation of the sail surface area is important, as the decay forces acting on the sail are directly dependent on its area. These forces are the base for the subsequent structural design of the deorbiting system.

Boom Design

Four inflatable booms hold each corner of the sail to ensure the highest effective drag surface area. These booms were designed based on the inflatable mast from InflateSail [68]. The booms are made of 2 layers, an outer aluminum layer, that provides stiffness to the boom, and an inner Mylar layer, glued to the aluminum layer, that acts as a bladder to avoid air leakage during inflation. Aluminum has the lowest interaction with atomic oxygen of all metals, an important characteristic at LEO where this highly reactive component is abundant. It is also highly malleable, easy to manage, safe, and light [39].

The booms are folded following a Miura origami pattern in the stowed configuration. After the deployment signal is transmitted from the On Board Computer (OBC) or the backup activation system, a cold gas generator inflates the four booms. The booms need to remain stiff after the inflation gas has escaped, as it is impossible to achieve complete airtightness. The stiffening technique proposed to guarantee structural stiffness after deployment was work hardening, the same technique used in the InflateSail project. Further research on the rigidization of the boom is performed in this thesis. The inflation gas will leak passively through the manufacturing imperfections of the boom. The company

estimated a maximum deflation time of 10 minutes. Figure 2.2 shows the booms in a semi-folded configuration, where the origami pattern is visible, and a fully inflated configuration, where no creases are visible, and the boom has been overpressurized.

This preliminary concept of the booms has not been proven to work for the load case corresponding to the orbital decay phase. Designing the booms according to the requirements is the purpose of this thesis, therefore iterations in the the dimensions, inflation process, materials and design will follow.

(a) Semi-folded configuration.

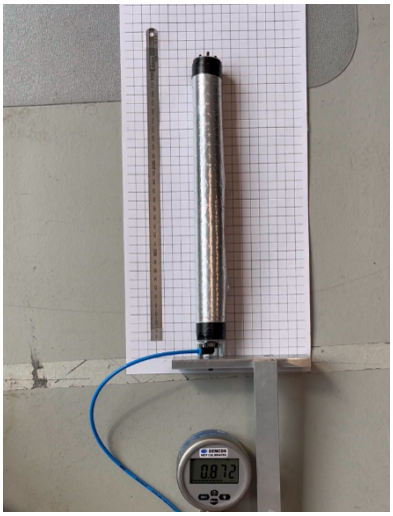

(b) Fully deployed configuration.

Figure 2.2: Preliminary boom design prototype.

2.1.3. Demcon Requirements

Demcon stated one main mission requirement, based on the possible future clients, and three system requirements, based on the deployment system design made.

Table 2.2: Demcon requirements.

ID	Requirement	Description
RC-01	The system shall be able to deorbit 6U and 12U CubeSat.	Mass and Area of host spacecraft definition. This requirement narrows down the host spacecraft characteristics from RS-04.
RC-02	The system in stowed configuration shall not be bigger than 1.5U.	Constrain in stowed volume.
RC-03	The system shall maintain the boom radius of the prototype (1.5 cm).	Requirement based on the deployment system design.
RC-04	The system should maintain the boom length of the prototype (30 cm).	Requirement based on the deployment system design.
RC-05	The system should maintain the boom inclination angle of the prototype (50°).	Requirement based on the deployment system design.

2.2. Research Question

The objective of this thesis is to advance the understanding and application of drag sail systems for CubeSats in LEO, specifically focusing on systems deployed via inflatable structures. The research comprises two primary areas: a preliminary sizing of the drag sail system's sail, and a structural analysis of the drag sail and its inflatable booms to ensure the design withstands the environmental mechanical loads.

Accurately estimating orbital decay time is important for determining the appropriate drag sail area needed to reduce the host spacecraft's natural decay time by a factor of five, as required by the project requirements. The primary goal is to develop a numerical model that can estimate the decay time of a CubeSat in LEO. This model will enable the sizing of the drag sail, ensuring the spacecraft complies with end-of-life disposal guidelines.

The structural analysis focuses on assessing the suitability of inflatable booms as load-bearing elements in the space environment. Inflatable structures offer significant benefits, such as minimal packaging volume, low mass, and adaptability in design. However, challenges with gas retention need to be addressed. This research will investigate strain rigidization as a post-deployment rigidization technique to enhance the structural stability of inflatables, with a specific emphasis on their load-bearing capacities when integrated within drag sail systems for CubeSats.

The following research question and sub-questions were established from the preceding discussion.

How can an inflatable drag sail system be designed to effectively reduce the orbital decay time of CubeSats in Low Earth Orbit while withstanding the mechanical loads throughout the deorbiting phase?

- How can a numerical model be developed to estimate the orbital decay time of a CubeSat in Low Earth Orbit?
- How can be the sail area estimated to meet the project's primary requirement of reducing the CubeSat's natural decay time by a factor of five?
- How can the drag sail and inflatable deployable booms be designed to withstand the mechanical loads during deployment and decay?

Part I

Orbital Decay

3

Orbital Decay Model

This chapter presents the orbital decay model, detailing its general framework and the introduction of various orbital perturbing accelerations. A special focus is given to atmospheric drag perturbation, as it is the main driver of orbital decay [73]. For the atmospheric drag perturbation, two atmospheric models, two ways of estimating the drag coefficient and three effective drag area cases were studied.

The model is implemented in Python, utilizing the Tudat libraries [11], which offer flexibility through code modification and the ability to add custom features. This adaptability allows for a more accurate representation of this study´s specific design scenario. A validation of the model is done using telemetry data from three decayed CubeSat.

3.1. General Framework

The reference frame used for this model is an inertial reference frame, with J2000 frame orientation and the Earth as its center. By using this orientation, the z-axis aligns with the North Pole, and the XY plane passes through the Equator as of the J2000 time Epoch. The starting Epoch for all simulations has been set to January 1^{st}, 2000. By doing this the initial time for all simulations will be at 0 s, simplifying the post-processing of the results [11].

Determining the final altitude at which to consider the system fully decayed presented a challenge, as no single altitude is applicable for all satellite missions and configurations. It is shown that at an altitude of 160 km - 120 km, the atmospheric drag will naturally decay the system in a few days, finally disintegrating into the atmosphere due to high thermal loads [74]. To establish a suitable limit, telemetry data from the Delfi-C3 and Delfi-PQ CubeSat missions was referenced, which extended down to altitudes of 200 km and 160 km, respectively. Additionally, decay monitoring for GeneSat-1 and EcAMSat CubeSats concluded at approximately 150 km. Based on this information an altitude of 160 km was chosen as the final decay altitude for this analysis.

The CubeSat has been modeled as a point mass. Tudat has the option to define the geometry of the body, allowing for more exact results for surface and attitude-dependent variables like drag force or solar pressure. This process is computationally expensive, and not suitable for long-period simulations as is the case of orbital decay, which can take decades. The initial position of the satellite is defined by the six Keplerian elements.

The ephemerids and rotation models of the celestial bodies were already included in the Tudat libraries. Tudat used SPICE modules developed by NASA's Navigation and Ancillary Information Facility (NAIF) [47]. These models are commonly used in the space sector to analyze and design planetary missions. The shape of the celestial bodies is approximated by a sphere. The radius is approximated as the average radius of the body, obtained from the SPICE model [11].

Three numerical integrators RK4(5), RK5(6), and RK7(8), have been compared to determine the most effective solving method.

3.2. Perturbations

Figure 3.1 illustrates the impact of the perturbing accelerations at various altitudes. For the current study, the focus will be on perturbations that significantly affect orbits from 650 km downward, following RS-03. These include Earth's gravity, the J2 effect, solar and lunar gravity, solar pressure, and atmospheric drag.

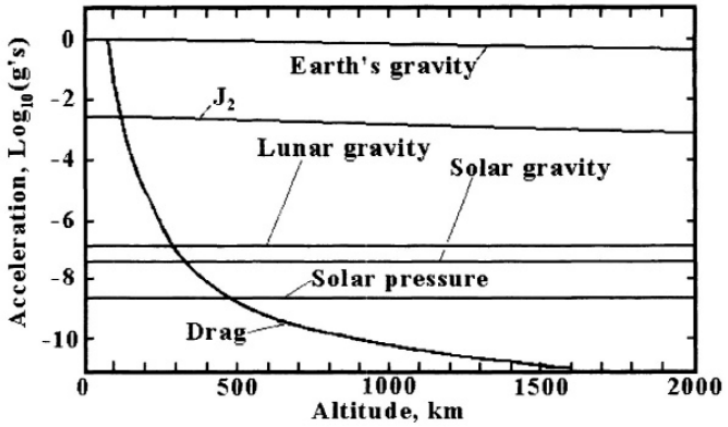

Figure 3.1: Perturbing influences on an orbiting spacecraft [58].

3.2.1. Atmospheric Drag

As previously mentioned, atmospheric drag is the primary factor driving orbital decay [73]. In this model, the stream flow has been assumed perpendicular to one of the surfaces of the CubeSat, therefore no lift or side forces have been introduced. No atmospheric wind has been taken into account either. Estimating the atmospheric density, the drag coefficient and the drag area with precision presents significant challenges [69]. This study analyses and compares two different methods for estimating the atmospheric density and drag coefficient and three approximations for the effective drag area.

Atmospheric density

The density of the upper atmosphere is influenced by a combination of factors, including the nature of its molecular structure, the amount of solar radiation it receives, and its interaction with Earth's magnetic field. These factors are time-dependent; therefore, it is very complicated to accurately estimate the density of the upper atmosphere. There are two main types of density models, time-varying models, which are computationally more expensive, but take into account the dynamic behavior of the upper atmosphere, and static models, which are simpler and less accurate, modeling a neutral density [69]. The accuracy of neutral methods is estimated to be between 10% and 15% in mean solar activity conditions, and up to 100% in local and momentary variations [43].

The two atmospheric models compared in this study are the US Standard Atmosphere 1976 (US76) steady model [51] and the NRLMSISE-00 time-dependent model (Naval Research Laboratory Mass Spectrometer and Incoherent Scatter Radar Extended 2000) [55], both commonly used in the design of planetary missions.

The **US76 model** uses averaged steady conditions of the atmosphere to deliver the density and temperature profiles up to 1000 km altitude. This static model doesn't take into account the dynamic behavior of the upper atmosphere. In the orbital decay model, US76 is defined using tabulated data for density, pressure, and temperature, covering altitudes from 5 km to 1000 km. These parameters are already implemented in the Tudat library [11].

The **NRLMSISE-00 model** is a more detailed atmospheric model, which provides a precise description of the molecular composition of the atmosphere. This model accounts for solar radiation and geomagnetic activity through time-dependent parameters like F10.7 (solar flux) and Ap (geomagnetic index). NRLMSISE-00 allows to estimate the temperature and density profile in the near future based on the past recorded tendency. The data needed to implement this model was obtained from celestrak [8]. Figure 3.2 shows the 10.7 data from 1957 to the present, along with predicted values up to 2041.

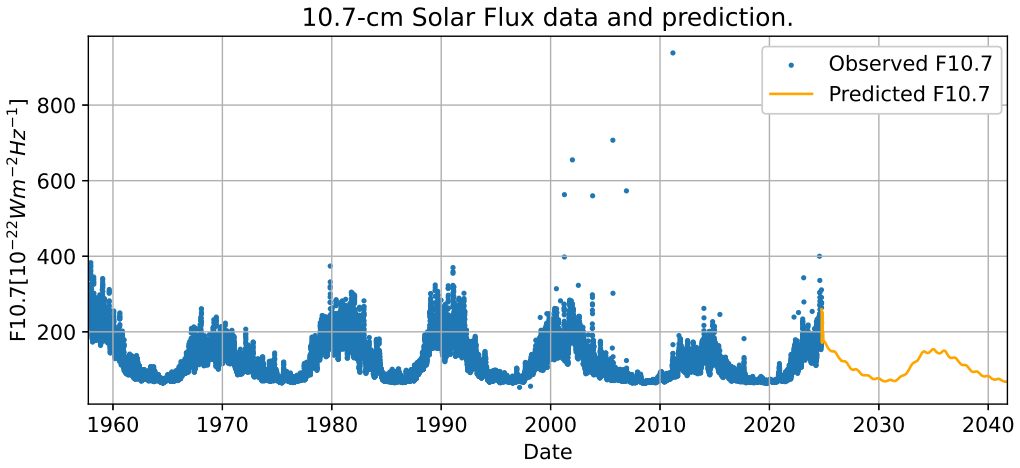

Figure 3.2: 10.7-cm Solar Flux data and prediction [8].

To conduct the long-term natural decay analysis for the CubeSats, the initial data from the NRLMSESI-00 model (originating in 1957) was adjusted to match the initial decay epoch of 2000. This adjustment ensured that the model had sufficient atmospheric data to run an extended decay simulation, taking into account that solar activity was at its peak in both 1957 and 2000. Some modifications of the NRLMSISE-00 atmospheric parameters were required to incorporate the atmospheric model into the orbital decay model. Appendix A outlines these modifications.

Flow regime − Drag Coefficient

The aerodynamic flow regime of a satellite varies along the re-entry trajectory. This flow regime can be determined by the Knudsen number K_n, defined in Equation 3.1 [34].

$$K_n = \frac{\lambda_{mol}}{L_{ref}} = \frac{m_p}{\sqrt{2}\pi\sigma^2\rho L_{ref}} = \frac{M}{N_A\sqrt{2}\pi\sigma^2\rho L_{ref}} \tag{3.1}$$

where λ_{mol} is the mean free path length of air molecules, L_{ref} is a characteristic length of the entry object, m_p is the particle mass, σ is the particle collision diameter, ρ the atmospheric density, M is the molar mass, and N_A is the Avogadro's number.

Three main flow regimes are defined based on this parameter [34]:

- Free molecular flow regime: Kn > 10
- Transitional regime: 0.01 < Kn < 10
- Continuum regime: Kn < 0.01

For this study, the decay was simulated up to an altitude of 160 km. L_{ref} was estimated to be 0.3 m, the biggest length of the 6U and 12U CubeSat configurations following RC-01. The molar mass and collision diameter of the main particles that compose the atmosphere are summarized in Table 3.1.

Table 3.1: Molar masses and collision diameters for the major atmospheric components [41].

Element	M [kg/mol]	σ [pm]
N2	28.0	370
O2	32.0	358
N	14.0	290
O	16.0	280
He	4.0	256
Ar	39.9	340
H	1.0	260

The molar mass and collision diameters summarized in Table 3.1 are valid up to an altitude of 100 km. Above this altitude gaseous diffusion is more significant, leading to a change in the composition of the atmosphere. The number density (n_i) or concentration of the main particles that compose the atmosphere at different altitudes can be obtained from the NRLMSISE-00 density model, thus an averaged value of the mass and collision parameter of each element can be calculated following Equation 3.2 and Equation 3.3 [41].

$$M_{avg} = \sum_{i=0}^{N} M_i \frac{n_i}{n_{tot}} \tag{3.2}$$

$$\sigma_{avg} = \sum_{i=0}^{N} \sigma_i \frac{n_i}{n_{tot}} \tag{3.3}$$

To determine the flow regime of the satellite, before implementing the full method into the orbital decay model, the number density of the atmospheric particles was obtained from the ECSS-E-ST-10-04C – Space environment (15 November 2008) standard [20]. This standard summarizes the density, temperature, and number density of the atmospheric particles for the different altitudes for the low, mean, and high solar activity cases. Table 3.2 defines the main solar activity parameters for these scenarios.

Table 3.2: Solar Activity Parameters for the three solar activity cases defined in the ECSS-E-ST-10-04C standard [20].

Parameter Name	Mean Solar Activity	Low Solar Activity	High Solar Activity
F10.7 [sfu*]	140	65	300
F10.7avg [sfu*]	140	65	250
S10.7 [sfu*]	125	60	235
S10.7avg [sfu*]	125	60	220
M10.7 [sfu*]	125	60	240
M10.7avg [sfu*]	125	60	220
Ap [-]	15	0	240

* sfu stands for solar flux units, 1 sfu = 10^{-22} W/m^2/Hz

where F10.7 is the Solar Flux Index, F10.7avg is the Average Solar Flux Index, S10.7 is the Short-Wavelength Solar Index, S10.7avg is the Average Short-Wavelength Solar Index, M10.7 is the Medium-Wavelength Solar Index, M10.7avg is the Average Medium-Wavelength Solar Index and Ap is the Geomagnetic Index.

Figure 3.3 shows the magnitude of the Knudsen number at the different altitudes, for the three atmospheric cases studied. A close-up look near the final simulated decay time is shown in Figure 3.3b.

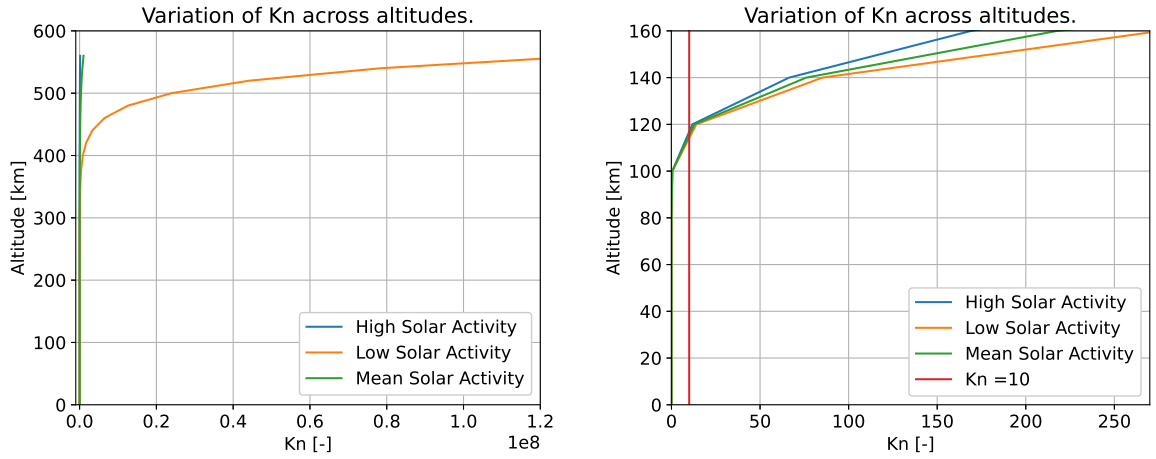

(a) Kn for the full altitude range.

(b) Kn up to the final simulated decay altitude.

Figure 3.3: Variation of Knudsen Number Across Altitudes for Three Atmospheric Conditions for a 6U and 12U CubeSat.

As it can be seen the complete simulated orbital decay (from 650 km altitude to 160 km altitude) of the CubeSat for the three solar activity cases, can be assumed to be in the **free molecular flow aerodynamic regime**. Changing to the transition regime at an altitude of around 120 km. To introduce the characteristics of this regime in the drag force calculations, the engineering approach defined by K. Hart in *Analytically-derived Aerodynamic Force and Moment Coefficients for Resident Space Objects in Free-Molecular Flow* [25], was applied.

K. Hart [25] introduces the *free molecular flow regime in the drag force calculation by a redefinition of the pressure coefficient (C_P) normal to the surface and the shear pressure coefficient (C_T) tangent to the surface.* In this study, the stream flow has been assumed perpendicular to the CubeSat surface at all points in the decay ($\theta = 90°$). Therefore, the tangential component of the pressure coefficient is null, and only the normal component remains, thus, in this case, $C_P = C_d$. Equation 3.4. defines the redefinition of the drag coefficient [25].

$$C_P = \frac{1}{s^2}\left[\left(\frac{2-\sigma_N}{\sqrt{\pi}} s\sin\theta + \frac{\sigma_N}{2}\sqrt{\frac{T_w}{T_\infty}}\right) e^{-(s\sin\theta)^2} + \left\{(2-\sigma_N)\left((s\sin\theta)^2 + \frac{1}{2}\right) + \frac{\sigma_N}{2}\sqrt{\frac{\pi T_w}{T_\infty}} s\sin\theta\right\}(1+\operatorname{erf}(s\sin\theta))\right] \tag{3.4}$$

$$s = \frac{V_\infty}{\sqrt{2R_{gas}T_\infty}} \tag{3.5}$$

where σ_N is the normal momentum accommodation coefficient, s is the freestream molecular speed ratio, analogous to the Mach number and defined in Equation 3.5, T_∞ is the freestream temperature, V_∞ is the freestream velocity, T_w is the wall temperature and R_{gas} is the gas specific constant.

The momentum accommodation coefficient defines the molecule-surface interaction and can be classified as diffuse ($\sigma_N = 1$) or specular ($\sigma_N = 0$) [25]. The most common case is diffuse reflection, thus $\sigma_N = 1$ was used for this study. The temperature of the freestream flow is obtained from the atmospheric density model, and the ratio between the flow stream temperature and the wall temperature has been assumed to be 1.

The second and simpler method used to determine this coefficient is assuming a **continuum aerodynamic regime with a C_d of 2.2**, applying the flat plate model. This is a common assumption used for preliminary studies [69].

Drag Area

Estimating the drag area is challenging, as the satellite may tumble throughout the decay phase, making it a time-dependent variable. In previous projects, such as InflateSail and CanX-7, the drag sail was offset from the CubeSat's center of mass to achieve a favorable aero-stable attitude. In the current design, this offset is provided by deployable inflatable booms; however, passive stability has not yet been investigated.

Based on the initial assumption that the airflow is always perpendicular to the drag surface, a constant effective drag area is assumed throughout the decay phase. Three values are considered for this effective area: **the average of the CubeSat's outer surface areas, the smallest outer surface area, and the largest outer surface area**. The influence of these area estimates will be analyzed during the model validation in Section 3.5.

3.2.2. Solar Pressure

Solar radiation that hits the spacecraft can arrive from two different routes, the direct reflection of solar radiation on the spacecraft, and the albedo, the reflected Sun radiation from the Earth [19]. Only the direct radiation from the Sun has been considered for the decay model. The Albedo magnitude depends on the reflectivity of the Earth, commonly estimated to be 0.3 [19], therefore the weight of the Albedo in the overall solar pressure perturbing acceleration can be neglected. Moreover, the albedo will have

a higher effect on the spacecraft the closer the satellite is to the Earth [19], when the drag force will dominate the decay.

An isotopic model is used to define the radiation of the source, the Sun. In this model, the Sun is a point source where the radiation depends solely on its distance to the target, rather than on the source's relative latitude or longitude. The model also assumes the incoming rays to be parallel. These assumptions are valid when estimating the radiation from distant sources. The satellite was assumed to be at 1AU and the radiant power of the Sun to be 3.828E26 W [11].

The Cannonball target model was selected for the satellite, where the body is approximated as an isotropic sphere, characterized by its cross-sectional area and radiation pressure coefficient (C_r). This model is well-suited for lower-fidelity simulations, as it is computationally less expensive. A more accurate representation could be achieved using a paneled model, where the spacecraft surface is discretized into panels, and the interaction of radiation with each panel is individually calculated. However, since orbital decay can span several decades, employing the paneled model would be very computationally expensive. Additionally, the perturbative acceleration due to solar radiation pressure is at least one order of magnitude lower than atmospheric drag, making the computational expense of the paneled model unnecessary in this context.

Finding a single equivalent cross-section area and C_r that hold at all times is virtually impossible [66]. Therefore, as a first approximation, the cross-section area will be the average of the six outer surface areas of the CubeSat. Assuming MLI will cover the outside surface of the spacecraft, C_r has a value between 1 and 2, as the radiation will not be fully absorbed but not fully reflected. This coefficient is difficult to estimate, and there are not many literature studies on this parameter. The magnitude 1.2 has been chosen, based on the study *Short-term orbital effects of radiation pressure on the Lunar Reconnaissance Orbiter* by Dominic Stiller [66]. The model simulates the eclipse periods.

3.2.3. Gravitational Acceleration

Gravitational forces from the Earth, the Sun, and the Moon had been considered in the model. A point-mass acceleration is used to model the gravitational perturbation of the Sun and the Moon. This simplification is enough for the initial estimation of the decay time, being less computationally expensive than modeling spherical-harmonic accelerations for these two sources.

For the Earth´s gravitational acceleration, a point-mass approximation is not enough. Figure 3.1 shows that the effect of J2 in the perturbing acceleration is not negligible. Therefore a spherical-harmonic acceleration of the Earth, of degree 2 and order 0 was modeled.

3.3. Evaluation of Methods for Modeling Drag Perturbation

The host spacecraft configuration and mission characteristics have not been determined yet, thus the effect of the different density and aerodynamic regime models in the decay time was analyzed for the case of Delfi-C3 [24]. Delfi-C3 is a 3U CubeSat developed by the Technical University of Delft, with a mass of 2.2 kg and an average area of 0.023 m^2. It was launched in April 2008 to a circular orbit at an altitude of 635 km and an inclination of 97.94°.

3.3.1. Atmospheric density

Figure 3.4 shows the density profile during the decay phase of Delfi-C3 for the two atmospheric methods studied, the NRLMSISE-00 (blue) and the US76 (orange). In green, red and purple are the low, mean and high solar activity NRLMSISE-00 average density values obtained from the *ECSS-E-ST-10-04C – Space environment (15 November 2008)* standard [20].

As can be seen, the values from the standard create an accurate envelope of the method. The US76 method is close to the NRLMSISE-00 mean solar activity, but it does not capture the variability of solar radiation and geomagnetic activity, as explained in Section 3.2.

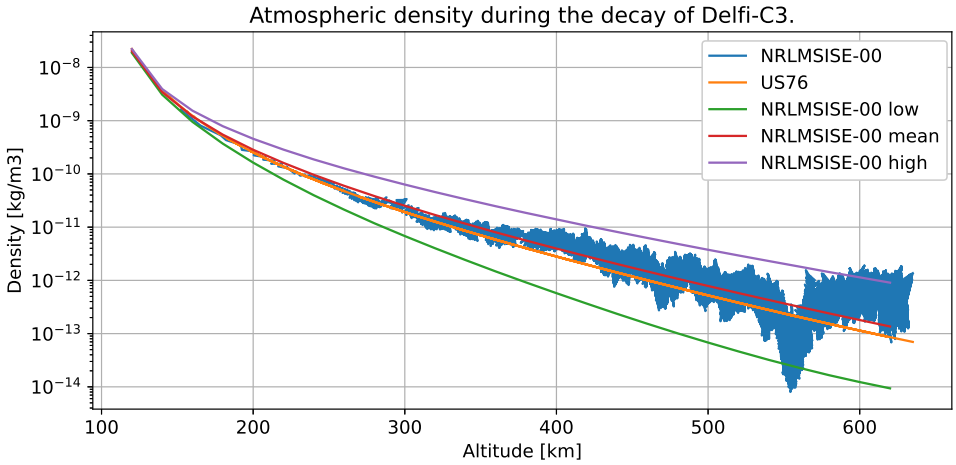

Figure 3.4: Density profile during the decay of Delfi-C3 for the NRLMSISE-00 and US76 atmospheric models.

Figure 3.5 shows the decay profile for the initial conditions of Delfi-C3, varying only in the atmospheric density model. It is important to note that the flow regime used for the calculation of both decay profiles was the free molecular flow. The decay time obtained with the NRLMSISE-00 method is 12.6 years, whereas the decay time obtained with the US76 model is 22.9 years, almost twice the time.

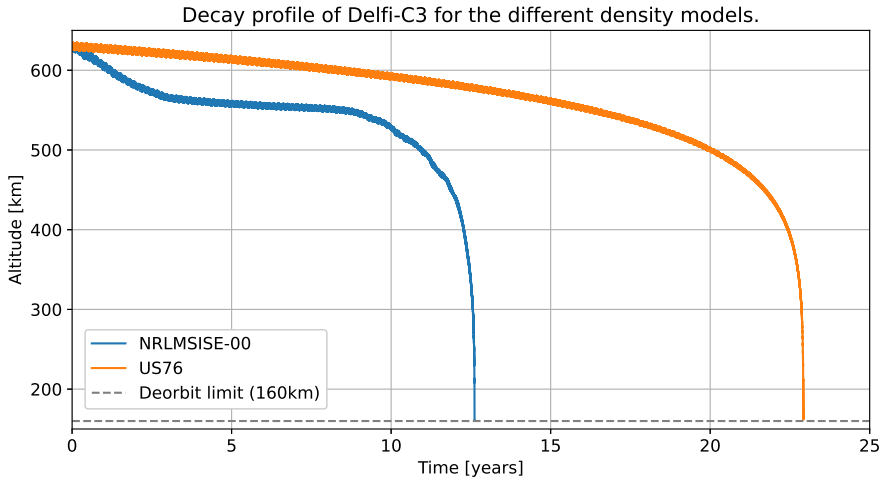

Figure 3.5: Decay profile of Delfi-C3 for the NRLMSISE-00 and US76 atmospheric methods.

3.3.2. Aerodynamic regime – Drag coefficient

Figure 3.6 shows the decay profile of Delfi-C3 for the free molecular flow and continuum flow regimes with constant C_d, using the NRLMSISE-00 atmospheric density model. The decay time of the continuum flow with a C_d of 2.3 and the decay time for the free molecular flow are very close. This is the case because when averaged, the value of the drag coefficient for the freestream flow regime was 2.28.

The continuum flow regime with a C_d of 2.2 and the free molecular flow regime, the two methods defined in Section 3.2, had a difference in the decay time of 4%, negligible when compared to the variation with the different atmospheric density models.

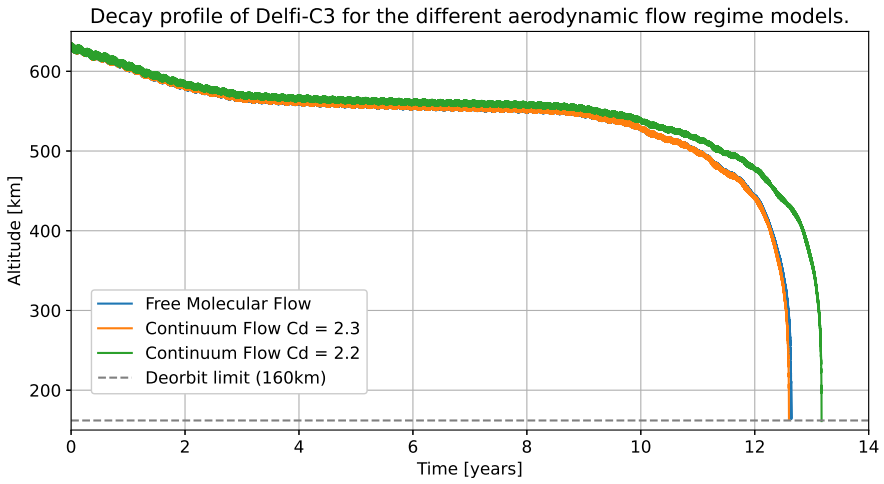

Figure 3.6: Decay profile of Delfi-C3 for the free molecular and continuum aerodynamic regime cases.

Figure 3.7 presents the decay profile of Delfi-C3 for the four different atmospheric drag perturbation models, along with the actual Two Line Element (TLE) decay data for Delfi-C3 [8]. The starting epoch in the graph is 8.5 years, accounting for the CubeSat´s real launch date. This allows the modeling of the real atmospheric conditions during its decay.

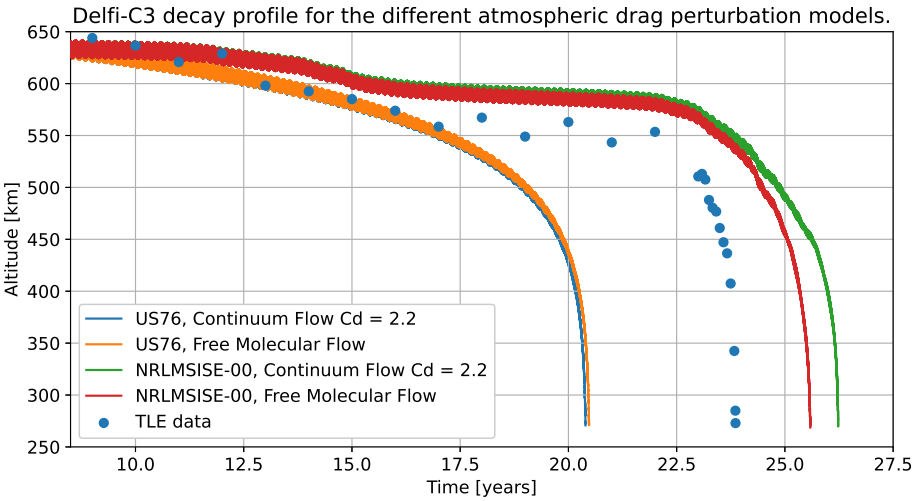

Figure 3.7: Delfi-C3 decay profile for the different atmospheric drag models and real data decay from Space-Track [61].

The US76 model significantly underestimates the satellite's decay time. When combining US76 and the rarefied aerodynamic regime, the change in the decay time is minimal. This is because the atmospheric density in the US76 model is derived solely from neutral atmospheric parameters, not accounting for the molecular composition of the atmosphere and solar and geomagnetic activity, which affect the calculation of the drag coefficient (C_d) in the rarefied flow regime. The small change in decay time is due to minor variations caused by changes in freestream molecular velocity.

In contrast, the NRLMSISE-00 model shows a more pronounced variation when different drag coefficient models are applied, as it accounts for the molecular composition of the atmosphere as well as solar and geomagnetic activity. Consequently, **the combination of the NRLMSISE-00 model and the rarefied flow regime provides the most accurate estimate of the CubeSat's actual decay profile**, as both components more closely represent real atmospheric conditions.

It is important to note that an accurate representation of atmospheric density is more critical than that of the drag coefficient. This is because atmospheric density varied by an order of magnitude between methods in this analysis, while the drag coefficient varied only by tenths of a unit.

3.4. Numerical Integrator

Using fixed-step numerical integrators may lead to long analysis times when high precision is required. Adaptive-step Runge-Kutta determines the optimal time-step size by evaluating the function with two different orders of the method, p and $p+1$, and ensuring the relative error (ϵ) between them is smaller than the error specified by the user. This approach allows the use of smaller timesteps to solve the periods of the orbit where the forces change rapidly, and bigger time steps when these rates of change are smaller. Adaptive-step numerical integrators are an optimal trade-off between accuracy and computational time [56].

A convergence analysis was carried out to determine the method that ensures an accurate result of the decay time with the lowest computational effort. Three different adaptive-step Runge-Kutta methods have been compared, RK4(5), RK5(6) and RK7(8). As the ϵ has to be set by the user, the method will be considered converged when the error allowed ensures a relative error in the decay time smaller than 1% with respect to the previous iteration. As is the case with the Drag Definition Analysis, the convergence analysis was performed for the mission case of Delfi-C3 [24]. Table 3.3 summarizes the results of the convergence of the three different methods.

Table 3.3: Convergence study of the Runge-Kutta adaptive-step integrators based on the error (ϵ) allowed.

Integrator	ϵ [10^{-}]	Decay time [years/months/days]	Relative error [%]
RK4(5)	9.00	12/4/22	-
	10.00	12/7/12	1.79
	11.00	**12/7/21**	**0.19**
	12.00	12/7/22	0.02
RK5(6)	9.00	15/8/9	-
	10.00	12/10/10	-18.05
	11.00	12/8/5	-1.39
	12.00	**12/7/24**	**-0.25**
RK7(8)	9.00	12/7/21	-
	10.00	**12/7/21**	**0.0001**
	11.00	12/7/21	-0.0002
	12.00	12/7/21	0.0013

The methods that comply with the convergence criterion are RK4(5) $\epsilon = 10^{-11}$, RK5(6) $\epsilon = 10^{-12}$ and RK7(8) $\epsilon = 10^{-10}$. To assess the efficiency of the method the number of evaluations of the function and the computational time have been compared. The results are summarized in Table 3.4.

Table 3.4: Efficiency study of the Runge-Kutta adaptive-step integrators based on function evaluations and computational time.

Integrator	Funct. Evaluations	% change	Comp. time [min]	% change
RK4(5)	1.38E+08	164.53	137.21	139.18
RK5(6)	1.18E+08	126.34	144.21	151.40
RK7(8)	5.21E+07	-	57.36	-

RK7(8) is the most efficient method in the use of function evaluations and computational time, with a relative error in the decay time w.r.t. RK4(5) and RK5(6) of -0.01% and 0.06% respectively.

3.5. Validation

The model was validated with three different decayed CubeSat cases, Delfi-C3, GeneSat-1 and EcAMSat. The Two Line Element sets (TLE) of these decayed CubeSat were obtained from Space-Track [61]. TLEs provide the position of a satellite for a given point in time.

Delfi-C3 [24], pictured in Figure 3.8a, was used for the analysis of the density and aerodynamic regime models, in addition to the analysis of the convergence of the propagator. Delfi-C3 was launched on the 28th of April, 2008 to a circular orbit at an altitude of 635 km and an inclination of 97.94°.

GeneSat-1 [15], pictured in Figure 3.8b, is a 3U CubeSat with a mass of 4.1 kg used for biomedical research in space. It was launched on the 16th of December, 2006 to a circular orbit at an altitude of 460 km and an inclination of 40.5°.

EcAMSat [45], pictured in Figure 3.8c, is a 6U CubeSat with a mass of 10.7 kg also used for biomedical research in space. EcAMSat was launched on the 20th of November, 2017 to a 413 km altitude orbit with a 51.6° inclination.

(a) Delfi-C3.

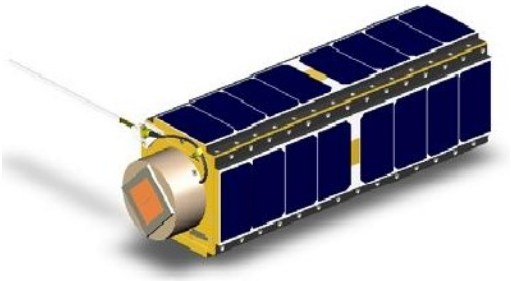

(b) GeneSat-1.

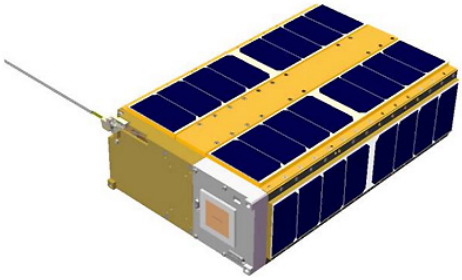

(c) EcAMSat.

Figure 3.8: CubeSats used for the validation of the orbital decay model.

As previously stated, three estimations of the effective drag area have been compared, the mean average area of the outer surfaces of the CubeSat (Mean Drag Area), the smallest of the outer surfaces of the CubeSat (Small Drag Area) and the biggest of the outer surfaces of the CubeSat (Big Drag Area).

Figures 3.9 - 3.11 show the simulated decay profile and the TLE data of the real decay of Delfi-C3, GeneSat, and EcAMSat respectively. In the case of Delfi-C3, the three effective drag areas were simulated, whereas for GeneSat, and EcAMSat only the mean and biggest drag area cases were modeled, as it was seen from the Delfi-C3 case that using the smallest area provided an overly conservative estimation.

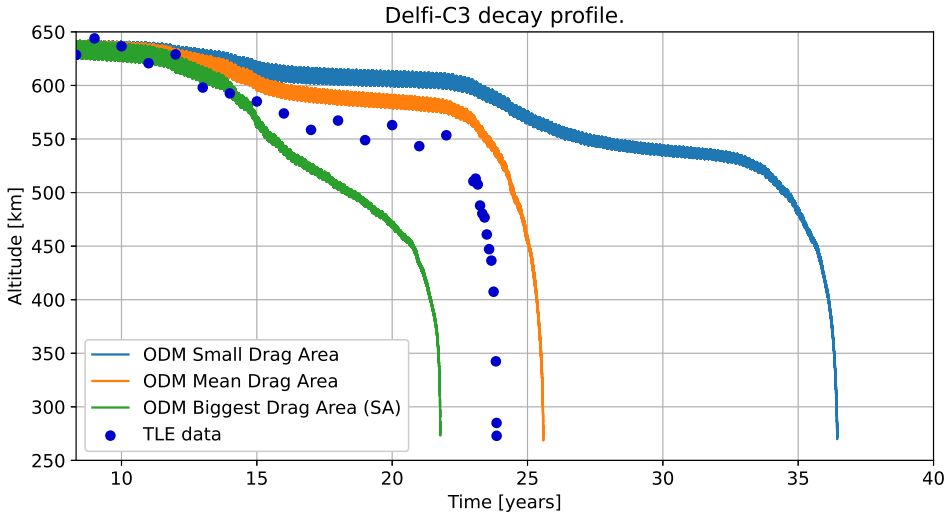

Figure 3.9: Orbital Decay Model of Delfi-C3 for the three effective drag area cases and real decay data (TLE).

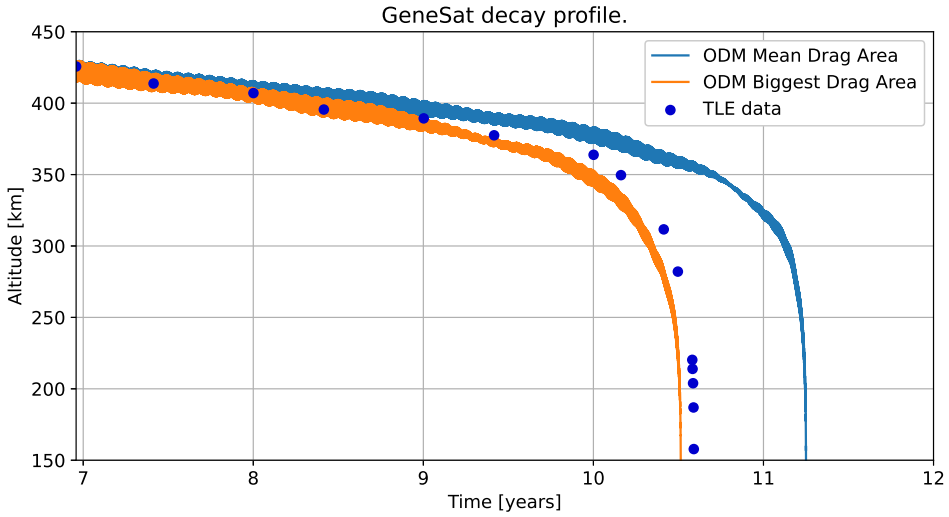

Figure 3.10: Orbital Decay Model of GeneSat-1 for the two effective drag area cases and real decay data (TLE).

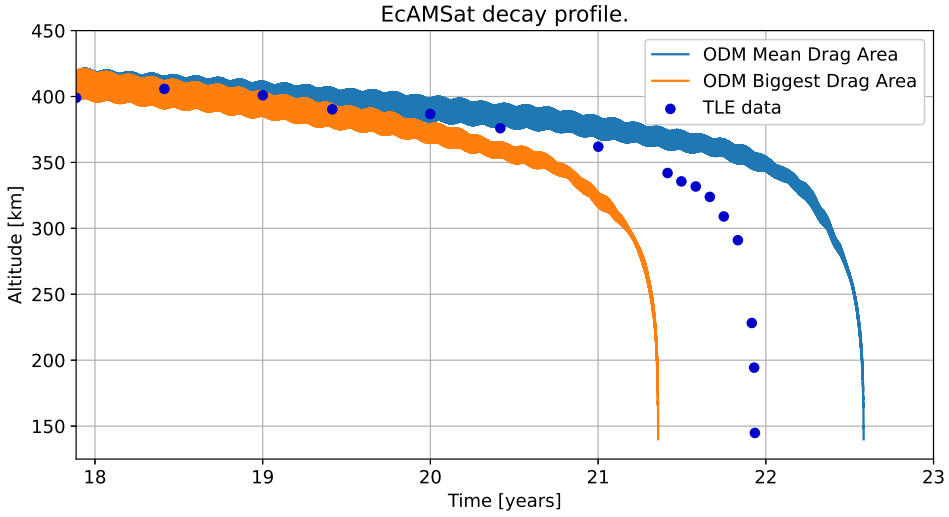

Figure 3.11: Orbital Decay Model of EcAMSat for the two effective drag area cases and real decay data (TLE).

In all three validation cases, the real decay time lies between the mean and big simulated areas. Table 3.5 shows the difference between the decay times of each satellite for the three efficient drag areas studied, and their difference with the real decay time obtained from the TLE data points.

Table 3.5: Deorbit time (DT) of the studied effective drag area cases for the three validation CubeSats and their difference with the mean effective drag area case.

CubeSat	Area models	DT [years]	Difference with mean case [%]	TLE DT [years]	Difference with TLE DT [%]
Delfi-C3	Small	36.44	42.46	23.86	52.74
	Mean	25.58	-		**7.21**
	Big	21.78	-14.86		-8.71
EcAMSat	Mean	22.58	-	21.93	2.96
	Big	21.36	-5.43		**-2.63**
GeneSat	Mean	11.25	-	10.59	6.23
	Big	10.51	-6.55		**-0.72**

Delfi-C3 has the highest difference in decay time between the three validation cases. This is due to the use of four 30 cm x 10 cm deployable solar arrays. The arrays have a 35° deployable angle, therefore their projection in the plane of the small area has been taken into account for the big and mean effective area estimations. As the projection of the solar arrays was used in the mean case, it pushed the average effective drag area up, making the mean case the closest to the real decay time. In the case of EcAMSat and GeneSat, the real decay time is closest to the big drag area case. The simulation results are more accurate in the cases where the CubeSat has the solar panels adhered to the main body.

From the results obtained, it can be seen that using the mean area for the model leads to a conservative result. This result is not overly conservative, thus **using the mean area of the CubeSat as the effective drag area is a good approximation**.

4

Sail Sizing and In-Orbit Loads

This chapter focuses on the sizing of the drag sail and the analysis of the in-orbit loads. First, the host spacecraft mission and geometry are defined, building upon common CubeSat LEO missions, as no specific mission is provided in the requirements. The drag sail is then sized to reduce the natural decay time of the spacecraft by a factor of five, using the area-to-mass ratio as the primary design parameter. The efficiency of the drag sail as a post-mission disposal solution for CubeSats in LEO is also shown.

Some high-risk factors that could shorten the drag sail's operational life are analyzed. From the three main high-risk factors studied, the high structural loads during orbital decay will be further analyzed. These loads will serve as the input for the second part of this project, the structural analysis of the drag sail system.

4.1. Host Spacecraft and Mission

From the requirements given for the design of the drag sail system, stated in Chapter 2, only four address the host spacecraft configuration and mission. These requirements are:

- RS-01. The system shall reduce the deorbit time by a factor of 5 in comparison to the natural orbit decay.
- RS-02. The maximum decay time shall be 10 years.
- RS-03. The system shall be designed for an initial altitude range of 450 km to 650 km.
- RC-01. The system shall be able to deorbit 6U and 12U CubeSat.

To define the host spacecraft mission and geometry, the six Keplerian orbital elements that define an orbit, and the two CubeSat configurations proposed in the requirements were studied. Figure 4.1 illustrates the following six Keplerian parameters [69]:

- Length of the semi-major axis (a), largest radius of the elliptical orbit.
- Eccentricity (e), measures how the elliptical orbit deviates from a circle.
- Inclination (i), measures the angle between the orbital plane and the Earth´s equator.
- Right ascension of the ascending node (Ω), measures the angle in the equator plane from the reference direction (Vernal equinox) to the ascending node of the orbit.
- Argument of periapsis (ω), measures the angle in the orbital plane, from the ascending node to the perigee.
- True anomaly (ν), measures the angle in the orbital plane between the perigee and the position of the orbiting body.

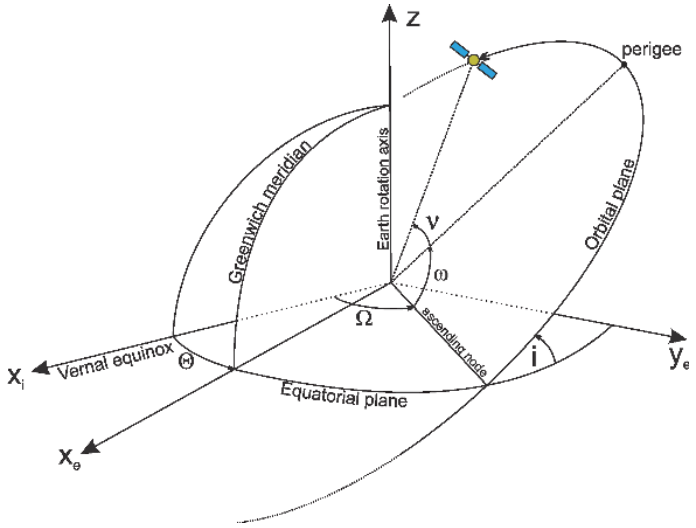

Figure 4.1: Satellite orbit defined by its Keplerian elements in the inertial frame [75].

The Delfi-C3 mission case (main parameters summarized in Table 4.1) has been used as the base case to determine the host spacecraft mission characteristics, by studying how the change in the different Keplerian elements and the CubeSat configurations change the decay time. To fairly analyze the influence of the studied parameters on the decay time, the US76 density model and the continuum aerodynamic flow regime with a C_d of 2.2 have been used for the simulations, getting rid of the random influence in the density and C_d due to the variable solar and geomagnetic activity.

Table 4.1: Orbital parameters and geometric parameters of the base case.

Parameter	**Magnitude**
Semi major axis	600 km
Inclination	97.94°
Eccentricity	0.0
Right Ascension of Ascending Node	0°
Argument of Periapsis	0°
True Anomaly	0°
Mass	2.2 kg
Average Surface Area	0.023 m^2

The right ascension of the ascending node (Ω), the argument of periapsis (ω) and true anomaly (ν) had low influence in the decay time of the CubeSat, thus these three angles have been set to 0°.

4.1.1. Length of the major axis

The initial altitude of the orbit was studied to determine the length of the semi-major axis. Requirement RS-03 states that the system shall be designed for an initial altitude of 450 to 650 km. Figure 4.2 shows the decay profile of Delfi-C3 for the initial altitudes of 450, 500, 550, 600, and 650 km. As can be seen, the decay time strongly depends on the initial altitude. The higher the initial altitude is, the less atmospheric density the system encounters, therefore smaller drag forces arise at the initial stages, delaying the natural decay of the CubeSat.

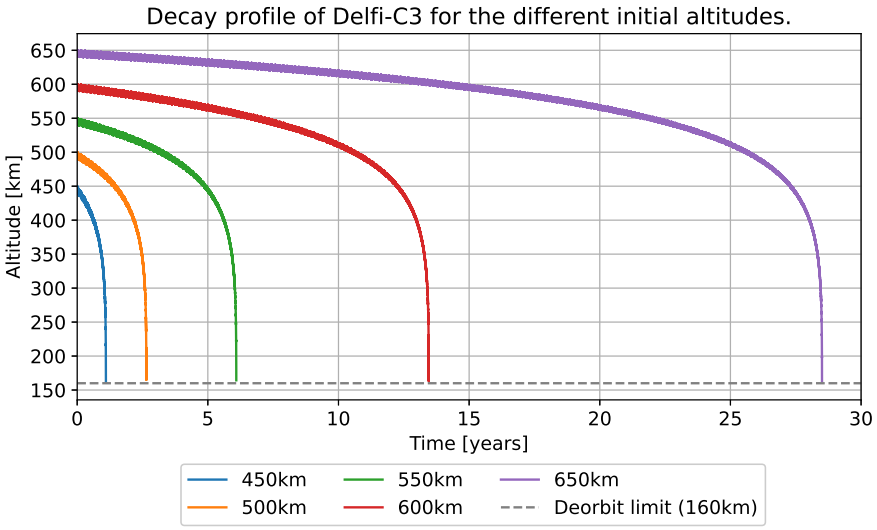

Figure 4.2: Decay profile of Delfi-C3 for different initial altitudes.

One fixed design does not effectively fit the whole initial altitude range. It is safe to say that, if the design is made for the worst-case scenario, an altitude of 650 km, it will comply with requirement RS-03 for all the remaining cases, but it will not be an efficient design. The lower the initial altitude, the smaller the drag sail area needed to comply with RS-01.

Figure 4.3, obtained from the *2023 Space Environmental Report* by ESA [17], illustrates that the highest concentration of active payloads is located between altitudes of 500 and 600 km, with a significant difference compared to other altitude ranges. Consequently, an initial altitude of 550 km is selected for the host spacecraft. This design choice does not fully comply with RS-03, but it aligns with the majority of payloads launched into LEO.

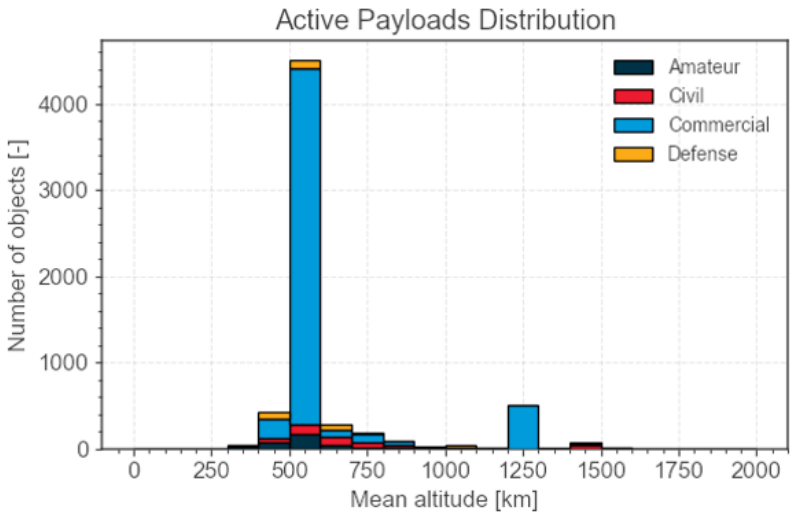

Figure 4.3: Distribution of active payloads at different orbital altitudes [17].

4.1.2. CubeSat Configuration

According to the company's requirement RC-01, the system shall be able to deorbit 6U and 12U CubeSat. An analysis of the decay time for both cases has been done. According to ESA's standard description of CubeSats, each module (1U) has a volume of 10 cm x 10 cm x 10 cm, and a mass of 3 kg [2]. The most common configuration for 6U and 12U CubeSats can be found in *CubeSat Design Specification (1U – 12U)* [33]. Table 4.2 summarizes the mass and average surface area of both configurations.

Table 4.2: Average surface area and mass of a 12U and 6U CubeSat.

6U CubeSat	
Average Area	**Mass**
0.036 m^2	18 kg
12U CubeSat	
Average Area	**Mass**
0.053 m^2	36 kg

Figure 4.4, shows the decay profile for the two configurations stated. The 12U has a 37.5% increment in the decay time compared to the 6U CubeSat. Therefore, the worst case, the 12U configuration, has been used for the host spacecraft definition. This approach meets requirement RC-01, as the 6U configuration achieves the target decay time with a reduction of over five units.

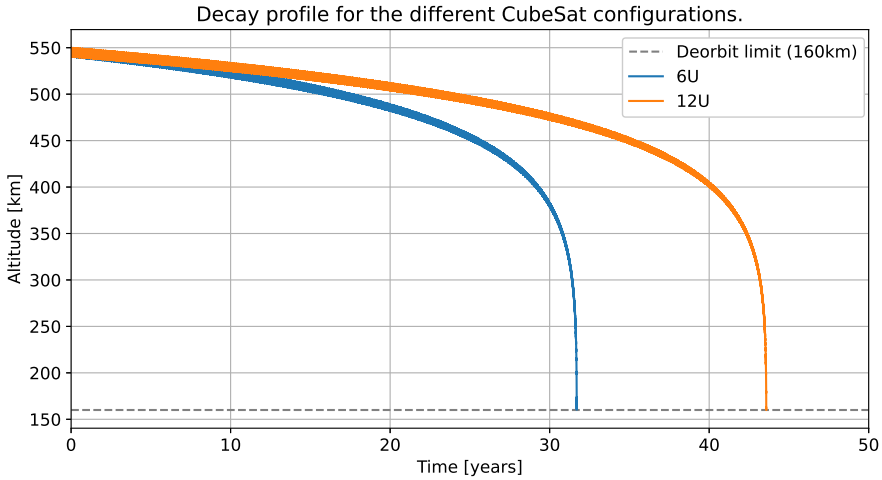

Figure 4.4: Decay profile of the base case mission for the different CubeSat configurations.

The contribution of the mass and the area was analyzed separately using the base case of a 6U CubeSat. When the surface area of the CubeSat was doubled, the decay time was reduced by 48.34%. When the surface area was halved, the decay time increased by 88.18%. Analogously, when the mass was doubled, the decay time was increased by 88.18%, and when the mass was halved the decay time was reduced by 48.34%. When both the area and mass were reduced by half, the decay time was the same as the case of the 6U CubeSat. Figure 4.5 illustrates this sensitivity analysis.

The drag force and the solar pressure are the only two non-conservative perturbations considered in the model, therefore only sources of orbital decay. Their accelerations are directly proportional to the surface area and inversely proportional to the mass, explaining the identical contribution of the change of mass and area on the decay time. In the case of the 12U CubeSat with respect to the 6U, the mass was doubled, but the surface area was only increased by 1.47 times, therefore, it is logical that the decay time of the 12U CubeSat is longer.

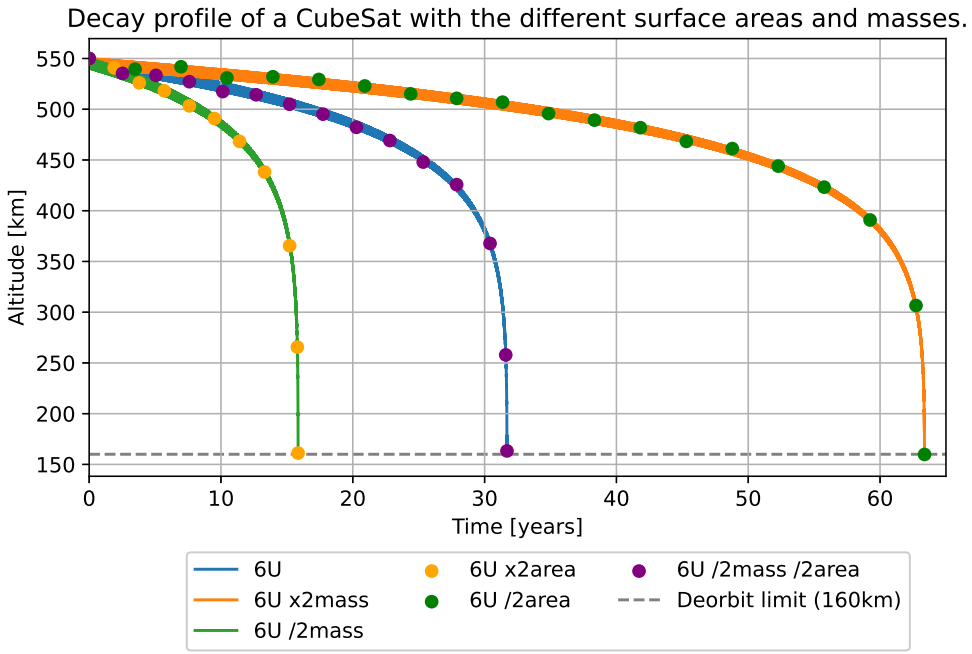

Figure 4.5: Decay profile of the base case mission for the different CubeSat´s geometry and mass configurations.

4.1.3. Eccentricity

The eccentricity of an orbit is delimited by its perigee and apogee radius, following Equation 4.1 [69].

$$e = \frac{r_a - r_p}{r_a + r_p} \tag{4.1}$$

where e is the eccentricity of the orbit, r_p is the perigee radius, distance from the center of the Earth (focal point) to its closest point in the orbit (perigee), and r_a is the apogee radius, distance from the center of the Earth to its farthest point in the orbit (apogee).

Due to the low altitude of LEO, the possible orbital eccentricities are limited, as the perigee altitude cannot be smaller than the Earth's radius. In this design case, the ceiling decay altitude is 160 km, therefore $r_p = Re + 160$ and the apogee radius is $r_a = Re + 550$, where Re is the radius of the Earth. Using these magnitudes and introducing them to Equation 4.1, the maximum eccentricity of the orbit is 0.029.

The decay time was calculated for three different eccentricities, e = 0.025, e= 0.0125, and e = 0, to study the effect of the eccentricity on the decay time. Table 4.3 summarizes this analysis results and shows the decrease in the decay time with respect to a circular orbit (e = 0).

Table 4.3: Decay time analysis of the base case mission for different initial orbital eccentricities.

e = 0				
r_a [km]	r_p [km]	a [km]	DT [years]	Change w.r.t. e=0 [%]
6921.0	6921.0	6921.0	22.87	-
e = 0.0125				
r_a	r_p	a	t_d	Change w.r.t. e=0 [%]
6921.0	6750.1	6835.5	18.51	-19.1%
e = 0.025				
r_a	r_p	a	t_d	Change w.r.t. e=0 [%]
6921.0	6583.4	6752.2	9.94	-56.5%

As it was expected, the worst case will be the decay of a circular orbit. When an orbit is elliptical, its apogee and perigee radius are different. If the apogee radius is kept constant, the perigee radius starts to decrease when increasing the eccentricity, therefore lower altitudes are reached sooner. At lower altitudes, the atmospheric density is higher, leading to a higher drag force earlier in the decay phase, reducing the decay time. An eccentricity of 0 was used for the host spacecraft design case in this study.

4.1.4. Inclination

Six inclination cases were studied to determine the worst decay time case, i = 0°, i = 22.5°, i = 45°, i = 67.5°, i = 78.75°, and i = 90°, where the decay profiles are shown in Figure 4.6.

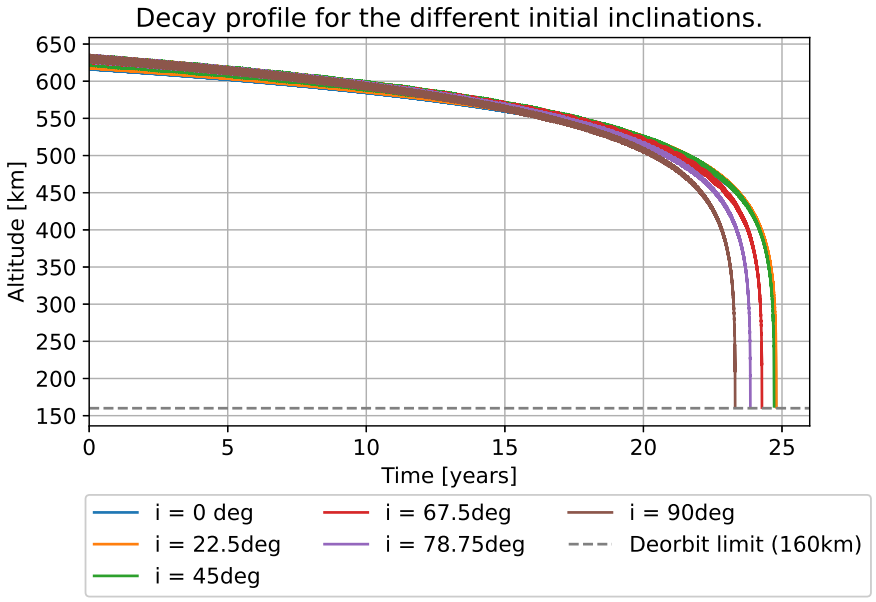

Figure 4.6: Decay profile of the base case mission for the different initial orbital inclinations.

The change in decay time due to the variation of the initial inclination is small, compared to the change of other initial orbital parameters. The difference between the longest decay time (i=22.5°) and the shortest (i=90°) is lower than 6.5%. Thus a sun-synchronous inclination (i = 97.94°), has been selected for the host spacecraft design. This inclination for common in LEO missions [62].

4.1.5. Design Case Host Spacecraft

Finally, Table 4.4 summarizes the mission parameters and geometry of the host spacecraft previously discussed.

Table 4.4: Design Case: Host Spacecraft and Mission.

Orbital Parameters	
Altitude	550 km
Eccentricity	0.0
Inclination	97.94°
Argument of Periapsis	0°
Longitude of the Ascending Node	0°
True Anomaly	0°
12U Configuration	
Average Area	0.053 m^2
Mass	36 kg

Using the parameters of the design case in Table 4.4 and including the NRLMSESI-00 atmospheric model and rarefied aerodynamic regime model in the final decay simulation, the **natural decay time of the host spacecraft is 31.39 years**; thus the sail needs to be sized to ensure a **target decay time of 6.28 years**, complying with requirement RS-01 (reduce the natural decay by a factor of 5). Figure 4.7 shows the decay profile of the host spacecraft.

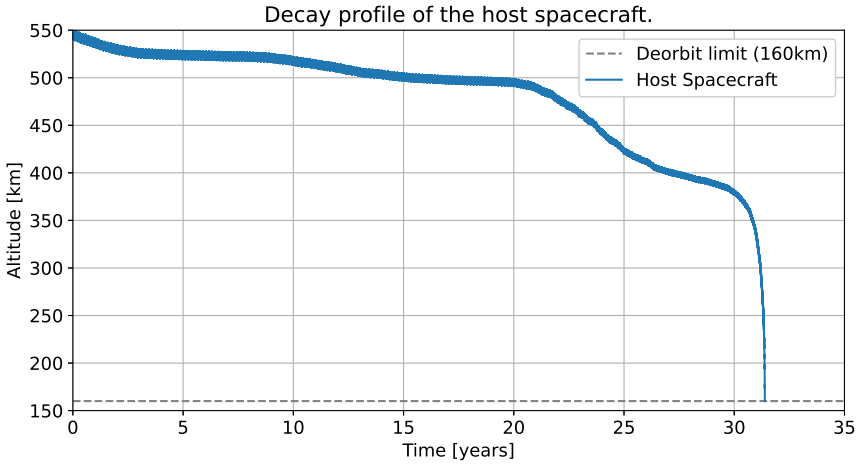

Figure 4.7: Decay profile of the host spacecraft.

This model follows the assumption that the system will disintegrate at an altitude of 160 km, based on telemetry data and decay monitoring results from similar CubeSat missions, as defined in Section 3.1. An orbital decay simulation of the host spacecraft down to 120 km altitude was also performed to ensure that, in case the system survives down to that altitude, the target decay time will not be significantly affected, as this parameter defines the sail area. The difference in the decay between an altitude of 160 km and 120 km was less than a day. Therefore the target time will be valid even down to an altitude of 120 km, without notable changes to the primary sail sizing requirement

4.2. Sail Dimensioning

Equation 1.4 shows that drag deceleration depends proportionally on surface area and inversely on mass. Further exploration of how mass and area variations impact decay time is presented in Section 4.1.2. Increasing the surface area without significantly increasing the mass will accelerate the system's decay. Drag sails are suitable for this purpose, due to their high area-to-mass ratio. To establish the design specifications for the drag sail, simulations using the same initial conditions as the host spacecraft with different area-to-mass ratios were performed. Figure 4.8 shows the results of these simulations.

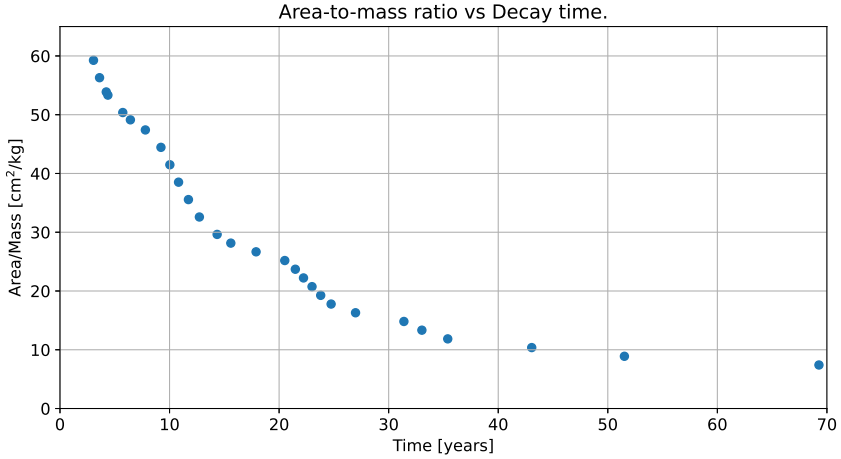

Figure 4.8: Decay time of the final host spacecraft case based on the area-to-mass ratio.

It is clear the decay time vs area-to-mass ratio relation follows an exponential trend, where higher ratios lead to lower decay periods. Figure 4.9 shows the exponential fit with a 2σ (95%) confidence level. Equation 4.2 presents the functional form of the exponential fit, including the corresponding parameter values: a,b, and c, which represent the amplitude [cm^2/kg], decay rate [years^{-1}], and offset [cm^2/kg], respectively, reported with their standard deviation.

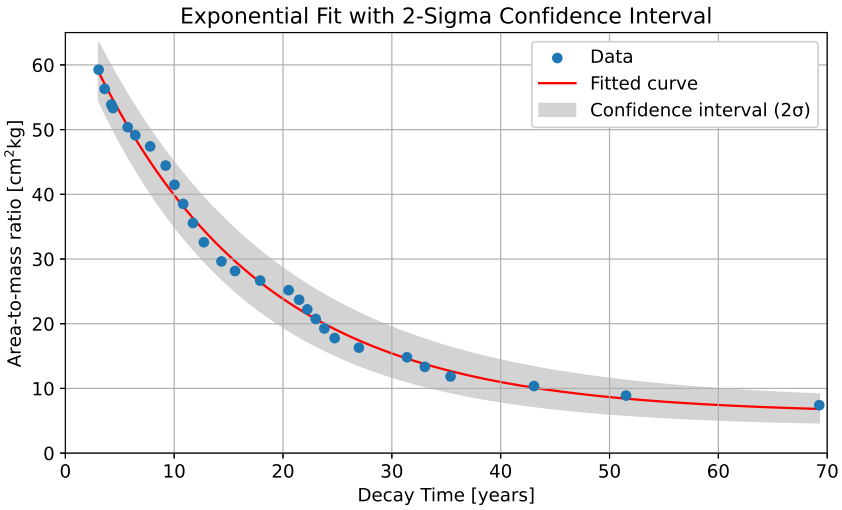

Figure 4.9: Exponential fitting of the decay time vs area-to-mass ratio relation with a $2sigma$ confidence interval.

$$\frac{Area}{Mass} = ae^{b \cdot DT} - c \tag{4.2}$$
$$a = 64.305 \pm 1.006$$
$$b = -0.064 \pm 0.003$$
$$c = 6.083 \pm 0.941$$

where DT is the required decay time in years and mass/area yields a value in cm^2/kg.

Using the fitted parameters from Equation 4.2 and incorporating a conservative 2σ confidence interval, **the area-to-mass ratio required to achieve the target decay time of 6.28 years was calculated to be 53.9 cm^2/kg**.

To validate this, a full orbital decay simulation was performed using the calculated area-to-mass ratio and the host spacecraft's initial conditions. The simulation resulted in a decay time of 4,212 years, which is 32.9% shorter than the target. This shorter decay time reflects the conservative approach of introducing the 2σ confidence interval in the fit, ensuring that the derived area-to-mas ratio provides a wide margin for the sail size and decay time.

4.2.1. Drag Sail System Mass Estimation

The area-to-mass ratio, determined by the system's mass and surface area, is defined in Equation 4.3. By estimating the system's mass based on the preliminary design described in Section 2, the required area can be calculated to ensure compliance with RC-S-01.

$$\frac{Area}{Mass} = \frac{A}{M_{HostSC} + M_{Structural} + 4M_{Boom} + M_{Sail}} \tag{4.3}$$

where M_{HostSC} is the mass of the host spacecraft, $M_{Structural}$ is the structural mass of the drag sail system defined in Equation 4.4, both fixed values in the design, M_{Boom} is the mass of the booms defined in Equation 4.5 and M_{Sail} is the mass of the sail defined in Equation 4.6, both dependent on the sail area.

$$M_{Structural} = M_{Chasis} + M_{DeployMech} + 2M_{CGG} \tag{4.4}$$

$$M_{Boom} = 2\pi R \frac{\sqrt{2A}}{2sin(\alpha)} \left(\rho_{My} t_{My} + \rho_{Al} t_{Al}\right) \tag{4.5}$$

$$M_{Sail} = A \rho_{My} t_{My} \tag{4.6}$$

where M_{Chasis} is the chassis mass, $M_{DeployMech}$ is the mass of the deploying mechanism of the booms and sail and M_{CGG} is the mass of the cold gas generators used for inflation. R is the radius of the boom, A is the surface area of the sail, α is the angle of the boom with the vertical, ρ_{My} and ρ_{Al} are the density of the Mylar and Aluminum used in the design respectively and t_{My} and t_{Al} are the thickness of those materials respectively.

Following RC-02, the system shall not be bigger than 1.5U. According to *Structures, Materials, and Mechanisms* by NASA [1], a 1.5U CubeSat standard structure has an average mass of 0.145 kg. The company estimated the deployment mechanism to be around 0.2 kg, and each cold gas generator (CGG) has a mass of 0.35 kg [26]. Two CGGs will be used in the deorbiting system as a hardware redundancy measure. The mass of the sail and the booms are based on the parameters from the preliminary design, defined in Chapter 2. Table 4.5 summarizes all known parameters.

Table 4.5: Parameters that allow the estimation of the drag sail system´s mass.

Parameter	Label	Value
Mass host spacecraft [kg]	M_{HostSC}	36
Radius of the boom [kg]	M_{Chasis}	0.145
Radius of the boom [kg]	$M_{DeployMech}$	0.2
Radius of the boom [kg]	M_{CGGs}	0.35
Radius of the boom [m]	R	0.015
Angle of the booms w.r.t the vertical [°]	α	50
Density of Mylar [kg/m^3]	ρ_{My}	1390
Density of Aluminum [kg/m^3]	ρ_{Al}	2700
Thickness of Mylar [m]	t_{My}	75E-6
Thickness of Aluminum [m]	t_{Al}	30E-6

The only unknown in equation 4.3 is the area of the sail. Solving for A, a **sail of 0.2 m^2 complies with RS-01 and the initial conditions of the problem, representing the minimum size necessary to meet the target decay time.**

4.2.2. Efficiency of the Drag Sail System

As the drag force is proportional to the area-to-mass ratio, the efficiency of the drag sail system can be determined by its ability to increase the host spacecraft's surface area while minimizing mass increase, Figure 4.10 shows this relation. In this figure, the green shaded area represents when the increase in area is greater than the increase in mass. The red dot is the baseline case of the host spacecraft, and the blue line illustrates the impact of adding the drag sail system and shows its performance over various surface area configurations.

Large sail areas might require stiffening techniques like tension cables or increased sail thickness, to prevent excessive out-of-plane deflection and maintain effective drag area. Moreover, long inflatable booms have reduced stiffness in bending, which might also require stiffening techniques, increasing the mass of the system. For this analysis, a sail area up to a surface of 1 m^2 was studied. Where no stiffening techniques are expected to be required.

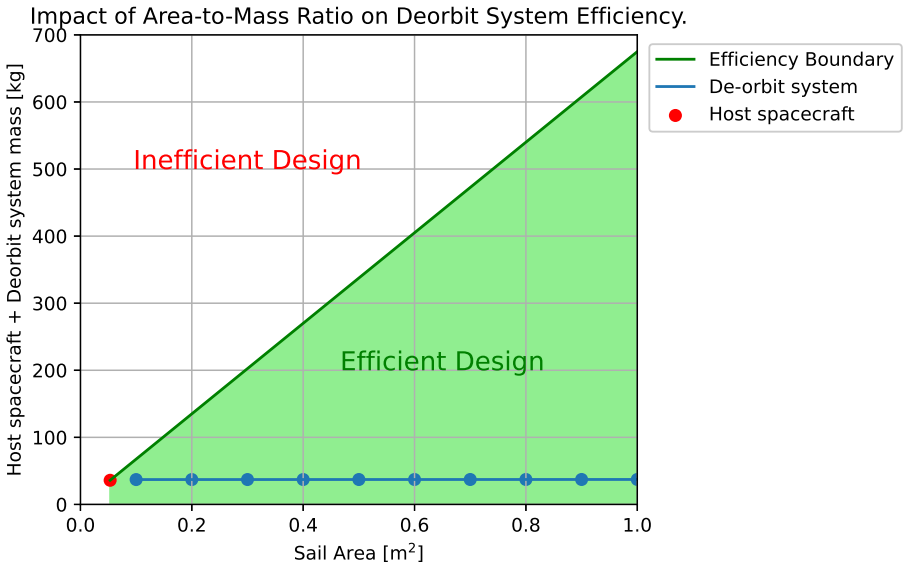

Figure 4.10: Impact of area-to-mass Ratio on deorbit system efficiency up to a sail area of 1 m^2 .

For a sail area of 1 m², the total system mass increases by less than 3.4%, making the mass increase almost negligible compared to the substantial rise in effective drag area. This suggests that, even if strengthening techniques will be needed for greater sail areas, the drag sail deorbit system with inflatable deployable booms offers a mass-efficient approach for post-mission disposal in LEO, complying with RS-10.

Figure 4.11 provides a breakdown of the mass contributions from the three primary components of the drag sail system: the structural mass, the boom mass, and the sail mass. The cumulative sum of these components represents the total system mass for varying sail areas.

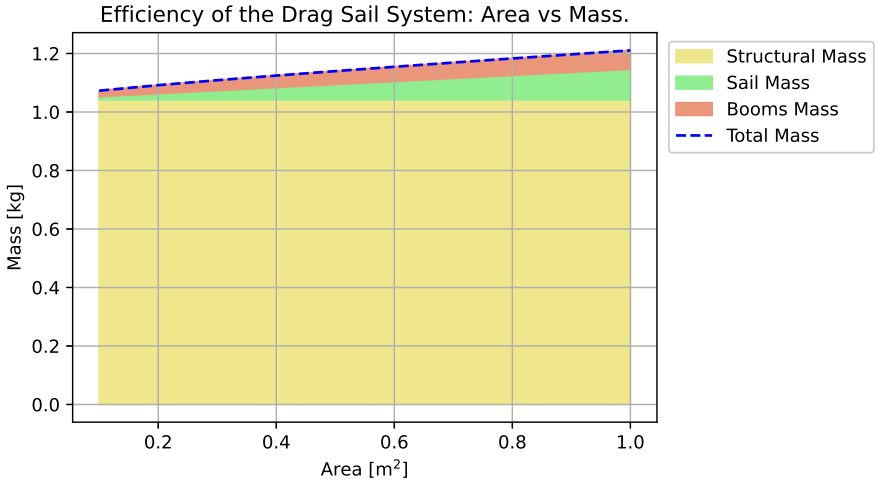

Figure 4.11: Mass breakdown of the Drag Sail System for the different sail areas.

The structural mass remains constant, as it is independent of sail size. In contrast, the boom and sail masses increase with sail area. For the boom, the mass scales with the square root of the sail area, resulting in a small increase in the overall mass. However, the sail mass increases linearly with its area, but given the minimal thickness of the sail material, its contribution to the total system mass remains relatively small. This implies that systems with larger sail areas become more efficient, as the structural mass constitutes a smaller fraction of the total mass. However, this efficiency assumes that significant stiffening of the booms and sail is not required, and the conditions under which such stiffening becomes necessary remain to be studied.

4.2.3. Analysis of high-risk factors that shorten the system´s operational life

The drag sail system is designed as a sacrificial component, primarily intended to reduce the host spacecraft's velocity at higher altitudes by increasing its drag surface area and accelerating orbital decay. Once the spacecraft reaches lower altitudes, its velocity will have decreased sufficiently so that, even if the sail fails or disintegrates, atmospheric drag alone will complete the decay process within a shorter time.

However, the drag sail is subject to several high-risk factors that could reduce its operational life. These include impacts from micrometeoroids or other debris, as well as the high thermal and structural loads during the final stages of decay.

Impact of micrometeoroids or other debris

The large surface area of the drag sail increases its risk of impact from micrometeoroids and debris. Since the sail is a fragile structural component, collisions can create punctures or tears in the fabric, reducing its effective drag area, and extending the decay time. An advantage leading from its thin film structure is that the sail won't fragment like solid components do, meaning it won't generate additional debris in the event of a collision.

An impact risk assessment would be necessary to evaluate its vulnerability to micrometeoroid and debris impact to comply with RS-12, although this aspect is outside the scope of this study.

High thermal loads at the end of the re-entry phase

As the altitude of the CubeSat is lowered, the atmospheric density increases, leading to high thermal loads due to aerodynamic heating. The drag sail was sized based on the assumption that it would withstand thermal loads without disintegrating down to an altitude of 160 km. This limit was set based on the telemetry data from the Delfi-C3 and Delfi-PQ CubeSats during decay, which transmitted down to an altitude of 200 km and 160 km respectively. And the decay monitoring for GeneSat-1 and EcAMSat CubeSats which concluded at approximately 150 km altitude.

Since the thermal loads during the decay were not analyzed in this study, and the sail is a thin structure, made out of Mylar, with a lower melting point than aluminum and a high area-to-mass ratio, absorbing and retaining heat more quickly, its disintegration is expected to be earlier than the CubeSat´s. Thus, the maximum altitude before the disintegration of the sail, that still meets the target decay requirement was calculated. Figure 4.12 shows the decay trajectory of the sail down to 160 km and the decay trajectory of the sail down to the maximum disintegration altitude that still complies with the target decay time.

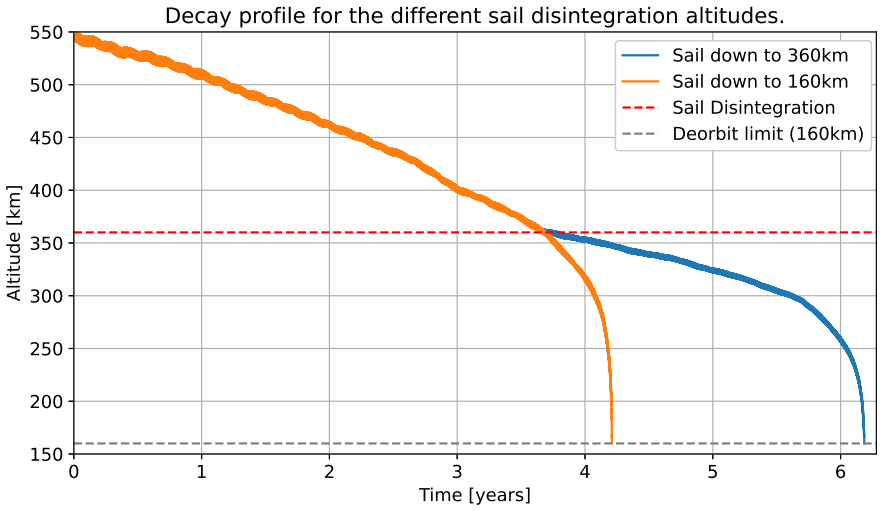

Figure 4.12: Decay profile for the highest disintegration altitude of the drag sail, which meets the target decay time.

If the sail survives down to an altitude of 360 km, the CubeSat will reach an altitude of 160 km 34 days before the target decay time, still complying with RS-01.

It is clear that once the system reaches lower altitudes, the increase in density is the main driver of the decay, therefore reducing the effective drag area during the last phase does not have such a big effect on the overall decay time. Although a detailed thermal analysis was not conducted, this result provides a broad altitude range within which sail disintegration can occur without impacting the target decay time, increasing the reliability of the design (RS-07). This range also serves as a preliminary input for future studies focused on thermal loads during decay, which will be especially critical within this altitude window.

High structural loads at the end of the re-entry phase

The higher atmospheric density at lower altitudes leads to higher atmospheric drag loads that need to be resisted by the sail and boom structures. This will be the main focus of the second part of this research. The estimation of the in-orbit mechanical loads is presented in Section 4.3.

4.3. In-orbit Loads

Two main groups of forces are in play during the deorbiting phase: the gravitational forces and the non-conservative forces (solar pressure and atmospheric drag).

If only gravitational forces had acted on the system, the satellite would have been in a free-fall state. These forces are uniformly distributed over the spacecraft not exerting stresses on the body. The non-conservative forces dissipate energy, in the case of drag this dissipation is caused due to atmospheric friction, and in the case of solar pressure, the energy is lost due to momentum transfer between the particles and the spacecraft. Thus the non-conservative loads are the primary sources of stresses on the sail and booms [69].

Figure 4.13 and Figure 4.14 show the different accelerations acting on the system for the first 5 days and last 5 days of the deorbiting phase respectively. During the initial phase, the drag force will have the lowest pull in the spacecraft due to the high altitude and an increase in its magnitude will be observed in the last phase. The solar pressure will have a constant magnitude during the decay, as an isotropic Sun source with a constant luminosity was used in the model.

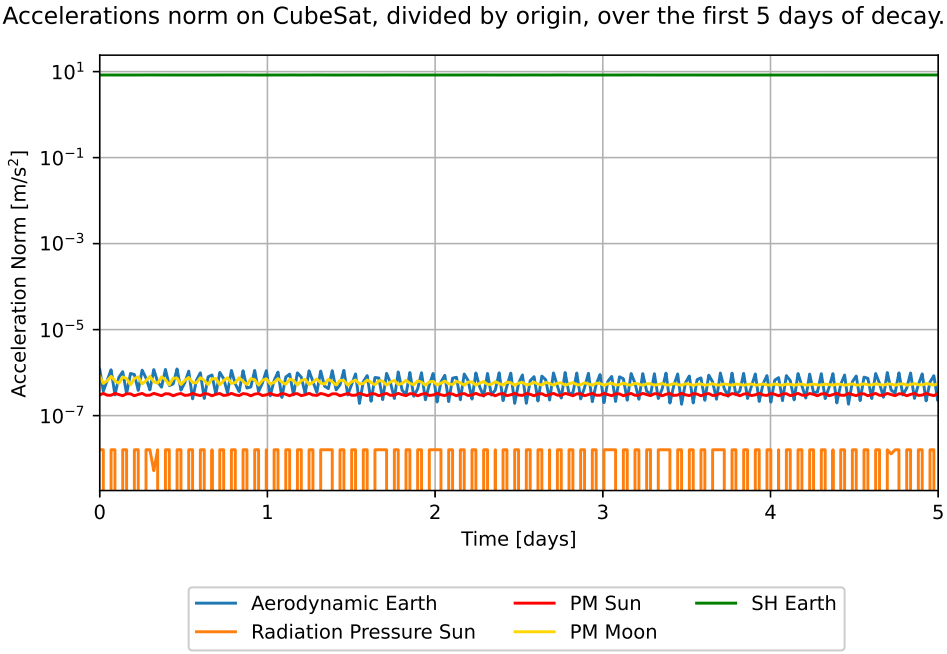

Figure 4.13: Norm of the perturbation accelerations on the CubeSat with the sail deployed for the first 5 days of decay, divided by their sources. Point Mass (PM) Spherical Harmonic (SH).

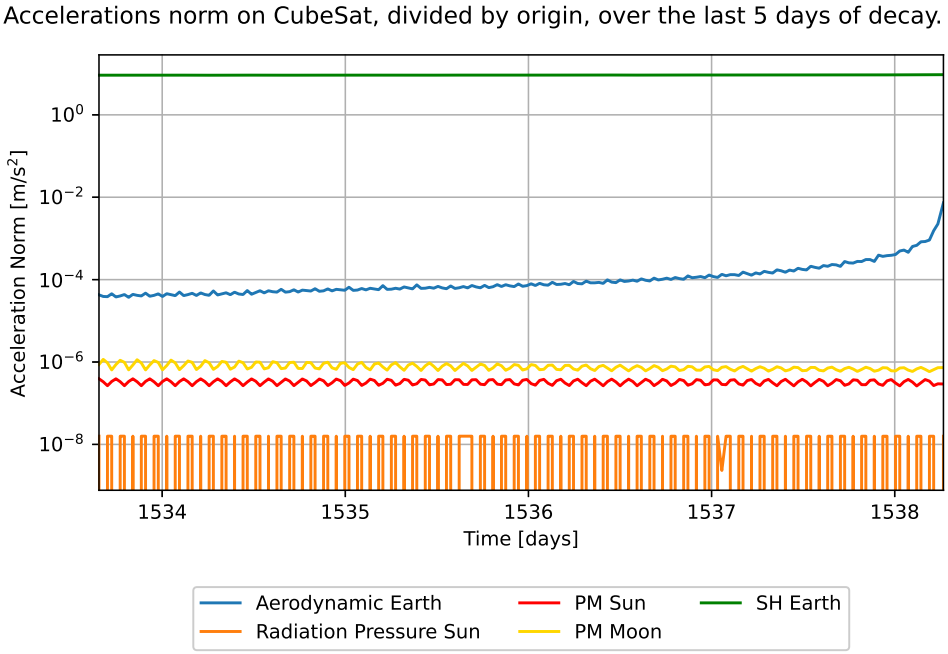

Figure 4.14: Norm of the perturbation accelerations on the CubeSat with the sail deployed for the last 5 days of decay, divided by their sources. Point Mass (PM) Spherical Harmonic (SH).

The acceleration due to solar pressure has a cyclic behavior during the orbit, being zero when the Earth is between the Sun and the satellite. Moreover, it is one order of magnitude lower than the drag acceleration and becomes negligible in comparison with the atmospheric drag when the altitude drops. Thus the drag force will be the only in-orbit load used as input for the later structural analysis.

Figure 4.15 shows the norm of the drag force over the course of propagation in the inertial frame established. With the assumption of streamflow perpendicular to the surface area of the drag sail, the change from the inertial frame to the spacecraft´s body reference frame can be done directly. The norm of the force vector in the reference frame will be equivalent to the magnitude of the force in the body frame of the spacecraft. In the body frame, the drag force vector will be perpendicular to the surface area, pointing outwards.

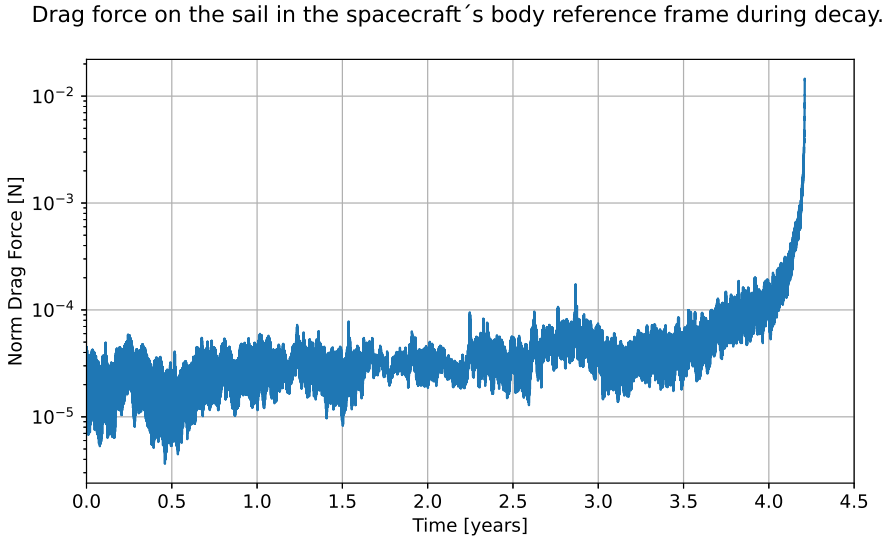

Figure 4.15: Magnitude of the drag force on the drag sail over the course of propagation.

For the structural analysis, a conservative scenario was selected in which the sail remains intact down to an altitude of 160 km. During most of the decay phase, the drag force is minimal, increasing exponentially toward the end due to rising atmospheric density. At 160 km, the drag force reaches 0.0136 N, which will serve as the input for the structural static analysis. Additionally, the drag force exhibits an oscillatory pattern, as shown in the figure, which will be used as input for a modal structural analysis.

Part II

Structural Analysis

5

System Design

This chapter introduces the two sail configurations under study, detailing their material and mechanical properties. For the booms, the chapter covers their final design stating the modifications from the preliminary design, the material properties, rigidization technique, inflation pressure cases linked to the rigidization technique, and an analytical stress analysis of the inner Mylar layer to ensure it can withstand the different inflation pressure cases. Finally, a complete sketch of the final design is presented.

5.1. Deployable Sail

In Chapter 4, it was demonstrated that a sail area of 0.2 m^2 is needed to comply with requirement RS-01. Two configurations are studied for the design of the sail. A square sail of 45 cm x 45 cm, pictured in Figure 5.1a and this same sail with 2 tension cables following the diagonals of the square, pictured in Figure 5.1b.

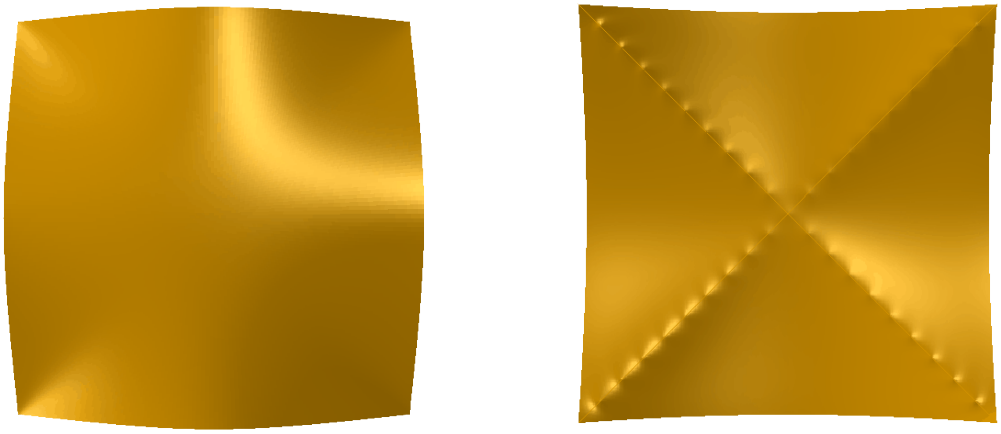

(a) Sail configuration 1.

(b) Sail configuration 2.

Figure 5.1: Sail configurations used in the design analysis.

Configuration 2 is studied as a stiffer option, to control the out-of-plane deflection of the sail. A high deflection of the sail in the out-of-plane direction causes a reduction in the effective drag sail area, decreasing the drag force, and augmenting the decay time.

The company wanted to demonstrate that the material already in stock had the mechanical properties to meet the design requirements of the sail. For the main sail, the material used is Mylar. Its mechanical properties were either sourced from the material datasheet provided by the supplier [60] or obtained from DuPont Teijin Films [12] when the datasheet did not include the necessary data. Table 5.1 contains

the mechanical properties of the Mylar needed for the following structural analysis. The variation of the properties with temperature was not found for the temperatures of study, therefore a linear interpolation based on the data from DuPont Teijin Films [12] was performed. The ultimate strength of the material increases with lower temperatures and decreases with higher temperatures. A conservative approach was used for the cold case, assuming the same value as the room temperature. The density of the Mylar is 1390 kg/m^3 with a thickness of 75 μm.

Table 5.1: Mechanical properties of Mylar for the different temperature cases studied.

Temperature	Property	Direction	Magnitude
Room (25°)	Elastic modulus [MPa]	Machine	3600
		Transverse	3900
	Ultimate strength [MPa]	Machine	186
		Transverse	215
	Yield strength [MPa]	Nominal	93
	Poisson ratio [-]	-	0.38
	Shear modulus [MPa]	-	1359
-100°	Elastic modulus [MPa]	Machine	3600
		Transverse	3900
	Ultimate strength [MPa]	Machine	186
		Transverse	215
	Yield Strength [MPa]	Nominal	172
	Poisson ratio [-]	-	0.38
	Shear modulus [MPa]	-	1359
100°	Elastic modulus [MPa]	Machine	3600
		Transverse	3900
	Ultimate strength [MPa]	Machine	140
		Transverse	161
	Yield Strength [MPa]	Nominal	34
	Poisson ratio [-]	-	0.38
	Shear modulus [MPa]	-	1359

Dyneema was selected for the tension cables. Dyneema is the commercial name for the high-performance Ultra-High-Molecular-Weight Polyethylene (UHMWPE) synthetic fiber. It has a high strength-to-weight ratio, with low elongation, ideal for reducing the out-of-plane deflection of the sail. Regarding the space environment, Dyneema has good resistance to UV radiation and temperature changes [13]. Dyneema has a density of 978 kg/m^3 and the cables have a circular cross-section area of 7.85E-07 m (radius of 0.5 mm). The tensile strength of the material is 3500 MPa and its Ultimate strength is 110 GPa [13].

5.2. Inflatable Deployable Booms

The inflatable booms consist of a two-layer cylindrical thin-walled body, two end-caps, and an inflation system, complying with RS-05.

The inflatable cylindrical body is comprised of two independent layers. The outer layer is a 30 μm thick aluminum 1100 alloy foil, with a length of 30 cm and a radius of 1.5 cm, complying with RC-03 and RC-04. The inner layer is a 75μm transparent Mylar bladder, used to improve airtightness during inflation. Both layers are attached to the end caps but are not glued to each other and therefore behave independently, contrary to the preliminary design, the reason for this design change is explained in Subsection 5.2.1. In stowed configuration, the cylindrical body is folded using a Miura origami pattern [30]. The booms are inclined at an angle of 50° relative to the vertical complying with RC-05.

Each end cap consists of 3 aluminum circular plates. The first two aluminum plates secure the Mylar bladder. An O-ring is used between these two plates to improve the airtightness of the connection. The aluminum layer is secured between the second and third aluminum plates. The 3 cm diameter end caps have a total thickness of 1 cm. This end cap design was based on the end fitting design for the inflatable mast on the project InflateSail [68]. Figure 5.2 shows the inflatable deployable boom

design. Figure 5.2a and 5.2b show the boom before and after inflation. The deformation in the inflated boom is amplified to demonstrate the inflated case. Figure 5.2c shows the aluminum (in gray) and the transparent Mylar (in light blue) layers of the boom.

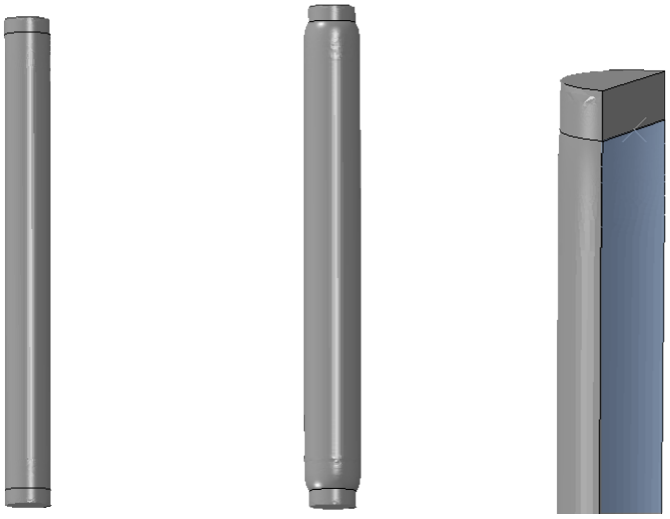

(a) Boom before inflation.

(b) Boom after inflation (deformation exaggerated).

(c) Layers of the inflatable boom.

Figure 5.2: Inflatable deployable boom design.

The inflation system consists of two MINOS CO2 Cool Gas Generators (CGG) [26] attached at the base of the deorbit system enclosure. The CGGs were designed and developed by the company HADES for space applications. A flexible hose connector attaches the CGGs to the lower end cap to allow inflation. One CGG is enough to inflate the 4 booms, as demonstrated in subsection 5.2.2, a second CGG has been introduced for system redundancy.

The material mechanical properties of the Mylar used for the inner layer of the cylindrical body are detailed in Table 5.1. The mechanical properties of the aluminum outer layer are summarized in Table 5.2. These properties were either sourced from the material datasheet provided by the supplier [59] or obtained from Matweb [40] when the datasheet did not include the necessary data. The aluminum foil alloy used for the prototype is Al-1100, with an aluminum content >99.0% and a density of 2700 kg/m^3.

Table 5.2: Mechanical properties of Al-1100 for the different temperature cases studied.

Temperature	Property	Direction
Room (25°)	Elastic modulus [GPa]	68.5
	Poisson ratio [-]	0.33
	Yield strength [MPa]	34.5
	Ultimate strength [MPa]	75
	Elongation at break [%]	0.25
-100°	Elastic modulus [GPa]	68.5
	Poisson ratio [-]	0.33
	Yield strength [MPa]	38
	Ultimate strength [MPa]	105
	Elongation at break [%]	0.4
100°	Elastic modulus [GPa]	68.5
	Poisson ratio [-]	0.33
	Yield strength [MPa]	32
	Ultimate strength [MPa]	69
	Elongation at break [%]	0.28

5.2.1. Rigidization Technique

The main drawback in the use of inflatable structures for space applications is their risk of gas leakage and therefore loss of structural capabilities [31]. A second risk in the design of inflatable deployable structures is the reduction in stiffness due to the creases created during the folding of the material for its packaging. By using the rigidization technique of work hardening, also called strain rigidization, the structure will maintain or even improve its mechanical properties after leakage, and the plastic deformation that accompanies the rigidization process will get rid of the residual creases due to folding.

Strain rigidization is a technique by which the material is subjected to a force that exceeds its yield strength, plastically deforming the material. When the load is removed, the elastic (reversible) deformation is recovered, while the plastic (permanent) deformation remains. This technique increases the strength of the material, quantified as an increase in the yield strength (σ_t or σ_y). But also makes the material more brittle, as the new yield point is closer to its ultimate strength [31].

Another risk following strain rigidization is the loss of compressive strength (σ_c), also known as the Bauschinger effect. When the material has been plastically deformed in tension, its yield strength in compression is reduced, as shown in Figure 5.3. This reduction is due to the residual stresses in the material [38].

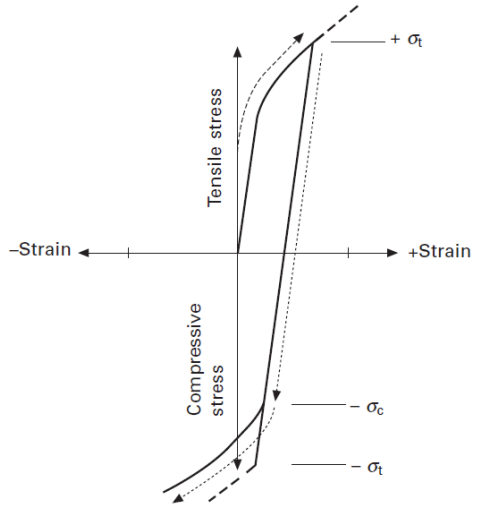

Figure 5.3: Illustration of the Bauschinger Effect when the direction of straining is reversed [38].

During the InflateSail [68] testing, some cases of auto-buckling of the boom were seen when the pressure used during the inflation was much greater than the yield pressure. This can be attributed to the design of the boom. In the construction of the boom, aluminum and Mylar were bonded together, causing the polymer's elastic recovery to induce significant residual stresses in the aluminum layer. Coupled with the reduced compressive strength and persistent creases, this led to an increased susceptibility to shell buckling.

For this design and changing the prototype definition, the inner Mylar layer and the outer aluminum layer won't be bonded, eliminating the residual stresses after deflation because of the layer adhesion, and therefore reducing the risk of buckling during deflation. This new configuration will decrease the stiffness of the boom, but as calculated in Section 4.3, the drag load in this design case is fairly small, not needing the extra stiffness the bonding provides.

5.2.2. Inflation Pressure

The boom acts as a pressure vessel subjected to internal pressure. The triaxial stress state is defined by the longitudinal stress (σ_l), the circumferential or hoop stress (σ_h), and the radial stress (σ_r). In thin-walled vessels ($R/t > 10$) the radial stress is negligible compared to the longitudinal and circumferential stresses. Because the boom R/t is equal to 500, a biaxial stress state was assumed for this analysis [42].

To calculate the pressure needed to achieve the yield of the material, the distortion energy failure theory or von Mises yield criterion has been used. This theory correlates better with experimental test observations for ductile materials than other failure theories. The theory states that yielding will be achieved when the distortion energy is equal to the uniaxial yield strength (σ_y) as described in Equation 5.1 [42].

$$\frac{1}{2}\left[(\sigma_1-\sigma_2)^2+(\sigma_2-\sigma_3)^2+(\sigma_3-\sigma_1)^2\right]=\sigma_y^2 \tag{5.1}$$

where the maximum principal stresses (σ_1, σ_2 and σ_3) can be defined as shown in Equations 5.2 - 5.4 [42].

$$\sigma_1=\sigma_h=PR/t \tag{5.2}$$

$$\sigma_2=\sigma_l=PR/2t \tag{5.3}$$

$$\sigma_3=\sigma_r=0 \tag{5.4}$$

where P is the inflation pressure, R is the radius of the vessel, and t is the thickness of the vessel wall.

Equation 5.5 defines the internal pressure that yields the material of the thin-walled vessel (Py).

$$P_y=\sqrt{4/3}\frac{\sigma_y t}{R} \tag{5.5}$$

The yield pressure calculated with Equation 5.5 is the minimum pressure that ensures the yielding of the material. To efficiently remove the creases, two other cases will be studied: 1.25 times the yield pressure and 1.5 times the yield pressure.

The harsh environmental conditions of space, mainly the extreme temperatures, have an influence on the inflation pressure. To approximate the temperature range of the mission Table 5.3, obtained from the book Low Earth Orbit Satellite Design [62], was used. This table summarizes the typical temperature ranges of common spacecraft components.

Table 5.3: Typical temperature ranges of space components [62].

Component	Typical Operating Regime [° C]
Electronics	-20 to 40
Special Electronics	0 to 35
Solar Panels	-100 to 100
Hydrazine	10 to 70

The booms will be outside the main structure, as is the case of the solar arrays, therefore a temperature range of [-100° C - 100° C] has been taken for the worst hot and cold cases. A transient temperature analysis of the satellite mission will be essential to determine the real temperature range. Further material testing is also necessary to corroborate the mechanical properties listed in Tables 5.1 - 5.2. The values taken for all parameters lay on the conservative side for this preliminary analysis.

Therefore, six different cases are studied in each structural analysis, the three inflation pressures (Py, 1.25 times Py and 1.5 times Py) for the cold (-100° C) and the hot (100° C) cases.

Effect of the inflation pressure in the Mylar layer

The thin Mylar layer needs to withstand this pressure without yielding. Two failure theories have been used for the polymeric anisotropic material, the Tsai-Hill Criteria [71] and the Maximum Strain Failure Criteria (MSS) [71]. The Tsai-Hill Criteria, described in Equation 5.6 is simpler than the Tsai-Wo criterion, as it does not distinguish between tensile and compressive stresses, but still considers the effect of combined in-plane stresses.

$$\left(\frac{\sigma_1}{X}\right)^2 - \frac{\sigma_1\sigma_2}{X^2} + \left(\frac{\sigma_2}{Y}\right)^2 + \left(\frac{\tau_{12}}{S}\right)^2 \geq 1 \tag{5.6}$$

where X, Y and S are the maximum allowable stresses and $\tau 12$ is the shear stress. For this analysis, X and Y are the yield tensile nominal strength and S is the yield shear strength.

The Maximum Strain Failure Criteria [71] states that the polymer will fail if any of its principal or shear strains exceed the corresponding maximum allowable, as described in Equation 5.7.

$$\frac{\varepsilon_1}{X/E_1} \text{ or } \frac{\varepsilon_2}{Y/E_2} \text{ or } \frac{\gamma_{12}}{S/G_{12}} \geq 1 \tag{5.7}$$

where ϵ_1 and ϵ_2 are the principal strains in the hoop and longitudinal direction respectively, and γ_{12} is the shear strain. E_1 and E_2 are Young's modulus for the 2 principal directions and G_{12} is the shear modulus.

Table 5.4 contains the different inflation pressure cases and the Tsai-Hill and Maximum Strain criteria values for the hot and cold cases. As it is seen, both theories ensure that the Mylar layer is in the elastic region. However, in the hot case at high pressure, there may be a risk of yielding as the maximum strain criterion approaches 1. A more accurate analysis using the Finite Element Method (FEM) output will be performed in Chapter 6.

Table 5.4: Inflation pressure cases for both temperature scenarios with Tsai-Hill and Maximum Strain criteria values for the inner Mylar layer.

Hot Case (100C)				
Pressure [kPa]	**Tsai-Hill**	**MSS 1**	**MSS 2**	**MSS 12**
73.90	0.18	0.43	0.21	0.21
92.38	0.29	0.54	0.27	0.27
110.85	0.41	0.64	0.32	0.32
Cold Case (-100C)				
Pressure [kPa]	**Tsai-Hill**	**MSS 1**	**MSS 2**	**MSS 12**
87.76	0.01	0.10	0.05	0.05
109.70	0.02	0.13	0.06	0.06
131.64	0.02	0.15	0.08	0.08

Cold Gas Generator Capacity

A single MINOS CO2 Cold Gas Generator [26] provides 20 Nl. At a pressure of 1 atm and a temperature of 0° C, this means the Cold Gas Generator stores 0.89 mol of CO_2. In the worst-case scenario, for a temperature of –100° C and pressure of 131.64 kPa (1.5 times P_y), the Cold Gas Generator is capable of providing 0.01 m^3 of gas. With the requirement of a 1.5 cm radius boom and accounting for the 4 booms in the design, the maximum length of the boom the CGG can inflate is 3.45 m. Thus the CGG is not a constraint for the design.

5.3. Full System

Figure 5.4 shows the representation of the fully deployed drag sail system. The booms rest on the sliding platforms, which are supported by the system´s enclosure. When inflated, guided by the crease in the system´s enclosure, the booms have a 50° angle with respect to the vertical. The projection of the booms in the drag sail plane runs along the diagonals. The sail is attached to the boom by the upper end caps.

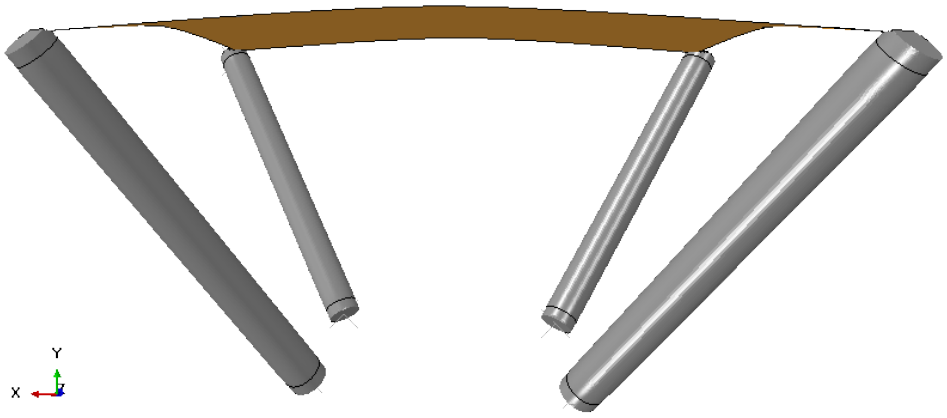

Figure 5.4: Fully deployed drag sail System. In gray the aluminum parts and in orange the Mylar sail.

6

Static Structural Analysis

This chapter defines the static structural analysis of the drag sail system. To reduce computational cost and simplify the evaluation of failure loads for the boom under compression and bending, the sail and booms were analyzed separately. For the sail, the primary focus was quantifying the deflection and stresses when the maximum drag load is applied. Since the booms serve as the main load-bearing components, a detailed rigidization, bending and axial compression analysis was conducted to confirm their resistance to the drag loads.

The static structural analysis of the drag sail system was conducted using the Finite Element Analysis (FEA) software Abaqus 19. Two extreme temperature cases hot and cold (+100° C and -100° C) were analyzed for three inflation pressures: the yield pressure, 1.25 times the yield pressure, and 1.5 times the yield pressure.

6.1. Sail

As described in Section 5.1, two sail design configurations are analyzed. Configuration 1 consists of the sail foil, and Configuration 2 includes the sail foil + 2 tension cables along the diagonals of the sail.

In the sail structural analysis, only one analysis per configuration is done. This is because the inflation pressure of the booms does not affect the performance of the sail, and, as seen in Section 5.1, the material properties of Young's modulus and Poisson ratio did not change with temperature for the sail materials, therefore, there is no need to separately analyze each temperature case, as the sail will remain in its elastic range.

6.1.1. Finite Element Model and Convergence

The sail was modeled as a 3D planar shell using the S4R element in Abaqus, which is a 4-node doubly curved element designed for shells. This element is well-suited for analyzing thin structures like the sail, as it employs reduced integration to avoid shear-locking (a numerical issue that leads to artificially high stiffness in shear-dominated deformations). The element includes hourglassing control, to prevent non-physical deformations, making it a reliable choice for thin shell models. The tension cables were modeled as 3D deformable trusses, as they work only in tension. The element used is T3D2 a 2-node linear 3D truss element. The material properties used for the sail and tension cables are defined in Section 5.1. The thin orthotropic Mylar layer of the sail was modeled as a lamina.

Due to the double symmetry of the problem, only one-quarter of the geometry is modeled, including symmetry w.r.t. X and symmetry w.r.t Y as initial boundary conditions (BC). Additionally, a pin BC is applied to the corner reproducing the sail-boom connection. This pinned BC is a conservative approximation of the real case, as the booms, even if they are stiffer than the sail, will allow some displacement. In Configuration 2, the sail and cables are connected as a surface-node tie constraint, where the sail is the master and the cable the slave.

A static general step was used, with the no-linear geometry option activated, as a notable deflection of the sail due to the drag load is expected. The drag load was introduced as a pressure load, derived from the decay analysis in Section 4.3. The maximum drag load during the decay is 0.0136 N, including a Safety Factor (SF) of 1.25 as recommended by the ESA standard ECSS-E-ST-32-10C Rev.2 [21], and dividing by the area, the pressure applied to the lower surface of the sail is 0.085 N/m^2.

A convergence analysis was conducted to ensure an accurate solution with a sufficiently refined mesh for precision, but not overly dense to avoid unnecessary computational expense. The highest stresses will be found at the pin connection, therefore the mesh will be finer in the pinned corner (size element 1), increasing along the edge, until the maximum element size is found in the middle of the sail (size element 2). Table 6.1 summarizes the results from the convergence analysis. The out-of-plane displacement (U3) in the center of the sail was used as the variable to compare. In all 3 mesh cases studied the aspect ratio of the element was smaller than 3, to reduce the risk of shear locking and improve the accuracy of the results.

Table 6.1: Drag sail FE model convergence study.

Size element 1	Size element 2	U3 [m]	Relative Error [%]
0.005	0.005	0.00204	-5.2
0.005	0.0025	0.00212	-1.8
0.005	0.00125	0.00216	-

The convergence criterion used was that the error with respect to the finest mesh model should be lower than 5%. The mesh with a maximum element size of 0.005 and minimum element size of 0.0025 complies with the convergence criterion, summing up to 3969 quad elements with an average aspect ratio of 1.13 and a worst aspect ratio of 1.39. Figure 6.1 shows the converged mesh. Each cable can be modeled using a single element, as they act as trusses under tension with constant geometric and mechanical properties. However, to model their connection to the sail, 10 elements were used.

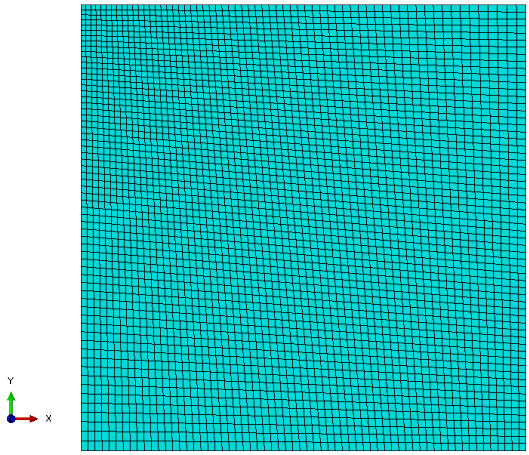

Figure 6.1: Sail converged mesh.

6.1.2. Deflection

A big out-of-plane deflection of the sail can cause a decrease in the effective drag area, increasing the decay time of the CubeSat. The maximum deflection of the sail for Configuration 1 is 2.12 mm at the sail´s center. The maximum deflection of the sail for configuration 2 is 0.95 mm at the middle point of its outer edges. Figure 6.2 shows the out-of-plane deflection of the sail for both sail configurations. The in-plane displacements have not been analyzed as they are in the order of 1E-3 mm and 1E-4 mm for Configurations 1 and 2 respectively.

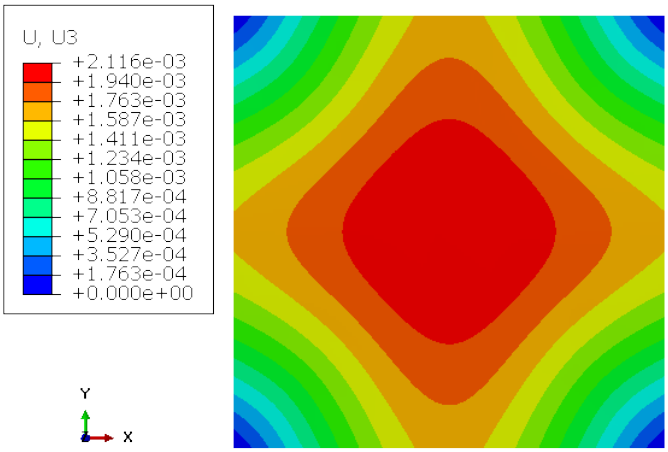

(a) Sail configuration 1.

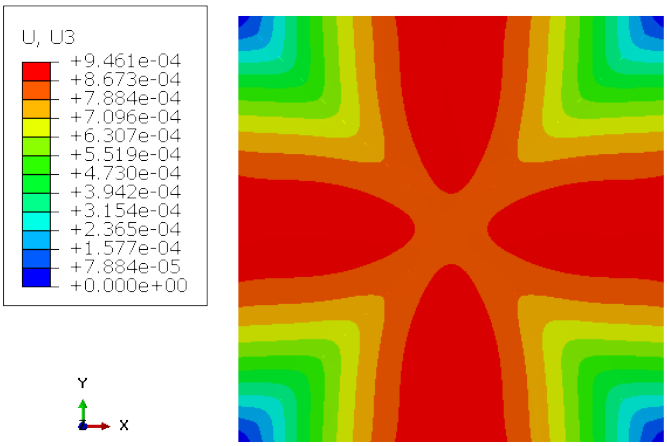

(b) Sail configuration 2.

Figure 6.2: Out-of-plane displacement of the sail when drag load is applied. Displacement in m.

As can be seen, the out-of-plane displacements of both configurations are small enough that they won't affect the effective drag sail area. A lower deflection of the sail is obtained with the second configuration. This is because the loads are distributed across wires, reducing the load carried by the fabric of the sail. Additionally, the tension cables divide the area into four triangles, an inherently more rigid shape, that resists deformation more effectively.

6.1.3. Stress Analysis

The maximum stress (MS) and the Tsai-Hill criteria were used to assess if the Mylar sail reached its yield point. The maximum stress of the cable in tension was compared with its UTS to determine if it would withstand the drag load. Table 6.2 summarizes the values of these criteria for the two sail configuration cases. The maximum in-plane stresses at the mid-plane were used for this analysis.

All criteria values are significantly lower than 1, therefore it's safe to say that the sail will not fail under the drag pressure in any of the configurations. Figure 6.3 shows the in-plane stress distribution across the mid-plane of the sail for Configuration 1. The applied pressure load propagates from the sail's center toward the pinned boundaries along the diagonals, creating a radial stress flow pattern that becomes especially pronounced near the corners (as shown in Figure 6.3b). The lowest stresses are found at the midpoints of the sail's outer edges. These edge midpoints, lacking constraints, allow for greater deformation, which results in reduced stress concentrations.

In Configuration 2, the inclusion of tension cables along the diagonals reduces the overall magnitude

of in-plane stresses within the sail, as the cables now carry a portion of the drag load. These cables redirect the load toward the corners, resulting in higher in-plane stress toward the outer edges of the sail while maintaining minimal stresses in the central region (as seen in Figure 6.4b). At the points where the cables are attached to the sail, the high stiffness of the cables restricts the in-plane deformation of the sail, creating pronounced stress concentrations in these attachments along the diagonals.

Table 6.2: Maximum stress and yield criteria for the two sail configurations.

	Conf 1: Sail	Conf 2: Sail	Conf 2: Cables
Max stress X [MPa]	1.62	0.13	0.95
Max stress Y [MPa]	1.64	0.15	-
Max shear stress XY [MPa]	1.05	0.09	-
Yield strength [MPa]	34.5		-
Yield shear strength [MPa]	17.2		-
Ultimate strength [MPa]	-		3500
MS$_X$	0.047	0.004	2.7E-4
MS$_Y$	0.048	0.004	-
MS$_{XY}$	0.030	0.003	-
Tsai-Hill	0.006	4.31E-5	-

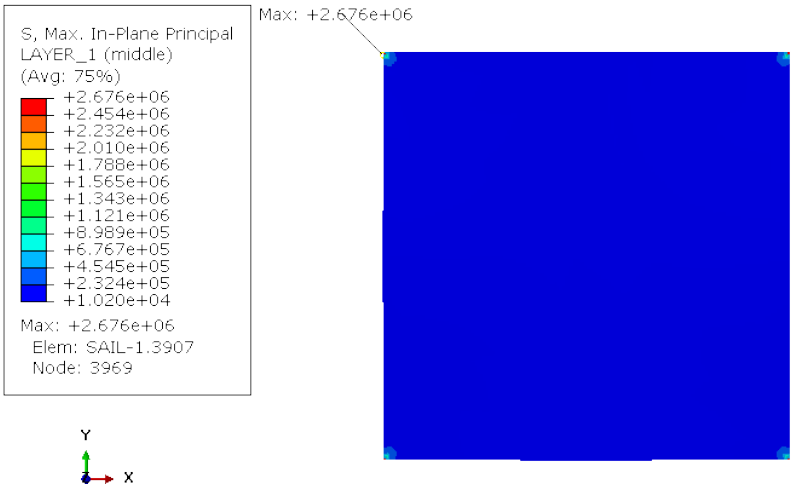

(a) Stress distribution.

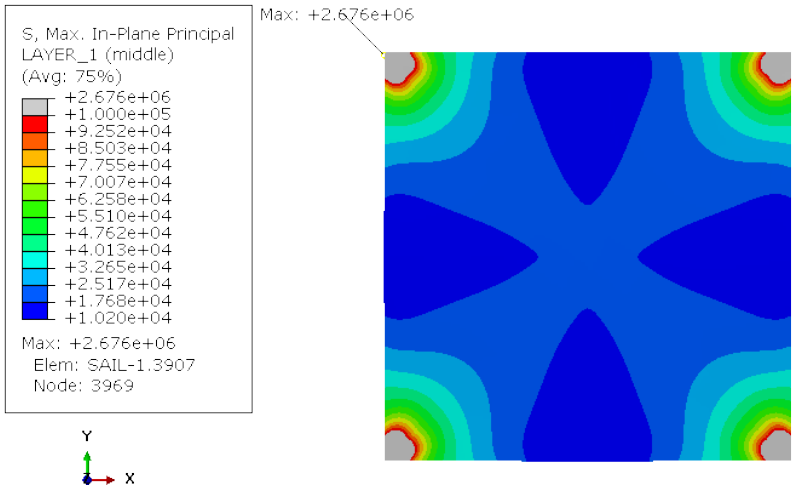

(b) Stress distribution with a maximum at 0.1 MPa.

Figure 6.3: In-plane stress distribution on the mid-plane for Configuration 1. Stresses in Pa.

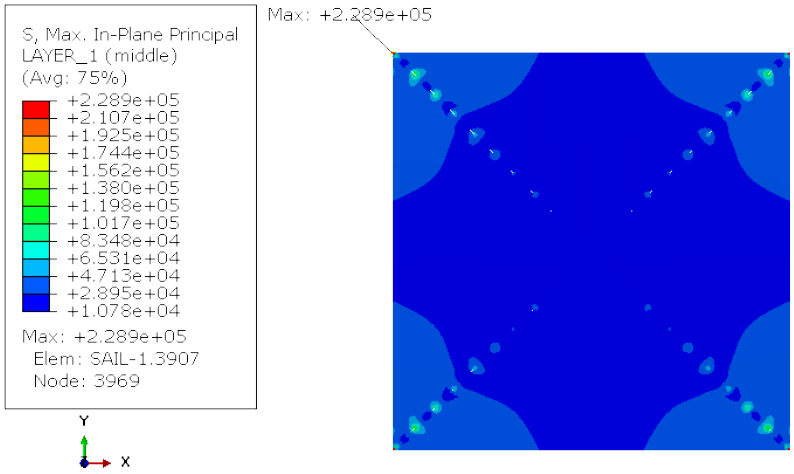

(a) Stress distribution.

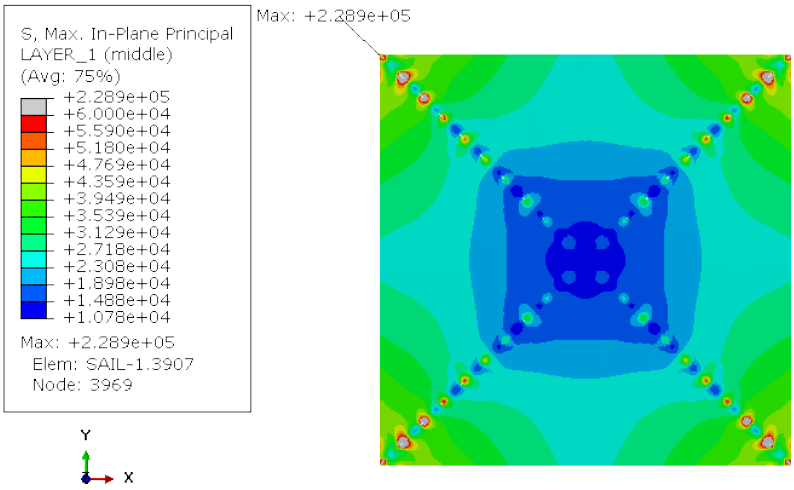

(b) Stress distribution with a maximum at 0.06 MPa.

Figure 6.4: In-plane stress distribution on the mid-plane for Configuration 2. Stresses in Pa.

6.1.4. Reaction Forces

The booms are connected to the sail's corners and extend toward the system's center along the sail's diagonals, forming a 50° angle with the vertical. To transform the reaction forces from the sail's local coordinate system to the boom's local coordinate system, a coordinate rotation is required. This transformation is achieved by rotating 45° about axis 3, to align axis 1 with the diagonal. A rotation of -50° about axis 2 is necessary to align axis 3 with the boom, as shown in Figure 6.5.

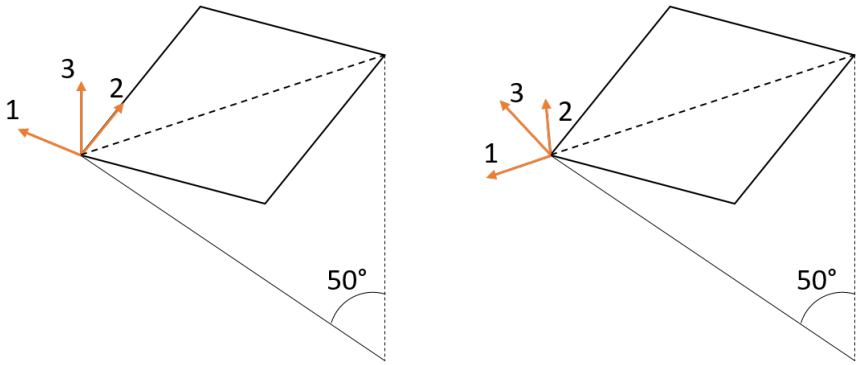

Figure 6.5: Rotation from sail local coordinate system to boom local coordinate system.

Equations 6.1 -6.2 define the rotation from the sail's local coordinate system to the boom's local coordinate system.

$$\bar{F}_{boom} = R_2(-50)R_3(45)\bar{F}_{sail} \tag{6.1}$$

$$\bar{F}_{boom} = \begin{bmatrix} \cos(-50) & 0 & \sin(-50) \\ 0 & 1 & 0 \\ -\sin(-50) & 0 & \cos(-50) \end{bmatrix} \begin{bmatrix} \cos(45) & -\sin(45) & 0 \\ \sin(45) & \cos(45) & 0 \\ 0 & 0 & 1 \end{bmatrix} \bar{F}_{sail} \tag{6.2}$$

$$F_{boom,Va} = -F_{boom,3} \tag{6.3}$$

$$F_{boom,Ha} = -\sqrt{F_{boom,1}^2 + F_{boom,2}^2} \tag{6.4}$$

where $\bar{F}_{sail}$ is the reaction force in the sail's local coordinate system at the pin BC, $\bar{F}_{boom}$ is the reaction force in the sail expressed in the boom's local coordinate system, and $\bar{F}_{boom,a}$ is the applied force on the boom, which has the same magnitude but opposite sign of the reaction force of the sail in the boom's coordinate system. Due to the XY symmetry plane of the boom, the horizontal applied force is the norm of the X and Y components in $\bar{F}_{boom,a}$, while the vertical applied force is the Z component in $\bar{F}_{boom,a}$.

The reaction forces in the sail were calculated with two different FE models. The first one used only the sail and simulated the boom-sail connections with pin BC. The second used the full system model, which will yield lower reaction forces, as the booms allow some displacement in the free end, where the sail-boom connection is. A more detailed definition of the full system FE model can be found in Chapter 8.

These reaction forces in the sail´s coordinate system ($\bar{F}_{sail}$), in the boom´s coordinate system ($\bar{F}_{boom}$), and the applied forces in the boom in its local coordinate system ($\bar{F}_{boom,a}$) are summarized in Table 6.3.

Table 6.3: Reaction forces in the sail and applied forces in the boom.

	Configuration 1		**Configuration 2**	
	Only Sail	**Full System**	**Only Sail**	**Full System**
$\bar{F}_{sail}$ [N]	(0.26,-0.26,-0.005)	(0.12,-0.12,-0.005)	(0.59,-0.59,0.005)	(0.13,-0.13,-0.006)
$\bar{F}_{boom}$ [N]	(0.23,0,0.28)	(0.11,0,0.13)	(0.58,0,0.63)	(0.12,0,0.14)
$\bar{F}_{boom,a}$ [N]	H=-0.24, V=-0.28	H=-0.11,V=-0.13	H =-0.54, V=-0.63	H =-0.12, V=-0.14

The sail exerts an in-plane force that may cause failure in bending and a compressive force that could lead to buckling. The direction of the vertical force appears counterintuitive, as the sail's pressure is directed outward. Appendix B provides a detailed explanation of this effect. As expected, in the FE model where only the sail was simulated, higher reaction forces were observed. This effect was most pronounced in Configuration 2. To ensure a conservative estimate of the loads, the results from the sail model will be used to calculate the Margins of Safety (MoS) for bending and compression in Section 6.2.4.

6.2. Inflatable Deployable Booms

As defined in Section 5.2, the booms are composed of two independent thin layers, an outer aluminum layer, and an inner Mylar layer. It was assumed that the elastic deformation of the Mylar inner bladder would not impact the aluminum layer during the inflation and deflation of the structure, as the Mylar´s Young´s modulus is one order of magnitude lower than the Aluminum. Consequently, the two layers were modeled separately. Another assumption taken in the model is that the creases due to the folding of the boom for its stowed configuration will fully disappear when plastically deforming the boom during its rigidization.

6.2.1. Finite Element Model and Convergence

The end caps were modeled as three-dimensional (3D) rigid bodies. The foil layers, similar to the sail, were modeled as 3D deformable shells using S4R elements. The boom geometry was modeled at its unfolded stage without the remaining creases due to folding (a perfect cylinder). The Material properties of Mylar and aluminum are provided in Tables 5.1 and 5.2, they were modeled as isotropic and lamina respectively. The aluminum layer is expected to undergo plastic deformation, so true plastic stress-strain data was incorporated into its material definition based on the Abaqus guide guidelines [10]. Kinematic hardening was applied to the aluminum to account for strain-induced hardening effects. The attachment between the boom and end caps was simulated as a tie constraint between the shell and rigid body. In practice, the foil would be clamped between two aluminum plates, with an O-ring to enhance grip and ensure airtight sealing. Therefore, the tie constraint mimics the aluminum's secure hold on the cap.

The booms were modeled as cantilever beams, fixed at the base (encastre boundary condition) and free at the top, where forces were applied. A static general step was employed to simulate inflation and deflation with a maximum iteration increment of 0.001 to help achieve convergence. In both inflation and deflation steps, non-linear geometry was activated to account for plastic deformation, the primary mechanism contributing to boom rigidization. The internal pressure was modeled as a pressure load to the foil and inner surfaces of the caps.

For subsequent loading steps involving tension and bending, a Dynamic Implicit Quasi-static step was applied, utilizing the Riks (arc-length) solver. This approach uses the material's damping to maintain steady control during the simulation. The maximum increment in the step was 0.01, the same as the initial increment, to ensure convergence and stability of the analysis.

In the bending analysis, the load was applied as a horizontal concentrated force of 3.5 N, and in compression as a vertical shell edge load of 2500 N/m, equivalent to 235 N concentrated force applied downwards. These values were approximated from the non-rigidized case, the first analysis in both failure studies.

The element size for the caps was relatively large, as they were modeled as rigid bodies. However, due to the tie connection between the cap and the shell cylinder, the cap´s edge in the boom-cap connection was meshed with the same element size as the end edges of the cylinder, to ensure effective coupling. The meshing of the caps can be seen in Figure 6.6. For the shell cylinders, due to the high stresses expected at the connection with the end caps, a smaller element size (size element 1) was used near the ends of the boom, while a coarser mess (size element 2) was used toward the center. The 2.5 cm before both ends of the boom were divided into 5 equal-hight areas to have better control in the deformation of the element during meshing. Figure 6.7a shows this partition. The element size ratio was always smaller than 3.

Table 6.4 summarizes the convergence study, using the vertical displacement (U2) of the top nodes of the cylinder after deflation as the variable to judge convergence.

Table 6.4: Cylindrical shell boom FE mode convergence study.

Size element 1	Size element 2	U2 [m]	Relative Error [%]
0.0015	0.0015	1.06351E-06	-107.6
0.0015	0.0009	-8.56652E-06	-38.83-1.8
0.0015	0.00045	-1.28191E-05	-8.46
0.0015	0.0002	-1.36906E-05	-2.24
0.0015	0.0001	-1.40044E-05	-

An error in the U2 lower than 5% w.r.t. the finest mesh model was the convergence criterion used. The mesh with a maximum element size of 0.0015 and minimum element size of 0.0002 complies with the convergence criterion, summing up to 30337 quad elements with an average aspect ratio of 1.22 and a worst aspect ratio of 2.41 and 270 tri elements with an average aspect ratio of 1.28 and worst aspect ratio of 1.98 in the cylinder. 28652 tetrahedral elements were used in the cap. Figures 6.7b and 6.6 show the mesh distribution of both parts respectively.

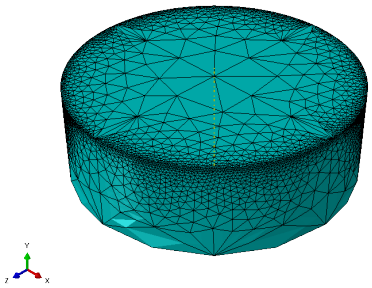

Figure 6.6: Mesh of the bottom end cap. Higher mesh density at the top edge, connecting edge with the shell cylinder.

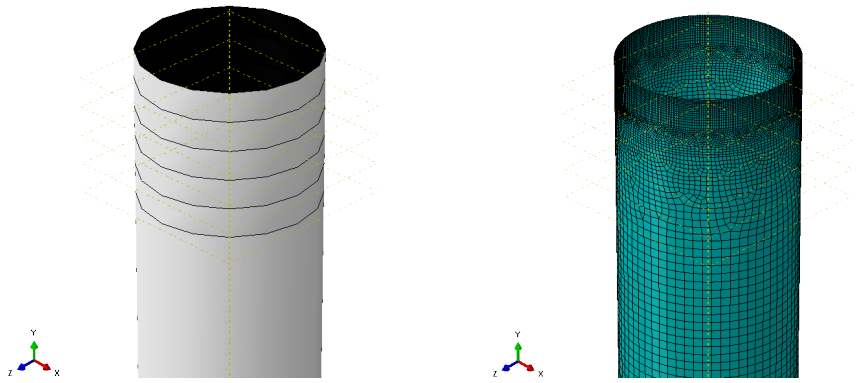

(a) Partition of the boom´s surface for meshing. **(b)** Boom converged mesh.

Figure 6.7: Boom partition and meshing.

6.2.2. Rigidization of the Boom

The rigidization of the boom occurs in two key phases: inflation and deflation. During inflation, the boom is pressurized to a level where the aluminum layer exceeds its yield strength, resulting in plastic deformation, while the inner Mylar layer remains within its elastic range. This differential behavior between materials allows the aluminum to undergo permanent deformation without compromising the structural integrity of the Mylar. During deflation, gas slowly leaks out from the boom, causing internal pressure to drop. As a result, the internal stresses in the aluminum and Mylar disappear while the residual plastic strain remains, thereby rigidizing the boom even in the absence of internal pressure.

To achieve rigidization, during inflation, the minimum stress in the boom should be larger than the yield strength of the aluminum, but lower than the ultimate strength, so the material doesn't fail.

Based on basic shell theory under ideal conditions (no imperfections, uniform material properties, and perfect cylindrical shape) the membrane stress is uniform across the thickness. This was seen in the middle sections of the boom, where these ideal conditions were met. Close to the end caps, where the tie connection is, there is a necking of the boom. This phenomenon is clearly seen in Figure 6.9b. This necking introduces additional bending stresses through the thickness, therefore the inner surface experiences higher stress because it's the "compressed" side, and the outer surface experiences lower stress because it's the "tensioned" side in bending. For that reason, the inner plane where the highest stresses are found, was used to check for final failure and the the outer plane where the lowest stresses are found, was used to check for rigidization (yielding). Table 6.5 summarizes these values.

Table 6.5: Stress analysis on the aluminum layer of the inflatable boom.

	Hot Case			Cold Case		
	76 kPa	**92 kPa**	**110 kPa**	**90 kPa**	**110 kPa**	**132 kPa**
Min stress during inflation [MPa]	15.20	32.12	32.37	16.36	38.13	38.50
Max stress during inflation [MPa]	33.34	43.53	58.34	39.41	51.15	66.85
Max stress after deflation [MPa]	15.03	24.51	20.99	13.14	28.93	24.63

Figure 6.8 illustrates the stress distribution in the aluminum boom following the inflation and deflation phases for the hot case at an inflation pressure of 76 kPa. While the majority of the boom is uniformly rigidized, a small region near the end cap connection remains less so. Figures 6.9a and 6.10a show a close-up look at this region.

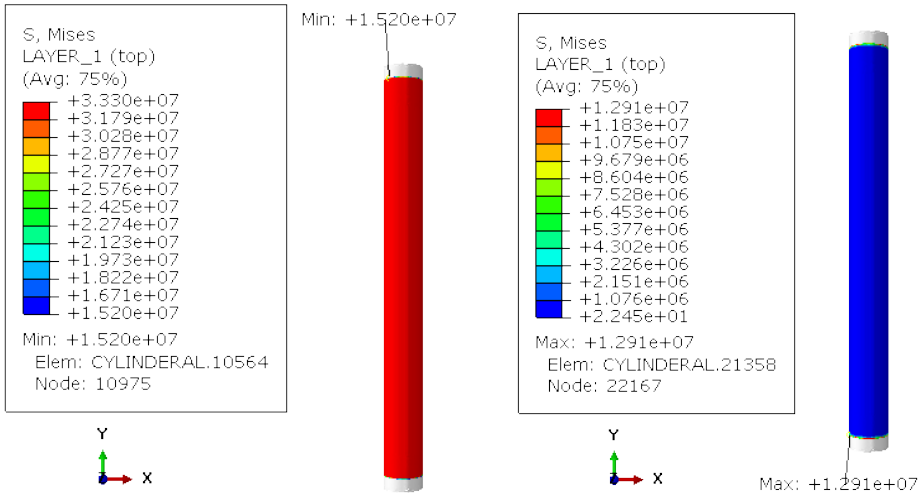

(a) Inflation. **(b)** Deflation.

Figure 6.8: Stress distribution after Inflation and Deflation for the hot case 76 kPa inflation pressure. Stresses in Pa.

As rigid end caps attach the aluminum layer at each end, the areas at the boom-end cap connections will not experience the same rigidization as the rest of the boom. The aluminum layer deforms plastically in the middle area of the boom, where is free to expand. However, at the rigid end caps, the material is constrained and cannot expand in the same way. For the lower inflation pressure of both temperature cases, the stresses in this region don't reach the yield strength. This can be seen in Table 6.5 and Figure 6.9a. This causes the regions near the end caps to remain unrigidized (elastic), creating a transition zone between the rigidized central section of the boom and the elastic regions near the end caps. At higher inflation pressures, plastic deformation does occur near the end caps, although to a lesser extent than in the boom's central area, leading to non-uniform rigidization, where the stress gradient along the boom can also be seen. This is shown in Table 6.5 and Figure 6.9b.

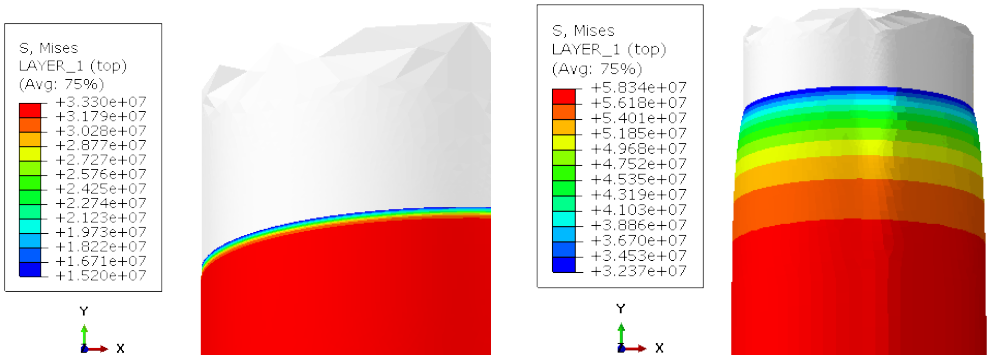

(a) 76 kPa inflation pressure. **(b)** 110 kPa inflation pressure.

Figure 6.9: Close-up look at the cap-boom connection during inflation for the different inflation pressure cases. Stresses in Pa.

After deflation, when the internal pressure is released, the central part of the boom, where the plastic deformation took place, keeps its shape without significant residual stresses as seen in Figure 6.8b. Whereas the area close to the end cap has to withstand the difference between the strained middle section and the fixed end caps, resulting in high residual stresses, as seen in Figure 6.10.

In Figure 6.10a, a lower stress concentration is found in the area immediately adjacent to the end cap compared to the stress found at the region just beyond it. This is because, for an inflation pressure of 76 kPa the area immediately adjacent to the end cap connection did not experience plastic straining, remaining in its elastic range. At an inflation pressure of 110 kPa, however, this region immediately adjacent to the end cap undergoes plastic straining, resulting in the highest stress concentrations appearing there, as shown in Figure 6.10b.

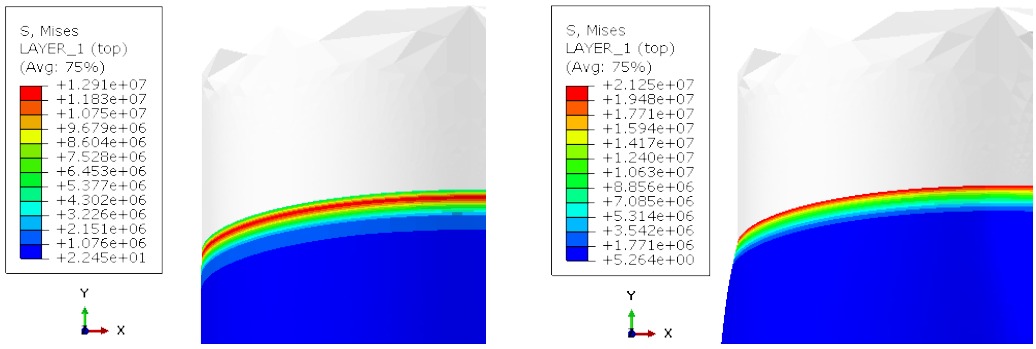

(a) 76 kPa inflation pressure. **(b)** 110 kPa inflation pressure.

Figure 6.10: Close-up look at the cap-boom connection after deflation for the different inflation pressure cases. Stresses in Pa.

The bending flexibility at the boom-end cap connections does not pose an issue for our design, as strict dimensional stability is not required and the majority of the boom remains rigidized. However, these connection areas represent potential points of failure under bending loads.

Rigidization of the middle section of the boom.
Figure 6.11 shows the strain-stress curve in the hoop direction, where the hoop stress (S1) and the hoop strain (LE1) are plotted. Figure 6.12 shows the strain-stress curve in the longitudinal direction, where the longitudinal stress (S2) and the longitudinal strain (LE2) are plotted. The strain and stress values were taken from an element in the middle of the boom for the different inflation pressures in the hot case. The same analysis was done for the cold case, following the same tendency as the hot case.

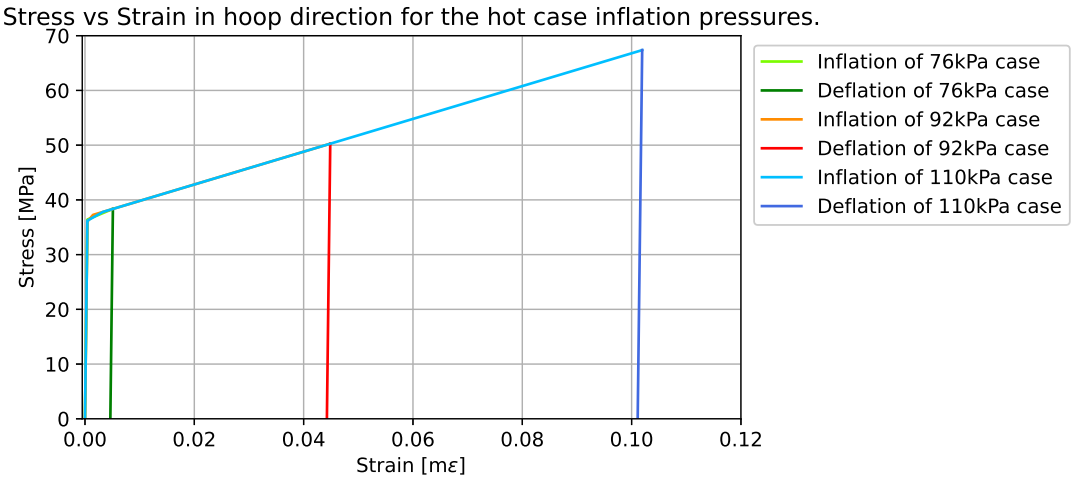

Figure 6.11: Rigidization in the hoop direction. Stress vs. strain graph.

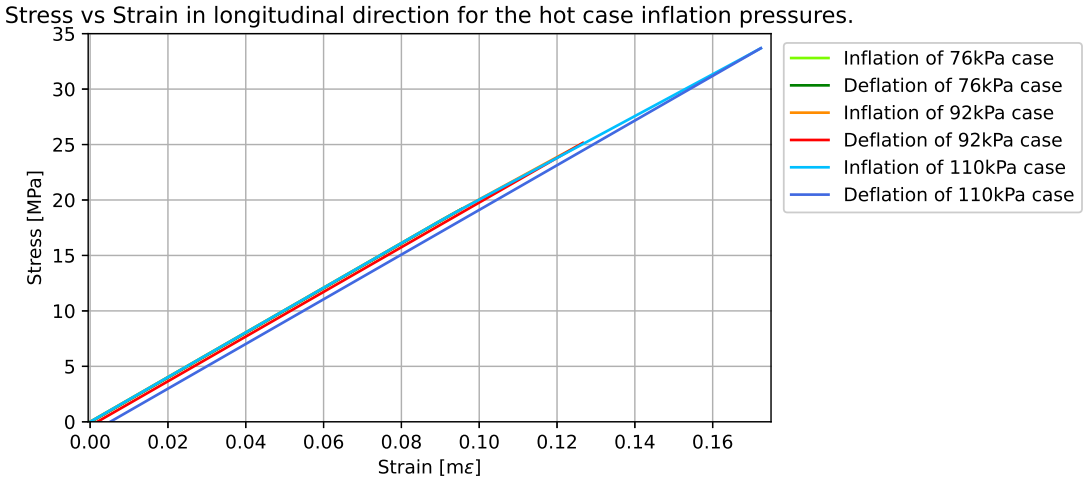

Figure 6.12: Rigidization in the longitudinal direction. Stress vs. strain graph.

The boom deforms substantially more radially, due to the hoop stress being twice the longitudinal stress for a cylindrical vessel, as shown in Equation 5.3. This can also be seen in the strain values after deflation for both directions, where the biggest strain for the longitudinal direction (maximum inflation pressure) is $5\mu\varepsilon$, whereas the minimum strain in the hoop direction (minimum inflation pressure) is 0.0046. Only rigidization in the hoop direction is perceptible, pushing up the yield strength of the material in that direction. As was explained before, this level of rigidization occurs only in the middle section of the boom, where it is free to expand.

The primary working principle of the strain rigidization technique is demonstrated in these graphs: higher levels of rigidization, indicated by an increase in yield strength, are achieved with higher inflation pressures (greater plastic deformation during inflation).

Rigidization near the end cap connection.

Near the end caps, the rigidization process exhibits distinct characteristics. Figure 6.13 illustrates the relationship between internal pressure and von Mises stress at an element located at the boom-cap connection for the 3 inflation pressures in the hot case. Contrary to expectations, the highest inflation pressure does not correspond to the highest residual stresses after deflation. Initially, it was hypothesized that greater inflation pressure would yield higher residual stresses due to the increased strain in the middle of the boom.

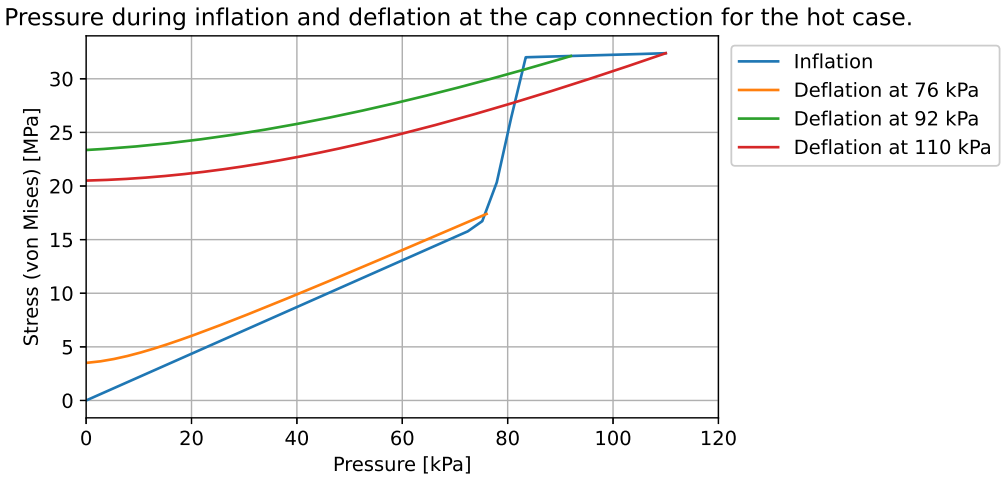

Figure 6.13: Internal pressure vs Stress at the region near the end cap for the different hot case inflation pressures.

This unexpected behavior may result from a complex nonlinear response associated with the tie constraint or from potential solver inaccuracies and numerical instabilities within Abaqus, testing will be necessary to corroborate these results.

If the real scenario is presented in the results, the inflation process reveals three main regions: an elastic region, where stress increases proportionally with pressure; a transition region, characterized by a steeper stress increase with minimal pressure change; and a plastic region, where further pressure increases result in smaller stress increments. The transition region suggests a hardening phase, in which the material begins to deform plastically but has not yet reached a fully stabilized state. This nonlinear behavior may account for the observed outcome, where an inflation pressure of 97 kPa results in higher residual stresses than an inflation pressure of 110 kPa after deflation.

Homogeneous Rigidization of the Aluminum Layer

To ensure the rigidization is homogeneous through the thickness, the change in strain over the thickness for the point of maximum and minimum stresses after deflation was analyzed. Tables 6.6 and 6.7 summarize these values. The strain values for the lowest inflation pressures were not analyzed, as they remain in their elastic region during inflation.

Table 6.6: Plastic strain variation along the thickness of the aluminum after deflation at the points of highest (Max LE) and lowest (Min LE) strain for the hot case.

	Hot Case					
	76 kPa		**92 kPa**		**110 kPa**	
	Max LE	Min LE	Max LE	Min LE	Max LE	Min LE
LE top plane [$m\varepsilon$]	5.073	-	44.255	0.076	101.110	1.533
LE bottom plane [$m\varepsilon$]	5.040	-	44.255	0.077	101.110	1.589
Difference [%]	0.65	-	0.00	1.73	0.00	3.52

Table 6.7: Plastic strain variation along the thickness of the aluminum after deflation at the points of highest (Max LE) and lowest (Min LE)strain for the cold case.

	Cold Case					
	90 kPa		**110 kPa**		**132 kPa**	
	Max LE	Min LE	Max LE	Min LE	Max LE	Min LE
LE top plane [$m\varepsilon$]	3.687	-	35.486	0.668	77.930	1.303
LE bottom plane [$m\varepsilon$]	3.658	-	35.486	0.678	77.930	1.343
Difference [%]	0.79	-	0.00	1.53	0.00	2.98

The maximum differences in strain along the thickness are found at the lowest strain points. These points are at the end cap-boom connection, where the aluminum is not free to deform and rigidizes differently from the rest of the boom. The maximum difference at this point is 3.52%, this can still be considered a small difference ensuring homogeneous rigidization along the thickness. The maximum strain points are found farther from the boom-cap connection. These points see a very small or zero difference in strain along the thickness as they are not constrained, following the basic shell theory under ideal conditions, which demonstrates a homogeneous rigidization along the thickness.

Elastic deformation of the Mylar layer.

The Mylar layer acts only as a bladder to ensure better airtightness during inflation, not being a load-supporting member. Therefore the only concern in its structural design is that it does not overpass its yield strength, so the polymer remains in its elastic range, ensuring proper performance. The Maximum Stress (MS) and Tsai-hill failure criteria were used to assess the Mylar layer performance. Table 6.8 shows both criteria reveal no yielding of the polymer for all the temperature and inflation pressure cases, as derived from the analytical analysis in Section 5.2.2.

Table 6.8: Maximum stresses in the hoop (1), longitudinal (2), and shear (12) directions, along with the yield criteria evaluation for the boom´s Mylar layer during inflation

	Hot Case			Cold Case		
	76 kPa	**92 kPa**	**110 kPa**	**90 kPa**	**110 kPa**	**132 kPa**
Max stress 1 [MPa]	16.25	19.59	23.34	19.17	23.34	27.92
Max stress 2 [MPa]	12.75	15.06	17.56	14.78	17.56	21.84
Max shear stress 12 [MPa]	2.12	2.58	3.10	2.52	3.10	3.74
MS1	0.47	0.57	0.68	0.56	0.68	0.81
MS2	0.37	0.44	0.51	0.43	0.51	0.63
MS12	0.12	0.15	0.18	0.15	0.18	0.22
Tsai-Hill	0.20	0.29	0.41	0.28	0.41	0.59

6.2.3. Yielding and Failure Analysis

As shown in Section 6.1.4, the sail transmits a compressive and bending force into the boom. From the previous section, it is clear that the aluminum returns to its elastic behavior during deflation, therefore bending and compression can be analyzed independently following the superposition principle.

Buckling

The inflatable boom is a slender, thin-walled cylinder, that can fail under axial compression in two main ways: column buckling and shell buckling.

- **Column Buckling** occurs in long, slender structures, where the boom tends to buckle in a global bending shape.
- **Shell Buckling** occurs in thin-walled structures, where the boom suffers localized dimpling. Shell buckling is highly sensitive to imperfections.

Table 6.9 summarizes the results of the column (P_{CB}) and shell buckling (P_{SB}) critical loads for the non-rigidized (NR) boom configuration and the six rigidized cases.

Table 6.9: Critical failure loads under axial compression of the boom for the different study cases.

	NR		Hot case			Cold case		
	Analytical	**FEM**	**76 kPa**	**92 kPa**	**110 kPa**	**90 kPa**	**110 kPa**	**132 kPa**
P_{CB} **[N]**	595.57	586.51	-	-	-	-	-	-
P_{SB} **[N]**	236.91	238.07	88.00	76.25	51.51	104.45	91.33	69.65
P_{SB} **(I) [N]**	76.28	76.66	28.34	24.55	16.59	33.63	29.41	22.43

* (I) denotes the introduction of imperfections in the calculation through the KDF.

In the non-rigidized case, the critical loads for both buckling modes were calculated analytically following the cylinder shell buckling equation 6.6 [44] and the column buckling equation 6.5 [57]. These analytical results were validated through a linear analysis in Abaqus, resulting in a relative error of 1.5% for the critical column buckling load and -0.5% for the critical shell buckling load.

$$P_{CB} = k\frac{\pi^2 EI}{L^2} \tag{6.5}$$

where P_{CB} is the column buckling critical load, E is the Young´s modulus, I is the second moment of inertia, L is the cylinder´s length and k is a value dependent on the boundary conditions of the problem, for a fixed/free BC $k = 0.25$.

$$N_x = k_x\frac{\pi^2 D}{L^2} \tag{6.6}$$

where N_x is the critical shell buckling line load, k_x is the buckling coefficient, which for $\Gamma Z > 2.85$ is defined in Equation 6.7, Γ is the KDF, Z is the curvature parameter defined in Equation 6.9, D is the wall flexural stiffness per unit width defined in Equation 6.8, L is the cylinder´s length, R is the cylinder's

radius, t is the wall thickness, E is the Young´s modulus and ν is the Poisson´s ratio. The critical shell buckling load $P_{SB} = N_x 2\pi R$

$$k_x = \frac{4\sqrt{3}}{\pi^2}\Gamma Z \tag{6.7}$$

$$D = \frac{Et^3}{12(1-\nu^2)} \tag{6.8}$$

$$Z = \frac{L^2}{Rt}\sqrt{1-\nu^2} \tag{6.9}$$

To determine the critical column buckling load in the FEM, the boom was modeled using beam (B31) elements. The shell FE model should be able to capture the beam buckling mode, but the significant differences in critical loads across modes would require requesting numerous eigenvalues in the model, making the analysis computationally prohibitive. Using beam elements, the first buckling mode under axial compression will always be column buckling.

To determine the effect of the end caps in the critical buckling load for the non-rigidized cases, a model including only the aluminum layer, and a model including the aluminum layer and the caps were analyzed. The analysis revealed a difference of less than 0.1% in the critical load values when end caps were included.

As previously discussed, the critical shell buckling load is highly sensitive to imperfections. *NASA SP-8007* [44] provides an empirical equation to account for reductions in the critical buckling load due to material and geometric imperfections through a Knockdown Factor (KDF), based on the radius-to-thickness ratio of the design. The inflatable boom design has an R/t ratio of 500, thus a KDF of 0.322 is estimated based on the empirical formula. It is important to note that *NASA SP-8007*[44] has not experimentally validated cylinders with a length-to-radius ratio greater than 5, and the boom´s L/R ratio is 20. Furthermore, the assumption that all creases from folding are removed may not be entirely accurate. Therefore testing is necessary to confirm an appropriate KDF that accounts for the structure imperfections, but also the effect of the remaining creases, in case they persist after rigidization.

From the results in the non-rigidized case, even when the KDF is used, the first failing mode in axial compression for the inflatable boom is shell buckling. Figure 6.14 shows the beam buckling and shell buckling modes for the non-rigidized case.

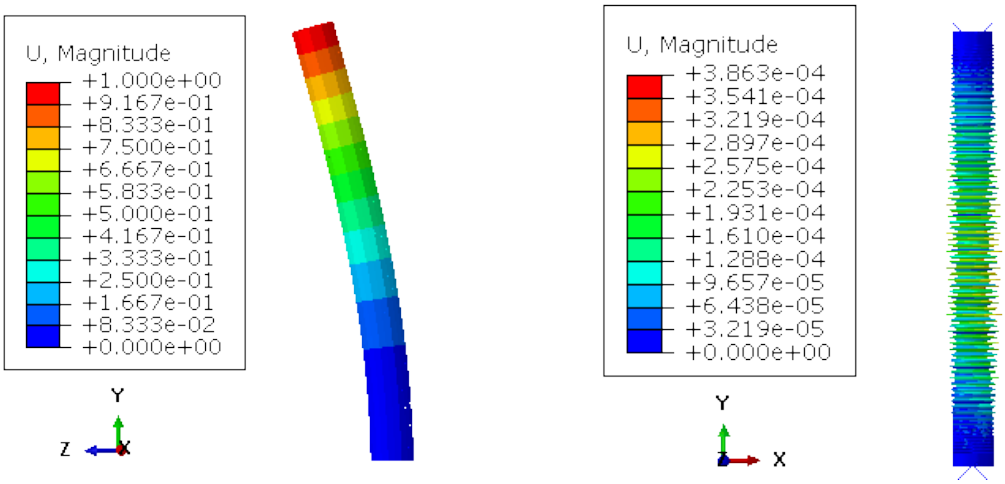

(a) Column Buckling 586.51 N.

(b) Shell Buckling 238.07.

Figure 6.14: Column and Shell Buckling modes for the non-rigidized case. Displacement in m.

For the rigidized cases, where a dynamic implicit quasi-static step was used to model the axial compression analysis, shell buckling was also found to be the failing mode in all cases. Therefore, column buckling was not further studied.

Figure 6.15 shows the force-displacement graph under axial compression for the rigidized booms in the hot case condition, where the sudden drop in the load signals the shell buckling point. The post-buckling behavior of the boom is not studied in this research. A decrease in critical buckling load with increasing inflation pressure is observed, aligning with the Bauschinger effect, where strain rigidization reduces the compressive strength of the material.

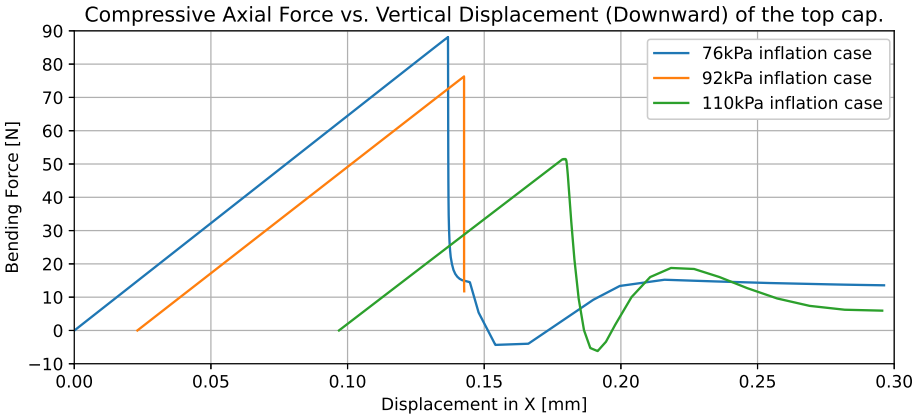

Figure 6.15: Compressive Axial Force vs. Vertical Displacement (downward) for the hot case scenario.

Figure 6.16a illustrates the deformation of the inflatable boom at an inflation pressure of 76 kPa, showing failure near the end cap. Figure 6.16b shows the deformation at an inflation pressure of 110 kPa, where a typical shell buckling pattern is visible in the upper area of the boom. Both figures represent conditions under the hot case scenario. The location and global shape of the deformation under shell buckling are highly dependent on the imperfections of the model, meaning the deformation seen in these figures might not represent the real scenario.

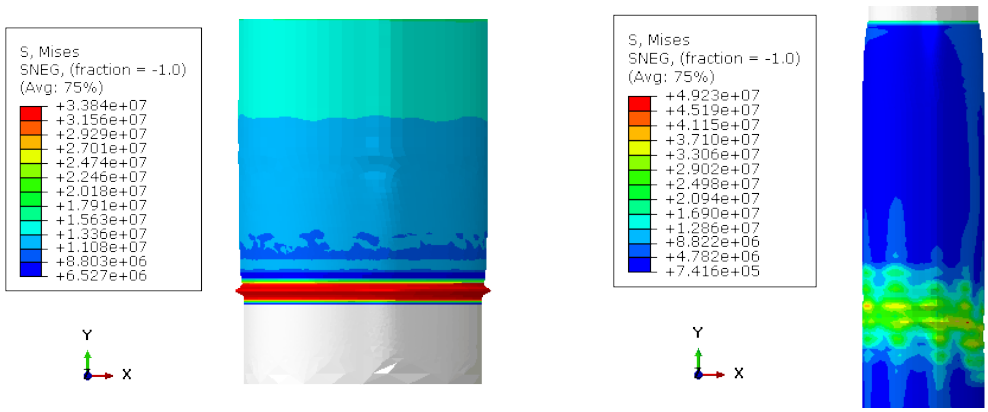

(a) 76 kPa Inflation Pressure.

(b) 110 kPa Inflation Pressure.

Figure 6.16: Deformation of the boom after shell buckling for the 76 kPa and 110 kPa inflation pressures. Stresses in Pa.

The critical shell buckling results need to be corroborated via testing, as the experimental KDF might lower this critical load.

Bending

During the bending analysis, two failing points were studied. The yielding of the material under the horizontal load (P_B), and a sudden reduction in the load-carrying capacity after the material yielding (P_{BH}). Table 6.10 summarizes the results of these analyses for the non-rigidized boom configuration (NR) and the six rigidized cases.

The rigidization technique pushes up the yield strength of the material, but as previously seen, this rigidization is not homogeneous along the whole length of the boom. At the end caps, where failure is expected, the maximum stress after inflation was close to the initial yield strength of the material. Therefore, the initial yield strength of the material (32 MPa for the hot case and 38 MPa for the cold case) will be used as the yield criterion.

Table 6.10: Critical failure loads under bending of the boom for the different study cases.

	NR		Hot case			Cold case		
	Analytical	**FEM**	**76 kPa**	**92 kPa**	**110 kPa**	**90 kPa**	**110 kPa**	**132 kPa**
P_B **[N]**	2.22	2.24	1.505	1.02	1.37	2.03	1.23	1.65
P_{BH} **[N]**	-	6.08	2.29	2.00	1.65	2.72	2.38	1.99

In the non-rigidized case, the critical load before yielding of the material (P_B) was calculated analytically following Equation 6.10. The analytical result was validated through a linear analysis in Abaqus, resulting in a relative error of 0.89%. The final failure load (P_{BH}) was only calculated via FEM.

$$P_B = \frac{\sigma_y I}{Lc} \tag{6.10}$$

where P_B is the bending load that yields the material, σ_y is the yield strength of the material, I is the second moment of inertia, L is the cylinder´s length and c is the distance from the neutral axis to the outermost fiber.

An increase in the maximum horizontal force the boom can withstand before yielding was expected after rigidization, compared to the non-rigidized case. This increase could have been seen if the boom failed in the middle section, but as the boom failed close to the end cap, where the film was not free to rigidize, a small reduction in the critical load is seen.

Figure 6.17 shows the material yielding under bending, with failure occurring as expected at the connection to the lower end cap. The figure highlights the yielding point at the boom's edge on the right side, where there is a high-stress concentration area caused by compression due to bending.

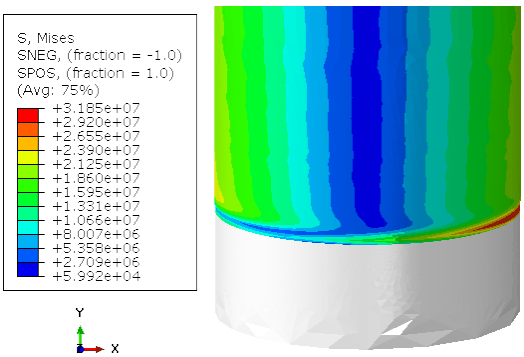

Figure 6.17: Yielding of the boom under bending loading for the hot case 76 kPa inflation pressure. Stresses in Pa.

It is important to note that in bending, the maximum horizontal force the boom can withstand before yielding is lower for the inflation pressure case of 1.5 Py than the 1.25 Py. This difference arises from the material's behavior near the end caps, as discussed in Section 6.2.2. Under horizontal loading, failure occurred near the lower end cap, where the bending moment is greatest. Given that the 1.25 Py

case showed higher residual stresses at this location, it follows logically that yield strength is reached under lower horizontal loads, as observed in the results.

The reduction in load-carrying capacity observed after the material yielding is presented as a 'plastic hinge ' in the boom. This load drop took place post-yielding as the aluminum continued to sustain the applied load during the plastic phase, but before the ultimate strength was reached. This behavior is shown in Figure 6.18. The increase in stiffness of the boom due to the rigidization in the hoop direction is seen in the graph with the increase in the slope before the load drop. The formation of this 'plastic hinge ' signals a critical reduction in the structural capacity of the boom, limiting its ability to sustain further loading even before the UTS is reached. Figure 6.19 shows this plastic hinge for the hot case at an inflation pressure of 76 kPa.

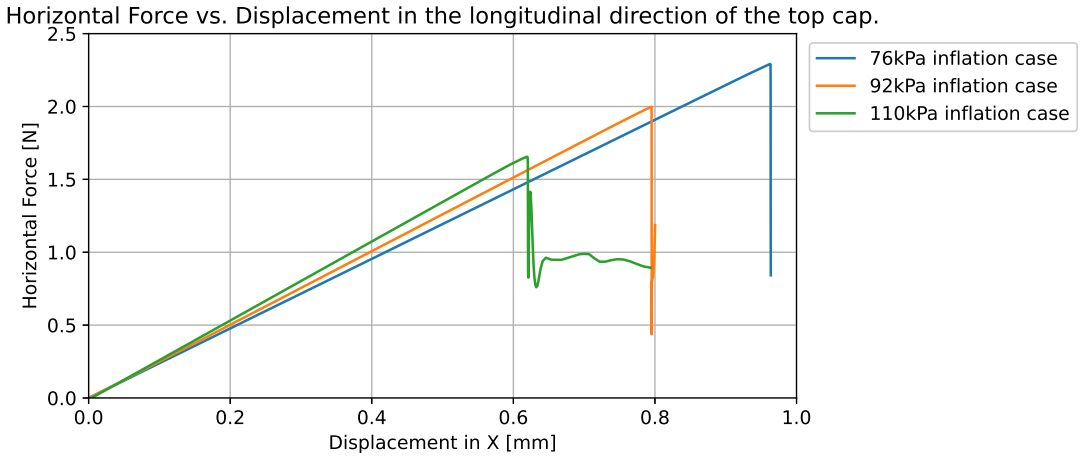

Figure 6.18: Horizontal Force vs. Displacement in the X direction for the hot case scenario.

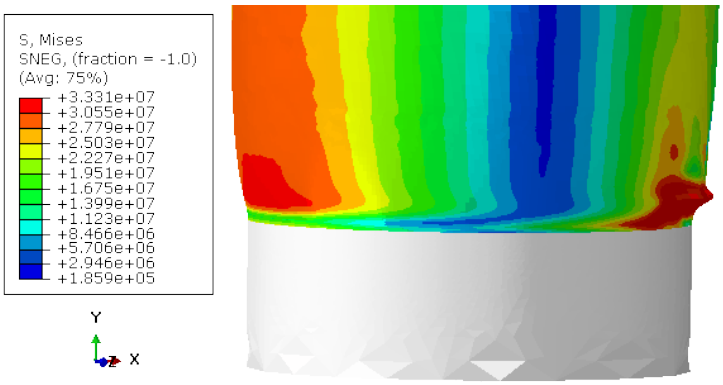

Figure 6.19: Plastic hinge after yielding in bending at an inflation pressure of 76 kPa for the hot case. Stresses in Pa. Deformation Scale Factor x20.

6.2.4. Margins of Safety (MoS)

Table 6.11 and 6.12 present the Margins of Safety (MoS) for the applied load for each design case under bending and axial compression respectively. The conservative loads from the sail simulation, in which pin BC simulated the boom-cap connection are used as the applied load in the calculation.

Table 6.11: MoS of the six boom cases studied under the horizontal bending drag loads for the two sail configurations.

	Hot case			Cold case		
	76 kPa	**92 kPa**	**110 kPa**	**90 kPa**	**110 kPa**	**132 kPa**
P_B **[N]**	1.51	1.02	1.37	2.03	1.23	1.65
P_{BH} **[N]**	2.29	2.00	1.65	2.72	2.38	1.99
Drag force in-plane Conf.1 [N]	0.24					
Drag force in-plane Conf.2 [N]	0.54					
MoS P_B **Conf.1**	5.27	3.23	4.69	7.46	4.10	5.85
MoS P_{BH} **Conf.1**	8.55	7.33	5.89	10.33	8.93	7.29
MoS P_B **Conf.2**	1.78	0.88	1.53	2.76	1.27	2.05
MoS P_{BH} **Conf.2**	3.24	2.70	2.06	4.03	3.41	2.68

Table 6.12: MoS of the six boom cases studied under the axial compression drag loads for the two sail configurations.

	Hot case			Cold case		
	76 kPa	**92 kPa**	**110 kPa**	**90 kPa**	**110 kPa**	**132 kPa**
P_{SB} **[N]**	88.00	76.25	51.51	104.45	91.33	69.65
P_{SB} **(I) [N]**	28.16	24.40	16.48	33.42	26.23	22.29
Drag force out-of-plane Conf.1 [N]	0.28					
Drag force out-of-plane Conf.2 [N]	0.63					
MoS P_{SB} **Conf.1**	313.29	271.32	182.96	372.04	325.18	247.75
MoS P_{SB} **(I) Conf.1**	99.57	86.14	57.87	118.37	103.38	78.60
MoS P_{SB} **Conf.2**	138.68	120.03	80.76	164.79	143.97	109.56
MoS P_{SB} **(I) Conf.2**	43.70	37.73	24.16	52.05	45.39	34.38

For both configurations, the buckling loads show a high margin of safety, suggesting that, even with an increased knockdown factor (KDF) after testing, the boom is unlikely to fail due to buckling.

The MoS in bending for Configuration 1 are relatively high, indicating a substantial safety margin in the design. In contrast, Configuration 2 exhibits comparatively lower MoS values. This is attributed to the increased in-plane loads applied to the booms due to the utilization of tension cables in the sail. Consequently, additional reinforcement may be required to ensure adequate safety margins for this configuration. A redesign of the boom is proposed in Appendix C to achieve a more robust MoS for Configuration 2.

Based on the results presented in this chapter, the primary failure mode for the boom is bending. While it was initially anticipated that higher inflation pressures would result in higher critical bending loads, the opposite behavior was observed. This discrepancy is attributed to inhomogeneous rigidization near the boom-cap connection, where material yielding in bending occurs. Consequently, lower inflation pressures were found to pose higher critical bending loads. Therefore, the lowest pressure that yields the boom should be selected as the inflation pressure for the design. For this design, a CGG capable of providing a pressure range between 76 and 90 kPa is required.

To address the variation in the yield pressure due to orbital temperature changes, two approaches are proposed: a fixed deployment condition and a dynamic adjustment. The fixed deployment condition requires a detailed analysis of the orbital temperature profile and a fixed deployment point. Based on the known temperature at deployment, the CGG would release the full volume of gas stored in the canister, which was previously calculated to reach the inflation pressure. The dynamic adjustment requires the CGG to store the gas volume for the worst-case scenario (cold conditions), combined with a temperature sensor and a valve. The sensor would measure the ambient temperature, and the valve would regulate the gas volume to provide the required inflation pressure.

It is important to note that this analysis assumes all creases from folding are eliminated after rigidization. However, this may not always occur, especially when the lowest pressure that rigidizes the material is used. Residual creases could locally reduce the stiffness of the boom. Testing is essential to validate this assumption and quantify the impact of any remaining creases.

Despite this potential stiffness reduction, the design incorporates a significant safety margin. With a minimum MoS of 1.78 for Configuration 2, the boom can withstand almost two times the expected applied load before yielding in bending in the worst case. This high MoS supports that the design can withstand the applied loads even in the presence of imperfections, such as residual creases or manufacturing imperfections.

7

Modal Analysis

In this chapter, a modal analysis of the two primary components of the drag sail system, the booms and the sail, is conducted to ensure that their natural frequencies are sufficiently separated to prevent resonance and mode coupling. Additionally, the natural frequency of the oscillatory drag load, as determined in Section 4.3, is evaluated to analyze the sail's dynamic response to the aerodynamic forces. Due to the ongoing design development of the drag sail system enclosure and the undecided attachment method to the CubeSat, an analysis of the system's vibrational response relative to the CubeSat structure has not been studied.

7.1. Modal Analysis of the Sail

The drag load acting on the sail increases with decreasing orbital altitude. During the early stages of orbital decay, the drag force is minimal, on the order of 10E-5 N, resulting in a nearly unloaded state for the sail. In this low-drag regime, neither the sail film in Configuration 1 nor the sail film and tension cables in Configuration 2 experience significant tension. Consequently, the overall structural stiffness remains low, resulting in lower natural frequencies. To model the natural frequencies at these stages, a linear frequency analysis was conducted without any prior loading step, assuming small amplitude vibration modes.

In the later stages of decay, as the drag force increases, the sail and cables enter a tensioned state. This added tension stiffens the structure, leading to higher natural frequencies. To capture these conditions, a frequency analysis was performed following an initial loading step, in which the maximum drag load was introduced as a pressure load of 0.085 N/m^2. This pressure load introduced tension into the sail and cables, resulting in higher natural frequencies.

Therefore, the natural frequency range of the sail, from the beginning to the end of the decay, extends from the lowest frequency in the unloaded configuration to the highest frequency in the loaded configuration, taking into account the variation in stiffness due to changing drag loads throughout the orbital decay phase.

The Mass Participation Factor (MPF) was utilized to identify critical modes in the different directions. These modes will excite a high percentage of the total mass of the sail in each direction, representing the primary contributors to the dynamic response of the system.

The drag sail's thin profile and large surface area result in a low out-of-plane stiffness. Consequently, modes with high mass participation in the out-of-plane direction were observed at low frequencies, with 98% of the sail's mass being excited within the first four modes. In contrast, due to the sail's high in-plane stiffness, significantly more energy is required to obtain a considerable MPF in in-plane modes. Despite analyzing the first 50 frequencies, less than 0.02% of the sail's mass was excited in the in-plane direction. In-plane frequencies are less relevant for the system´s primary loading condition, aerodynamic drag, which predominantly acts out-of-plane. As a result, only the out-of-plane modes are considered further in this study.

Table 7.1 summarizes the modes with an MPF higher than 1% for the unloaded sail case, simulating the initial phases of the decay. Table 7.2 summarizes the with an MPF higher than 1% for the tensioned sail case, simulating the final phases of the decay. Both tables contain the natural frequency values for the two sail configurations.

Table 7.1: Out-of-plane frequencies with an MPF higher than 1% for the unloaded case for the two sail Configurations.

Sail Configuration 1			**Sail Configuration 2**		
ID	**Nat Freq [Hz]**	**Participation [%]**	**ID**	**Nat Freq [Hz]**	**Participation [%]**
1	0.2072	93.21	1	0.2026	92.78
3	1.2793	3.59	3	1.2438	3.73
4	2.6664	1.67	4	2.6093	1.70
Total		98.51	**Total**		98.24

Table 7.2: Out-of-plane frequencies with an MPF higher than 1% for the loaded case for the two sail Configurations.

Sail Configuration 1			**Sail Configuration 2**		
ID	**Nat Freq [Hz]**	**Participation [%]**	**ID**	**Nat Freq [Hz]**	**Participation [%]**
1	6.0012	88.22	2	8.5148	90.63
3	11.9400	7.48	3	10.8100	1.48
-	-	-	7	18.1550	3.79
Total		95.76	**Total**		95.94

The sail's primary vibrational response occurs in the out-of-plane direction for Configuration 1 in the frequency range of [0.2072 - 11.9400 Hz] and for Configuration 2 in the frequency range of [0.2026 - 18.1550 Hz].

As it was anticipated, the loaded analysis yielded higher natural frequencies due to the tensioned state of the structure. Incorporating tension cables along the diagonals further increased the system's stiffness, resulting in higher natural frequencies for this configuration in the loaded case.

In contrast, in the unloaded analysis, the small amplitude vibrations around the undeformed configuration limit the cables' contribution to the overall stiffness. In this context, Configuration 2 exhibited even lower natural frequencies than Configuration 1, as shown in Table 7.1. This is due to the fact that, in the linear analysis, the cables primarily increase the system's mass without substantially augmenting its stiffness.

Figure 7.1 shows the main vibration modes corresponding to the unstressed sail for both configurations, which are presented in Table 7.1. The main vibration modes for both configurations are the same, but modes 1 and 3 have opposite directions of the out-of-plane deformation.

Figure 7.2 shows the main vibration modes corresponding to the tensioned sail for both configurations, which are presented in Table 7.2. For Configuration 1 only two modes have a participation factor higher than 1% in the out-of-plane direction for the first 50 frequencies, while for Configuration 2, three modes had a participation higher than 1%. In this analysis, the effect of the tension cables in the vibration modes is clearly seen.

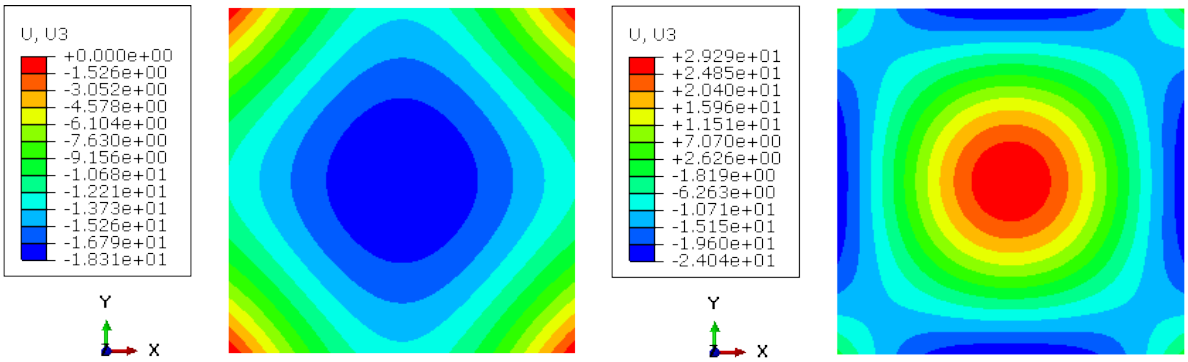

(a) Configuration 1. 1st Mode: 0.2072 Hz.

(b) Configuration 1. 3rd Mode: 1.2793 Hz.

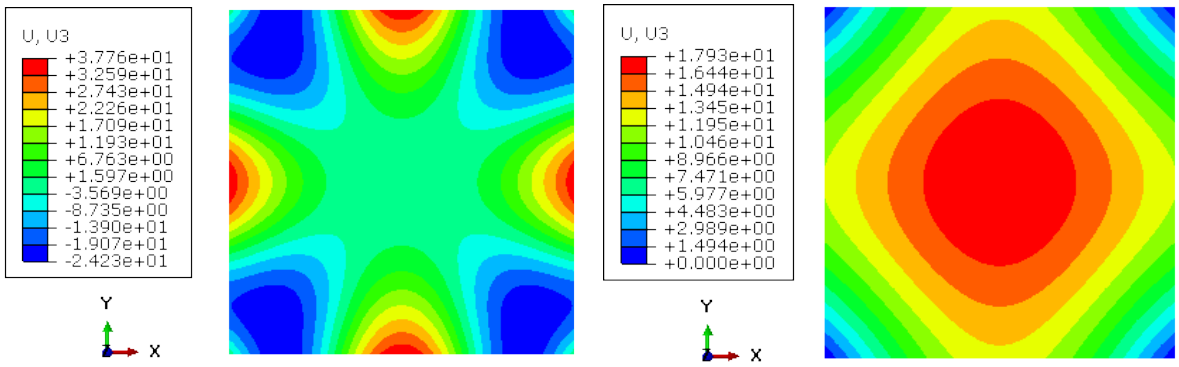

(c) Configuration 1. 4th Mode: 2.6664 Hz.

(d) Configuration 2. 1st Mode: 0.2026 Hz.

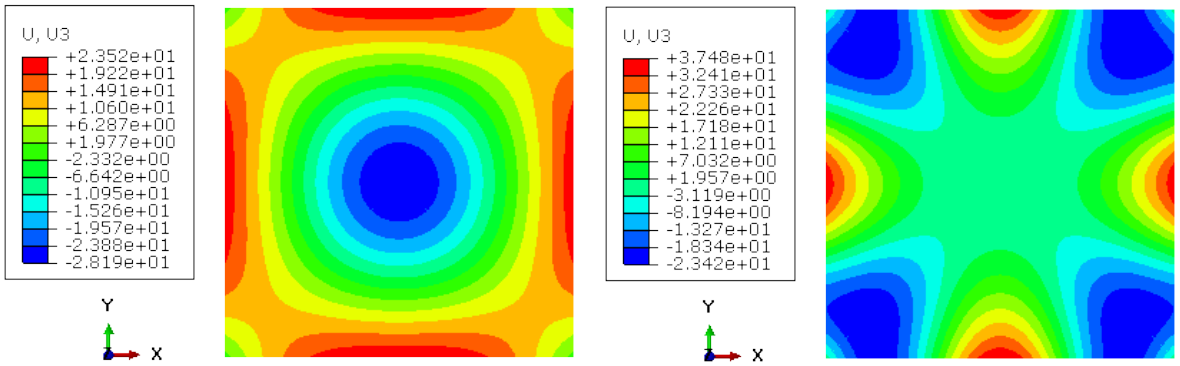

(e) Configuration 2. 3rd Mode: 1.2438 Hz.

(f) Configuration 2. 4th Mode: 2.6093 Hz.

Figure 7.1: Unloaded sail vibration modes for both configurations. Displacement in m.

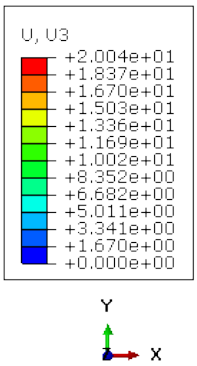

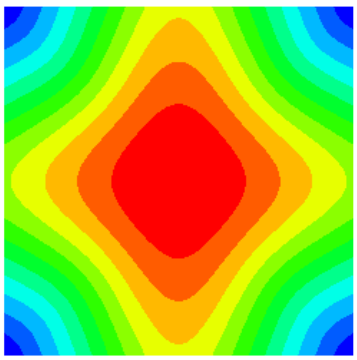

(a) Configuration 1. 1st Mode: 6.001 Hz.

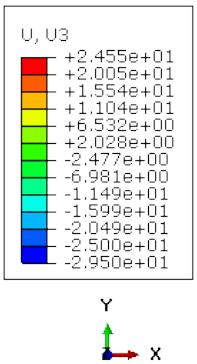

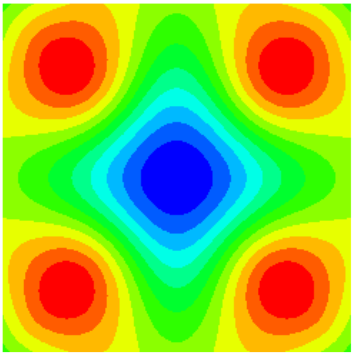

(b) Configuration 1. 3rd Mode: 11.9400.

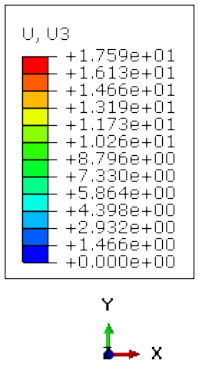

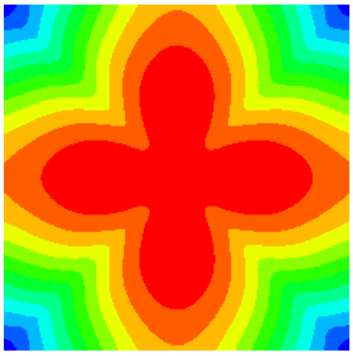

(c) Configuration 2. 2nd Mode: 8.5148 Hz.

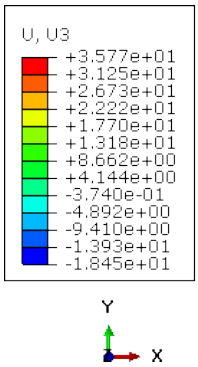

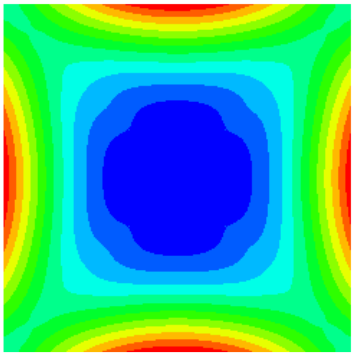

(d) Configuration 2. 3rd Mode: 10.8100 Hz.

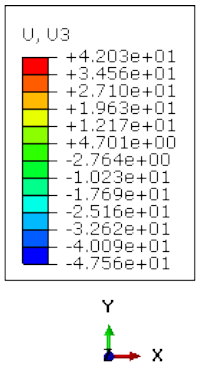

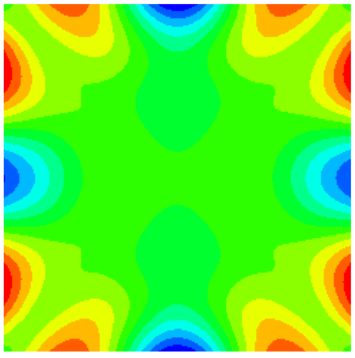

(e) Configuration 2. 7th Mode: 18.1550 Hz.

Figure 7.2: Loaded sail vibration modes for both configurations. Displacement in m.

7.2. Modal Analysis of the Drag Load

The atmospheric drag profile throughout the decay process, obtained in Section 4.3, is shown in Figure 4.15. This profile exhibits an oscillatory trend, primarily due to variations in atmospheric density. This dynamic density variation is accurately represented by incorporating the NRLMSESI-00 atmospheric model into the decay model. The natural frequencies of the atmospheric drag force were calculated, to ensure the natural frequencies of the external loads and sail are far apart, preventing potential coupling between their vibration modes, which can lead to amplifications of the sail´s out-of-plane deformation.

As detailed in Chapter 3, the equation of motion for the CubeSat is solved using a variable-step numerical solver. This solver enhances the model's accuracy and optimizes computational efficiency. However, to accurately determine the natural frequency of the external load, a Fourier transform is required, which is best performed with a constant time step. To satisfy Nyquist's theorem for identifying frequencies up to the sail's highest natural frequency (18 Hz), a time step of 0.025 seconds is necessary. Modeling six years of operation with a constant time step of 0.025 seconds is computationally prohibitive. Therefore, a partition of the decay phase was done, simulating ten orbits in intervals of 1 year. Figure 7.3 shows the points in time at which the natural frequency of the sail was studied.

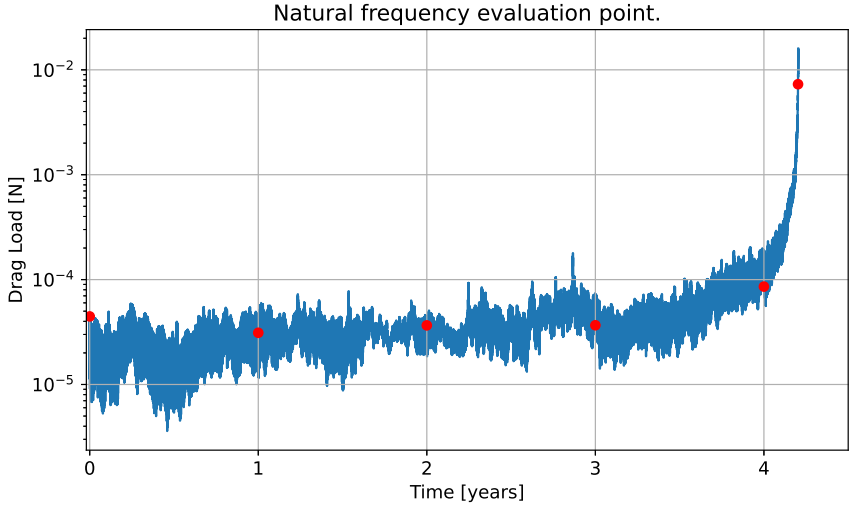

Figure 7.3: Points during the decay at which the natural frequency of the drag force was studied.

To minimize the effect of the quasi-static increase in drag with the decrease in altitude, which introduces a close to 0 Hz natural frequency, the effective drag area was reduced to 0.001 m^2, focusing the analysis on the oscillatory behavior induced by the atmospheric density alone. Figure 7.4 presents the drag profile at the initial altitude studied (550 km). As observed, the force is not centered at zero, so an amplitude shift is applied at each altitude to eliminate the 0 Hz frequency component.

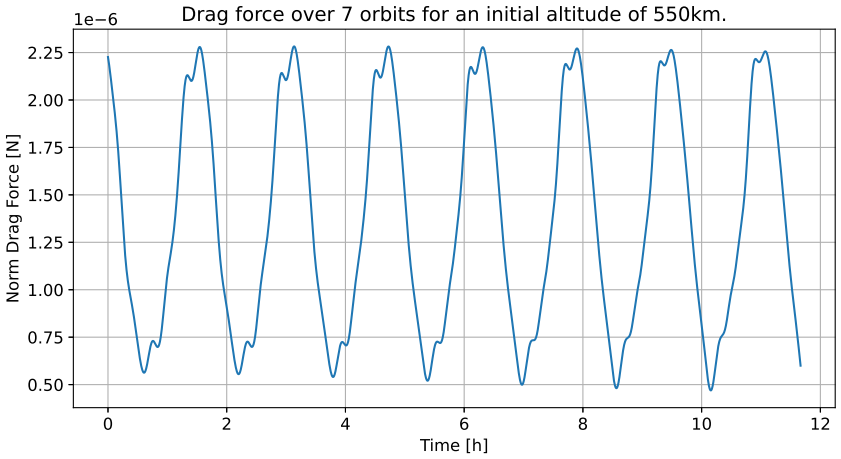

Figure 7.4: Drag profile for 7 orbits at an altitude of 550 km.

Table 7.3 lists the primary natural frequencies (FFT peaks) for all altitudes examined. For this analysis the long-term oscillatory effects in atmospheric density due to the 11-year solar cycle, seasonal variations, and the 27-day solar rotation cycle [69] were excluded. This approach does not capture

the complete frequency spectrum of the drag force. However, the excluded oscillations have very long periods, which excite low frequencies, well below the orbital frequency and far from the first natural frequency of the sail. Therefore, these components are not relevant to the resonance risk assessment of the sail structure.

Table 7.3: Natural frequencies of the drag load for the different altitudes studied.

	550 km	**506 km**	**459 km**	**401 km**	**315 km**	**177 km**
1/T [Hz]	1.74E-4	1.76E-4	1.78E-4	1.80E-4	1.84E-4	1.90E-4
1st Nat Freq [Hz]	1.67E-5	3.33E-5	-	1.67E-5	1.67E-5	1.67E-5
2st Nat Freq [Hz]	1.67E-4	1.83E-4	1.83E-4	1.83E-4	1.83E-4	1.83E-4
3nd Nat Freq [Hz]	3.50E-4	3.50E-4	3.67E-4	3.50E-4	3.67E-4	3.83E-4
4rd Nat Freq [Hz]	5.17E-4	5.33E-4	5.33E-4	5.33E-4	5.50E-4	5.83E-4
5th Nat Freq [Hz]	7.00E-4	7.00E-4	7.17E-4	7.17E-4	7.33E-4	7.67E-4
6th Nat Freq [Hz]	8.67E-4	8.83E-4	9.00E-4	9.00E-4	9.17E-4	9.50E-4
7th Nat Freq [Hz]	1.07E-3	1.07E-3	1.07E-3	1.08E-3	1.10E-3	1.15E-3

In all cases, the second natural frequency, which showed the highest amplitude, consistently appeared between 0.00017 and 0.00018 Hz, aligning with the orbital period (T). The first natural frequency, which is one order of magnitude smaller, may result from the quasi-static increase in drag force, as reducing the effective drag sail area did not fully mitigate this effect. Higher natural frequencies were also detected but with low amplitudes in the FFT, indicating faster, repetitive disturbances.

As shown in Table 7.3, the highest natural frequency of the atmospheric drag load was found to be 1.15E-3 Hz, which is two orders of magnitude below the first natural frequency of the sail. Therefore, we conclude that there will be no coupling between the external drag force and the sail's structural modes. Consequently, no amplification of sail displacements is expected, which mitigates the risk of reduced effective drag area or potential sail failure.

Figures 7.6 and 7.8 illustrate the Fast Fourier Transform (FFT) results for the drag force at 550 km (initial altitude) and 177 km (final altitude).

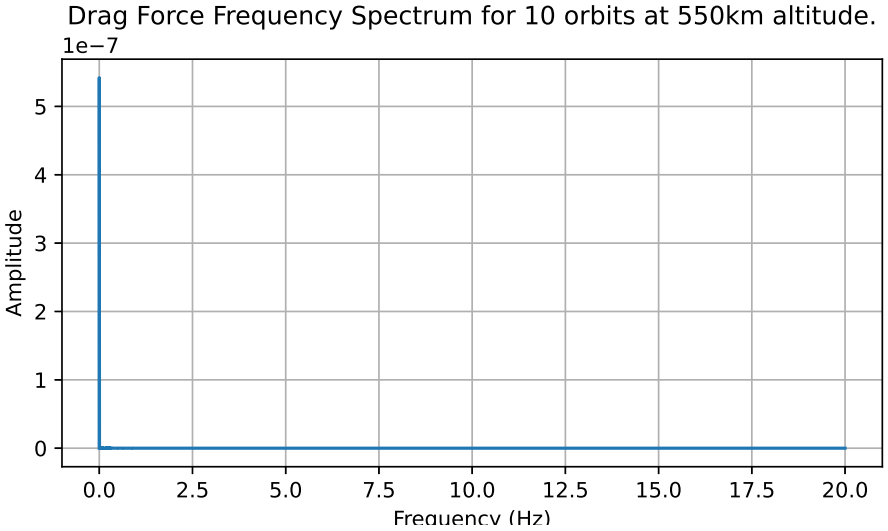

Figure 7.5: FFT of the drag force up to 18 Hz at an altitude of 550 km.

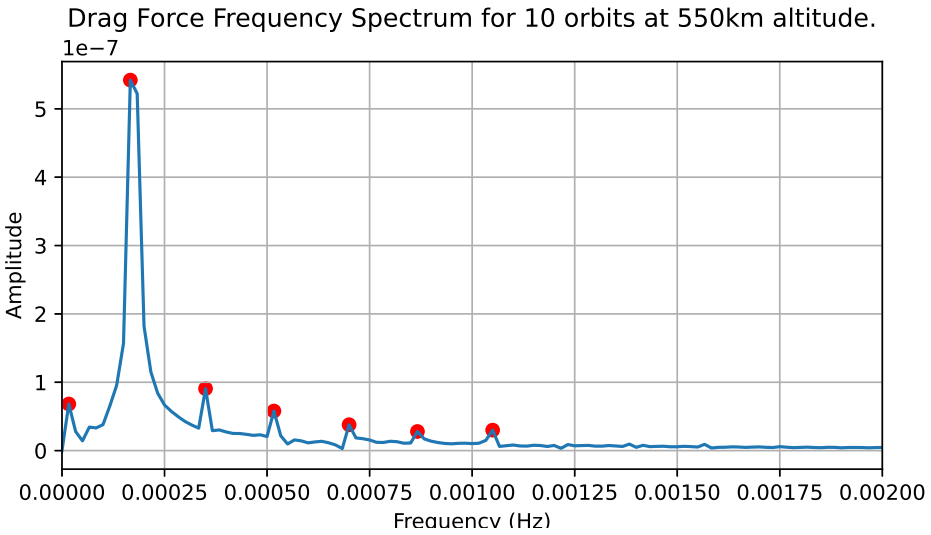

Figure 7.6: Excited frequencies of the drag force at an altitude of 550 km.

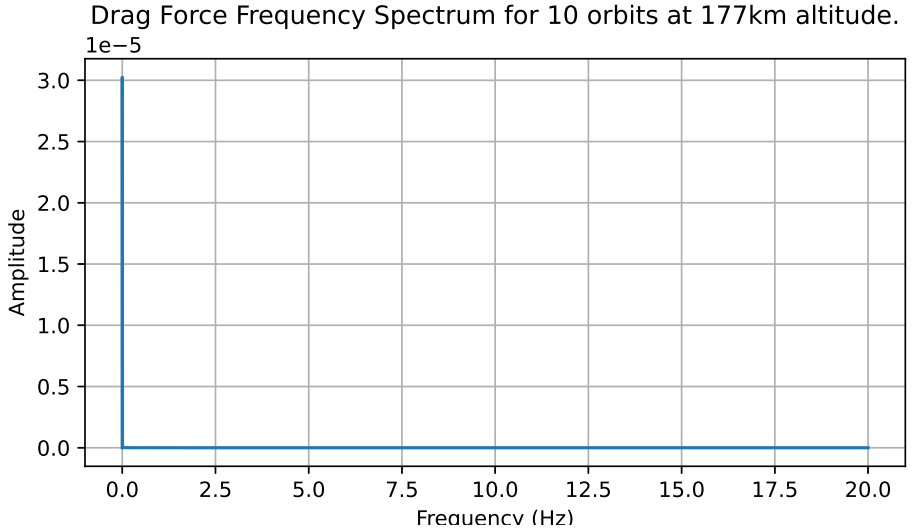

Figure 7.7: FFT of the drag force up to 18 Hz at an altitude of 177 km.

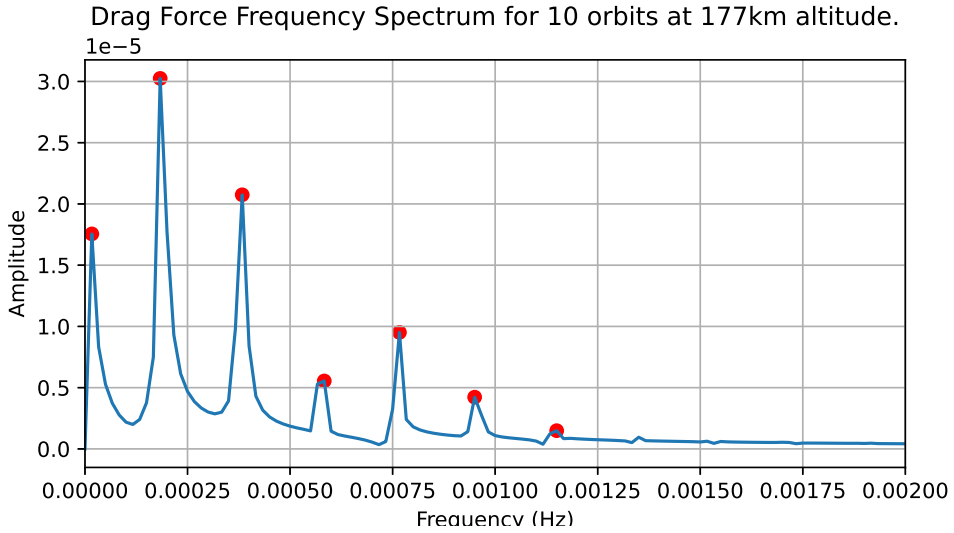

Figure 7.8: Excited frequencies of the drag force at an altitude of 177 km.

7.3. Modal Analysis of the Booms

The tangent stiffness is used for nonlinear analysis to estimate the stiffness of the system at each iteration point. The tangent stiffness matrix can be divided into a constitutive stiffness matrix and a geometric stiffness matrix. The constitutive stiffness matrix accounts for changes in the material properties such as Young´s modulus or poison ratio. This matrix is constant for linear analysis but has to be updated every iteration for nonlinear analysis when the plastic deformation of the material changes its structural behavior. The geometric stiffness matrix accounts for the change in stiffness due to the deformation and stress state of the system. Linear frequency analysis in Abaqus takes into account the residual stress and deformation state of the system from previous steps, but it does not account for the change in material stiffness after yielding, as it assumes linear elastic behavior around the deformed shape.

For the aluminum boom, after deflation, when the material returns to the elastic phase, its elastic modulus (constitutive stiffness), does not change after yielding. This can be seen in the stress-strain graph in Figure 6.11, where the elastic loading slope (inflation) is parallel to the unloading slope (deflation) after plastic deformation. Therefore, it can be assumed that the boom´s response to small vibrations remains similar before and after yielding. This allows for a linear frequency analysis to be valid post-deflation because the material's stiffness while having been plastically deformed, will still respond elastically and linearly to small oscillations.

The possible localized non-linear behavior in the areas close to the cap-boom connection led to changes in stiffness due to geometric effects or residual plastic deformation. However, these regions are so localized that are unlikely to impact the overall modal behavior of the boom. Moreover, as explained before, the residual stress state of the boom from the previous step is kept for the linear frequency analysis, providing a more accurate representation of the current state.

A linear frequency analysis will be used to determine the mode shapes of the inflatable booms after inflation-deflation. The linear approximation gives an appropriate estimation in this case because aluminum retains its stiffness post-yield, the nonlinearity close to the end caps is a localized effect that may not contribute significantly to the overall stiffness, and the analysis accounts for the boom´s stress state after rigidization. Table 7.4 contains the first natural frequency of the inflatable boom for each analyzed case and its participation factor.

Table 7.4: Natural frequencies of the inflatable booms with an MPF higher than 1% for the different cases studied.

	NatFreq X [Hz]	P [%]	NatFreq Y [Hz]	P [%]	NatFreq Z [Hz]	P [%]
HC-76	54.153	49.56	907.17	50.98	54.153	49.56
HC-92	55.72	50.01	902.93	50.99	55.72	50.01
HC-110	57.75	50.06	896.06	51.00	57.75	50.06
CC-90	54.10	49.59	907.24	58.98	54.10	49.59
CC-110	55.36	50.01	903.51	50.99	55.36	50.01
CC-132	56.85	50.05	897.78	51.01	56.85	50.05

As the inflation pressure increases, residual stresses introduced during rigidization enhance the stiffness in the hoop direction of the boom, increasing its natural frequencies in X and Z. These modes correspond to global bending, as shown in Figure 7.9a for the hot case at an inflation pressure of 76 kPa. Conversely, in the out-of-plane direction, natural frequencies decrease with increasing inflation pressure. This reduction is a result of the reduction in compressive strength of the boom after its rigidization. This direction of excitation reveals a shell buckling mode as shown in Figure 7.9b for the same case, occurring at a relatively high frequency.

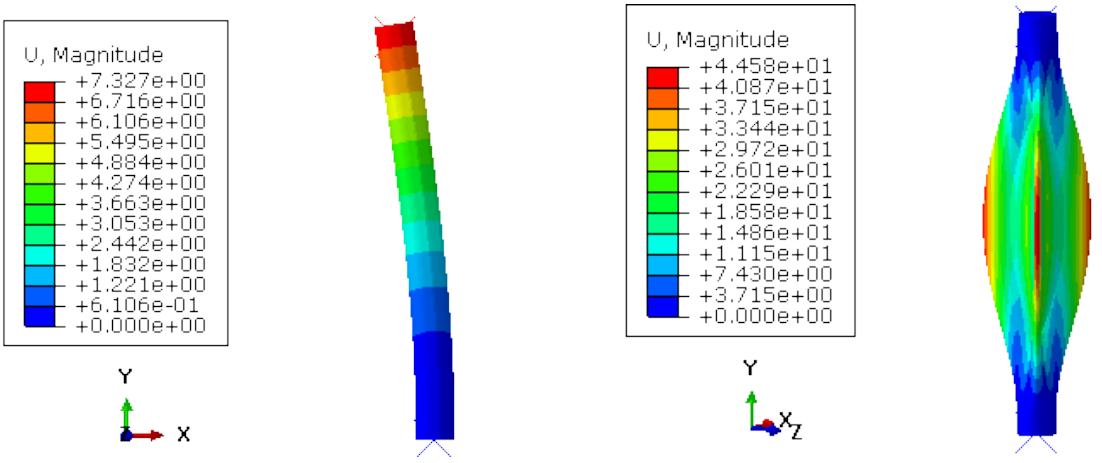

(a) Bending Mode, 54.153 Hz. Scale factor = 1E-2.

(b) Compresion Mode, 397.72 Hz. Scale factor = 7.23E-4.

Figure 7.9: Bending and compression boom vibration modes for the hot case 76 kPa inflation pressure. Displacement in m.

7.4. Natural Frequency Requirements of the Drag Sail System

The dynamic analysis required two conditions to be met: (1) a clear separation between the natural frequencies of the drag load and drag sail, and (2) a clear separation between the natural frequencies of the sail and booms.

To comply with condition 1 and ensure the drag load would not induce resonance in the sail, the lowest natural frequency of the sail needed to exceed twice the highest natural frequency of the drag load. The highest estimated natural frequency of the drag load was 1.15 E-3 Hz, two orders of magnitude lower than the first natural frequency of the sail 0.2 Hz. Therefore, the first requirement is met with a wide margin.

The separation of the natural frequencies of the sail and boom was essential to avoid vibration mode coupling, which could lead to resonance under unexpected high-amplitude loads during the in-orbit phase. To satisfy this condition, the first natural frequency of the boom was required to be at least twice the magnitude of the last natural frequency of the sail. In the least stiff boom case, the first natural frequency (54.1 Hz) was 4.5 times higher in Configuration 1 (11.94 Hz) and 3 times higher in Configuration 2 (18.15 Hz), successfully meeting the second condition.

8

Final Design and Requirements Analysis

In this chapter, the final sail configuration is selected based on the structural and modal constraints of the design. A full system analysis is conducted to determine the minimum altitude at which the deorbiting system can withstand mechanical drag loads without failing. A second full analysis is performed for the altitude of 160 km conditions, the decay limit altitude established in the orbital decay model, to corroborate the part analysis results in Section 6.2. Finally, the system requirements are reviewed, along with their status following this study.

8.1. Sail Configuration Selection

For the two sail configuration cases the following criteria were studied:

1. **Deflection of the sail due to the drag load** discussed in Section 6.1. The out-of-plane deflection of the sail reduces the effective drag sail area. Configuration 1 had a deflection of 2.12 mm, and Configuration 2 of 0.95 mm. The deflection of Configuration 2 was half the deflection of Configuration 1 due to the use of tension cables. The tension cables allow part of the load to be distributed across the wires, reducing the load carried by the fabric of the sail. Still, both configurations can be considered to have a negligible deflection, leading to no reduction of the effective drag area, and therefore no increase in the decay time.
2. **Stresses on the sail due to the drag load** discussed in Section 6.1. Table 6.2 shows that the stresses in the sail in Configuration 2 are one order of magnitude smaller than in Configuration 1, as the tension cables take part of the load, preventing the fabric from withstanding the full drag force. Still, the yielding criteria used (Tsai-Hill and Maximum stress), show that the stresses in both configurations are far from the yielding point, hence, both configurations can resist the drag loads without failing.
3. **Coupling of the vibration modes of the sail with the natural frequency of the drag load** discussed in Chapter 7. The highest natural frequency of the drag load is 1.15E-3 Hz, and the first natural frequency of the sail in Configuration 1 and 2 is 0.21 Hz and 0.20 Hz respectively. Both modes are more than 200 times apart, thus coupling of the drag load and the sail modes is not expected for any of the configurations.
4. **Coupling of the vibration modes of the sail and the boom** discussed in Chapter 7. The highest relevant sail natural frequency (with an MPF higher than 1%) in Configuration 1 and Configuration 2 are 11.9 Hz and 18.2 Hz respectively. The first natural frequency of the boom for the least stiff case (lowest inflation pressure) is 54.1 Hz. The boom's first natural frequency is 4.6 times the sail's natural frequency in Configuration 1 and 3.0 times in Configuration 2. Even though the modes for Configuration 1 are further apart, both margins are enough not to expect coupling between the boom and the sail in either configuration under external loads.

5. **Yielding of the boom under high drag loads** discussed in Section 6.2. It was seen that the first failing mode of the boom under the drag load was bending. For both configurations, the margins of safety were sufficiently high to confirm that the boom could withstand the drag load down to an altitude of 160 km. However, the analysis assumes that any creases caused by folding are entirely eliminated after rigidization. This assumption requires further validation, as it may not accurately reflect real-world conditions, leading to local reduction in the stiffness of the boom where the creases remain. Configuration 1 has larger MoS, better suited to resist the loads in case of stiffness reduction. Moreover, if the sail and booms do not disintegrate before the estimated deorbit altitude of 160 km, Configuration 1 provides booms with a greater MoS to withstand the increasing drag loads further in the decay trajectory.

Following the above-discussed points, **Configuration 1 has been selected as the final design** for this research. In case lower out-of-plane deflection or lower stresses in the sail have a higher impact on the design decision, Configuration 2 can be used. Appendix C presents a strengthening study for the boom design, achieving higher MoS under the drag loads.

8.2. Full System Structural Analysis

The complete system employing sail Configuration 1 was modeled in Abaqus to account for potential nonlinearities near the boom-cap connection, as discussed in Section 6.2.2. This model also aims to evaluate the effect of combined loading on the design, as the boom simultaneously experiences bending and axial compression. In Section 6.2.3, these loading contributions were analyzed independently.

In the full system model, the geometry, material, and mesh of the sail and booms were modeled following the same approach as the independent parts model defined in Section 6.2.1 for the boom and Section 6.1.1 for the sail. To model the attachment between both parts, a chamfer was created in the top cap, with the same angle w.r.t. the vertical as the sail. This allows a surface-to-surface pin connection between the sail and the top end cap. A node-to-node connection between the node on the corner of the sail and the mid-point of the boom was also studied, but this approach provides unrealistic stress concentrators at the attachment point that can cause overly conservative results or even convergence issues in the model. Figure 8.1 shows the connection between both parts.

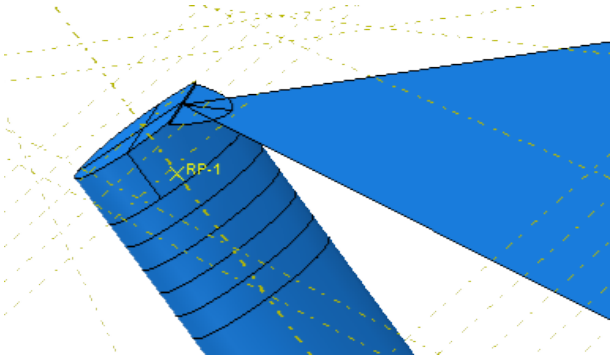

Figure 8.1: Boom-sail surface-to-surface connection.

For the rigidization of the boom, a static general step with the non-linearities option activated was used the same way as it was explained in Section 6.2.1. A Dynamic implicit Quasi-static step was used for the pressure loading in the sail after the rigidization. As the yield point of the boom is one of the desired outcomes from the analysis, a pressure of 5 Pa was used in the sail. Figures 8.2 to 8.5 show the initial design, the system after inflation, the system after deflation and the system after sail loading, for the 110 kPa inflation hot case. The deformation in the system has been scaled (x2) to properly show the state of the system. The stress magnitudes shown in the legend are in Pa.

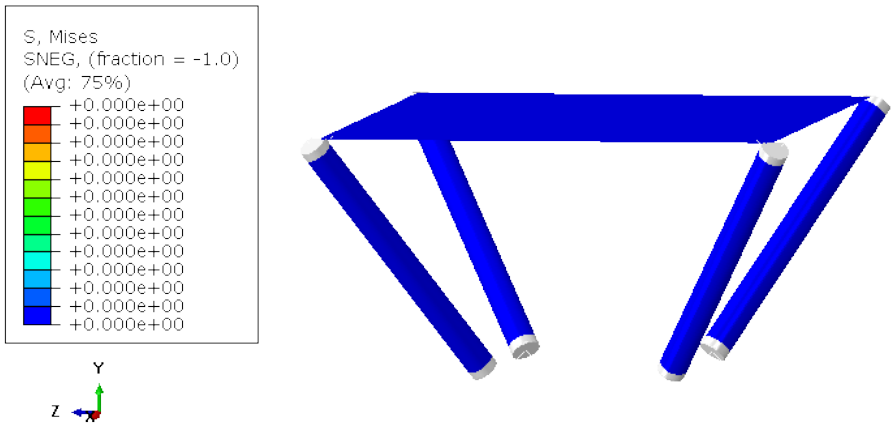

Figure 8.2: Full system model, hot case 110 kPa inflation pressure. System before loading.

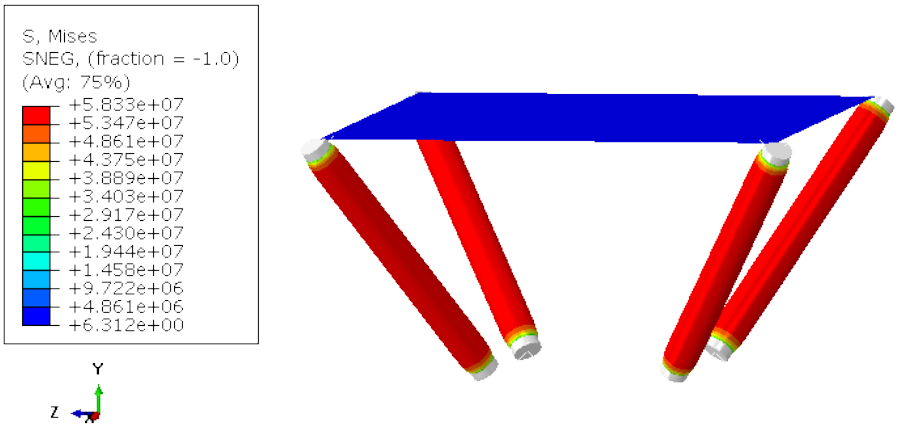

Figure 8.3: Full system model, hot case 110 kPa inflation pressure. System after boom inflation.

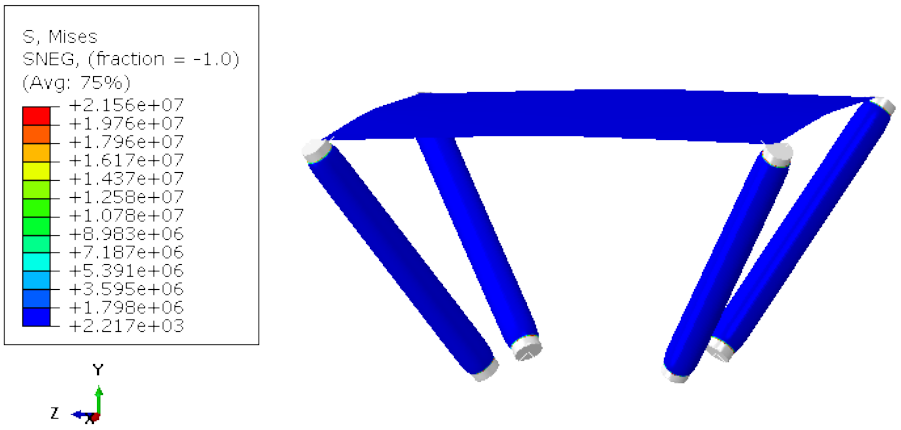

Figure 8.4: Full system model, hot case 110 kPa inflation pressure. System after deflation.

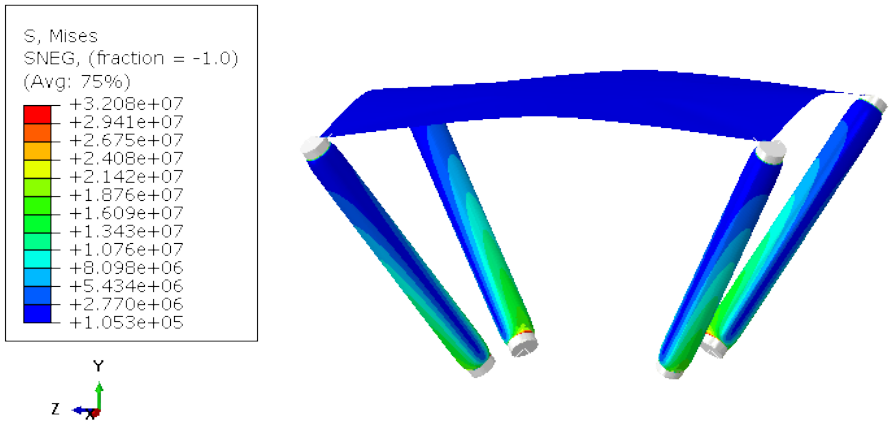

Figure 8.5: Full system model, hot case 110 kPa inflation pressure. System after sail loading at boom yielding point.

8.2.1. Yielding of the boom

The yielding point of the booms in the full system analysis was studied and compared with the results from the part analysis, to determine the effect of the compressive axial load in the failing mode. Table 8.1 summarizes the yield load in bending obtained from the full system analysis for all the studied cases and its difference from the part analysis in Section 6.2.

Table 8.1: Maximum horizontal load at yielding for the hot and cold inflation pressure cases and its difference with the part analysis performed in Section 6.2.

	Hot Case			**Cold Case**		
	76 kPa	**92 kPa**	**110 kPa**	**90 kPa**	**110 kPa**	**132** kPa
P_B **[N]**	1.51	1.02	1.37	2.03	1.23	1.65
Difference part FEM[%]	-12.72	-11.304	-11.62	-12.50	-10.87	-11.29

Figure 8.6 shows the stress state of the boom at its yielding point for the 76 kPa inflation pressure hot case.

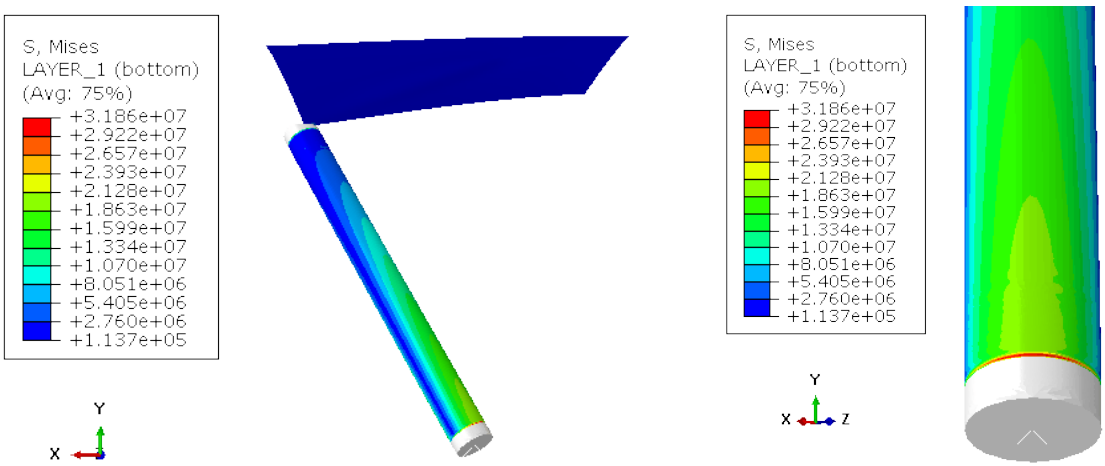

(a) Stress state shown for 1/4 of the design.

(b) Close-up look into the boom´s yielding area.

Figure 8.6: Full system analysis for the 76 kPa inflation hot case at the yielding point. Stresses in Pa.

The reaction forces were obtained in the global coordinate system of the model, which corresponds with the sail local coordinate system, thus the rotation in Section 6.1.4 was used to determine the applied forces in the boom´s coordinate system, this way the comparison with the part analysis is possible. In

the full system analysis, it is clear that bending is also the first failing mode. The maximum bending load at which yielding occurs is observed to be 10-12% lower compared to the part analysis which only considered bending. This reduction can be attributed to the combined loading effects present in the full system configuration, where the boom is subjected to both compression and bending. The superposition of these two load types creates a more complex stress state in the boom, leading to an earlier yielding.

The drag pressure in the sail P_d at which the yield of the boom is reached is defined in Table 8.2. The pressure values have an SF of 1.25 according to the ESA standard ECSS-E-ST-32-10C Rev.2 [21]. A decay simulation of the host spacecraft with the drag sail system deployed was performed to determine the altitude at which these drag pressures in the sail are achieved.

Table 8.2: Maximum drag pressure in the sail that yields the boom (with a SF of 1.25) and the altitude during the decay at which this pressure is reached.

	Hot Case			**Cold Case**		
	76 kPa	**92 kPa**	**110 kPa**	**90 kPa**	**110 kPa**	**132 kPa**
P_d **[Pa]**	2.38	1.27	1.92	3.71	1.68	2.58
Altitude [km]	116	121	117	113	118	115

The lowest point in the decay, where the booms are able to resist the drag load could not be calculated from the part model, as the ratio between the axial compressive and horizontal load is not constant. The full system design allows this estimation. Therefore, it can be seen from the full system results that the booms will survive the mechanical drag loads down to an altitude of 120 km, considering there is no local reduction in the stiffness of the boom due to remaining creases after rigidization. This is lower than the initially estimated final decay altitude of 160 km, providing a conservative estimate for the decay time and increasing the reliability of the design (RS-07).

8.2.2. Stress analysis on the sail

The stresses on the sail were analyzed to determine if the sail could withstand the higher drag pressure loads at an altitude of 120 km. The two criteria used for the Mylar layer (orthotropic material) were the Tsai-Hill and Maximum Stress (MS) criteria. Table 8.3 summarizes the stress observed in the mid-plane of the sail and the values of the yielding criteria. All failure criteria were well below 1, therefore it is reasonable to conclude that the sail can withstand these higher-pressure drag loads without failing.

Table 8.3: Stress in the hoop direction (1) longitudinal direction (2) and shear stress (12) in the mid-plane of the sail for the full system analysis under the different drag pressure cases.

	Hot Case			**Cold Case**		
	76 kPa	**92 kPa**	**110 kPa**	**90 kPa**	**110 kPa**	**132 kPa**
Max stress 1 [MPa]	2.14	1.26	1.77	3.08	1.60	2.27
Max stress 2 [MPa]	2.17	1.28	1.79	3.14	1.62	2.30
Max shear stress 12 [MPa]	1.03	0.55	0.83	1.58	0.73	1.11
MS1	0.06	0.04	0.05	0.09	0.09	0.07
MS2	0.06	0.04	0.05	0.09	0.09	0.07
MS12	0.03	0.02	0.02	0.05	0.02	0.03
Tsai-Hill	0.007	0.002	0.005	0.017	0.004	0.008

8.2.3. Vibration modes of the sail

Since the current model incorporates the sail-boom attachment and accounts for a higher drag pressure, the natural frequencies of the system will change significantly. The most notable differences are expected in the loaded configuration, where the increased drag pressure (3.71 Pa) further tensions the sail, leading to higher natural frequencies compared to the part-level analysis under 0.085 Pa drag pressure (as discussed in Section 7.2).

The Mass Participation Factor (MPF) in this scenario does not provide a reliable measure of participation percentages, as the analysis includes the mass and dynamics of the entire sail-boom system.

To better interpret the results, Figures 8.8, 8.10, 8.12 and 8.14 illustrate the out-of-plane deformation modes separately for the sail and boom (deformation in m), even though the analysis was conducted for the full system. This separation allows for clearer identification of whether specific vibration modes predominantly correspond to the sail or the boom.

Table 8.4 summarizes the new natural frequencies of the sail in the unloaded and loaded state (drag pressure of 3.71 Pa). The cumulative sum of the MPF is now higher than 100%, as only the mass of the sail has been taken into account for the analysis and the vibration modes also excite the boom. In this analysis, modes with an MPF greater than 5% have been considered, as opposed to the 1% used in the part-level analysis. This higher MPF accounts for the additional contribution of the boom's mass in the full-system model. Figure 8.7 and 8.9 show the two modes with an MPF higher than 5% for the unloaded case and Figure 8.11 and 8.13 show the two modes with an MPF higher than 5% for the loaded case, all displacements are in m.

Table 8.4: Out-of-plane frequencies with an MPF higher than 5% for the unloaded and loaded cases.

Unloaded case			Loaded case		
ID	**Nat Freq [Hz]**	**Participation [%]**	**ID**	**Nat Freq [Hz]**	**Participation [%]**
1	0.3017	97.17	1	12.966	141.46
3	1.3066	6.03	4	20.932	12.17
Total		103.20	**Total**		153.63

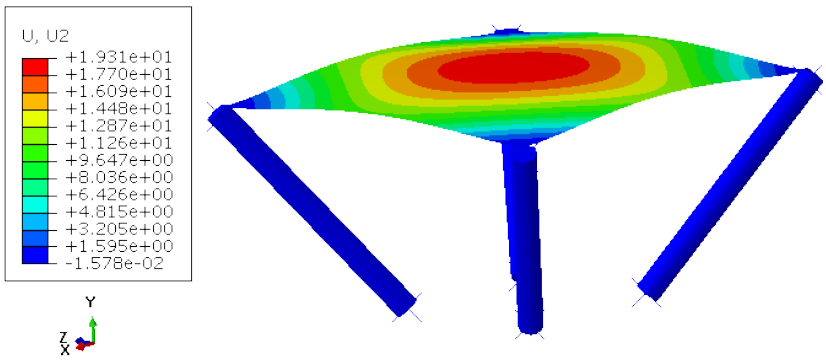

Figure 8.7: 1^{st} sail vibration mode in the unloaded case (0.3017 Hz).

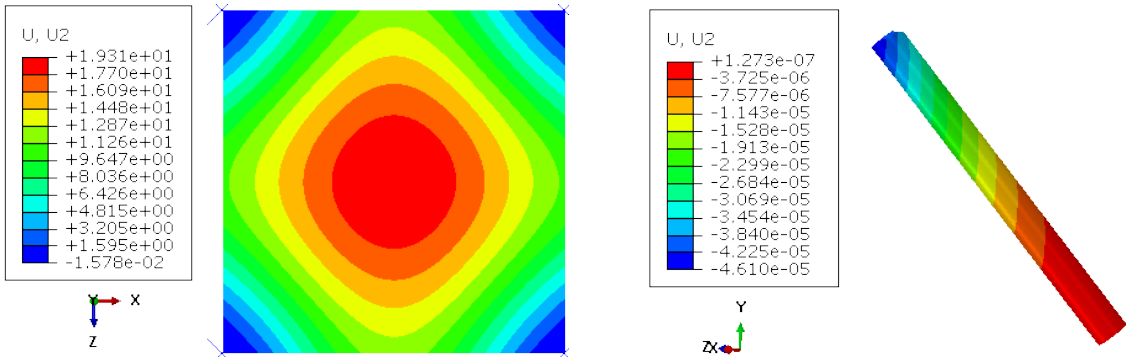

(a) Excitation of the sail. **(b)** Excitation of the boom.

Figure 8.8: Excitation of the 1^{st} sail vibration mode in the unloaded case (0.3017 Hz) by parts.

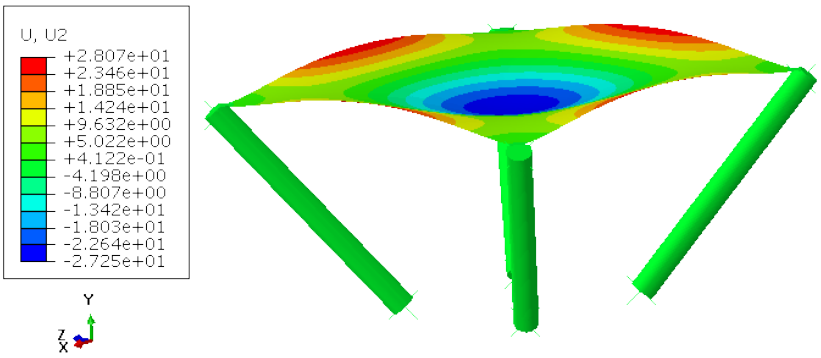

Figure 8.9: 3^{rd} sail vibration mode in the unloaded case (1.3066 Hz).

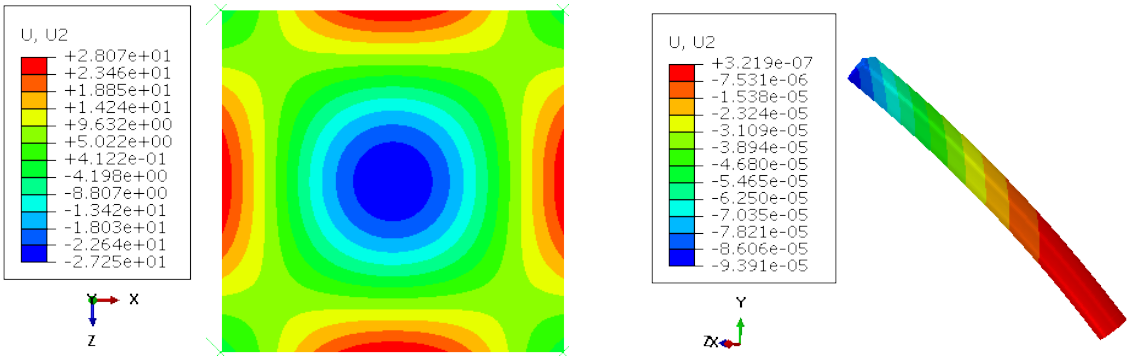

(a) Excitation of the sail. **(b)** Excitation of the boom.

Figure 8.10: Excitation of the 3^{rd} sail vibration mode in the unloaded case (1.3066 Hz) by parts.

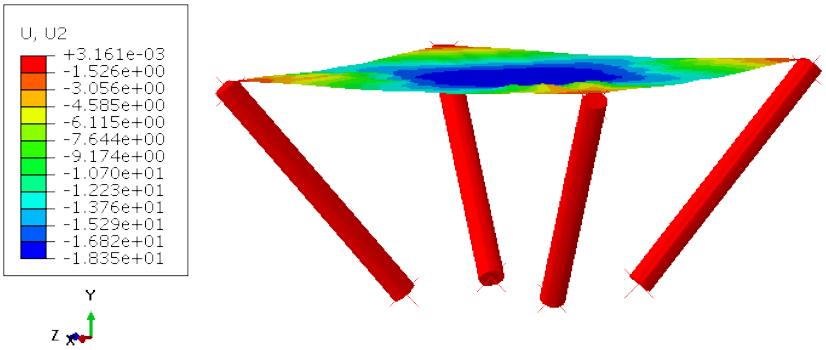

Figure 8.11: 1^{st} sail vibration mode in the loaded case (12.966 Hz).

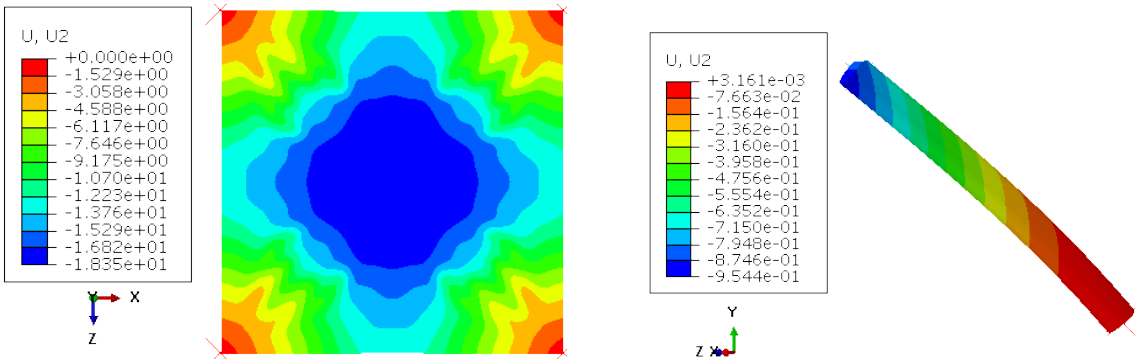

(a) Excitation of the sail. **(b)** Excitation of the boom..

Figure 8.12: Excitation of the 1^{st} sail vibration mode in the loaded case (12.966 Hz) by parts.

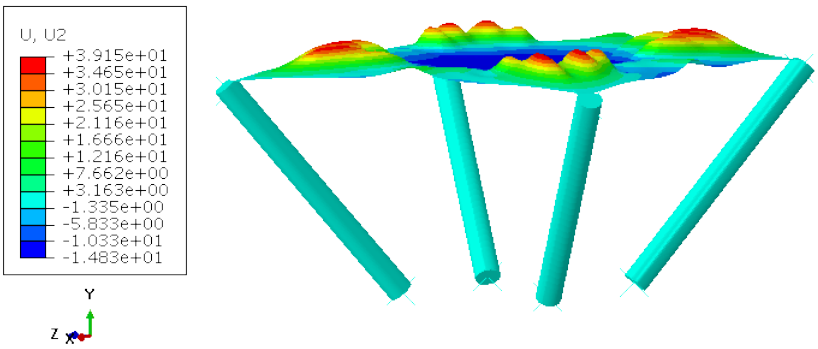

Figure 8.13: 4^{th} sail vibration mode in the loaded case (20.932 Hz).

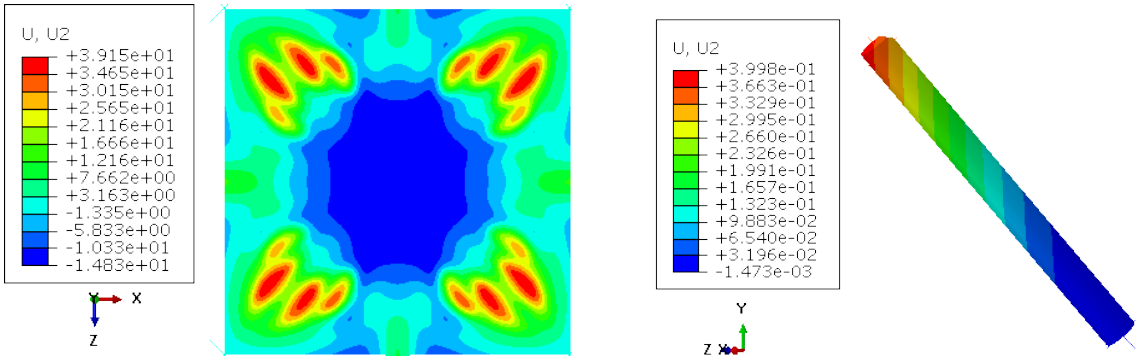

(a) Excitation of the sail. **(b)** Excitation of the boom.

Figure 8.14: Excitation of the 4^{th} sail vibration mode in the loaded case (20.932 Hz) by parts.

Both the unloaded and loaded cases exhibit vibration modes similar to those observed in the part-level modal analysis. Specifically, the unloaded full-system vibration modes correspond closely to those shown in Figures 7.1a and 7.1b of the unloaded part-level analysis. Similarly, the loaded full-system vibration modes align with those shown in Figures 7.2a and 7.2b of the loaded part-level analysis.

In all cases studied, it is evident that the low-frequency vibration modes primarily correspond to the sail, as the deformations in the booms are consistently 2 to 6 orders of magnitude smaller than those in the sail.

The natural frequencies in the unloaded case are higher than those in the part-level analysis. This may be attributed to the way the sail-boom attachment is modeled, where a larger area of the sail is pinned, effectively increasing its stiffness. For the loaded configuration, the natural frequencies of the sail are higher compared to the part analysis. This is expected, as the higher applied drag pressure increases the sail's tension, resulting in a stiffer structure.

The ratio between the highest drag load natural frequency (1.15E-3 Hz), and the lowest sail natural frequency (0.3017 Hz) is now 201.3, ensuring no resonance between the drag load and the sail. The ratio between the highest natural frequency of the sail (20.932 Hz), and the lowest natural frequency of the less stiff boom (54.1 Hz) is now 2.6, due to the higher drag pressure. The separation between modes is still higher than 2, therefore no mode coupling between the booms and sail is expected.

It is reasonable to conclude that the sail can withstand these higher-pressure drag loads, ensuring the system resists the mechanical loads down to an altitude of 120 km. However, the sail experiences greater out-of-plane deflection due to the increased drag pressure. The highest deflection occurs in the 90 kPa inflation cold case, which corresponds to the maximum drag pressure capable of yielding the boom. This displacement is 1.95 cm, an order of magnitude greater than the previously studied deformation for a drag pressure of 0.085 Pa (160 km altitude). While this deflection may slightly reduce the effective drag area, as discussed in Section 4.2.3, such a reduction at lower altitudes has a negligible impact on the overall decay time.

8.2.4. System at 160 km altitude

At 160 km altitude, the final decay altitude used during the whole study, the pressure applied in the sail due to the drag forces was calculated to be 0.085 Pa. The stress state of the booms at this drag pressure was studied for all the boom cases. Table 8.5 summarizes the results of the highest von Misses stresses in the boom´s inner plane (where the higher stresses are found) at this applied pressure. The residual von Misses stresses in the same location after rigidization are also included in this table.

Table 8.5: Stresses in the boom after deflation and at a 0.085 Pa sail loading for the hot and cold cases.

	Hot Case			Cold Case		
	76 kPa	**92 kPa**	**110 kPa**	**90 kPa**	**110 kPa**	**132 kPa**
Max Stress [MPa]	15.00	25.04	21.56	13.29	29.58	25.30
Stress at deflation [MPa]	14.92	25.04	21.56	13.19	29.59	25.30
Difference [%]	0.562	0.005	0.016	0.698	0.004	0.009

As observed, applying a drag pressure of 0.085 Pa to the sail does not significantly increase the stress in the boom. This is evident as the maximum stress after rigidization (before drag loading) and the maximum stress after 0.085 Pa drag loading on the sail (after rigidization) differ by only 0.7% in the worst case (boom inflation pressure of 90 kPa in the cold case). Therefore, it is clear that the drag load does not pose a structural risk to the system during the decay phase down to an altitude of 160 km, as demonstrated in the part analysis in Section 6.2. Figure 8.15 illustrates the stress distribution for the 90 kPa inflation pressure cold case, both after deflation and under a sail drag load of 0.085 Pa for the full system analysis. No change in the stress distribution is observed, with only a slight increase in magnitude.

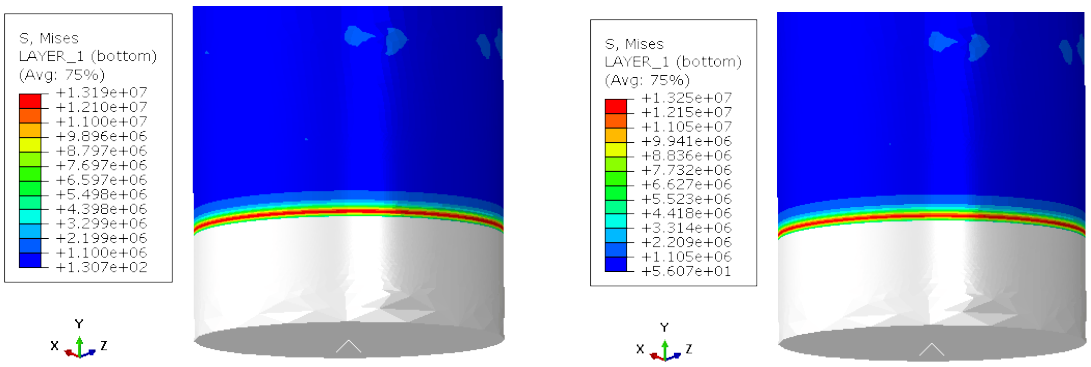

(a) Stress state after deflation.

(b) Stress state after 0.085 Pa load in the sail.

Figure 8.15: Close-up look to the 90 kPa inflation cold case high tress zone. Stresses in Pa.

8.3. Requirements Analysis

Table 8.6 shows the current state of the tender and company requirements after the design decisions made in this study. Each requirement falls under one of these categories:

- **Compliant (C)**. When the requirement is met by the design based on analysis results.
- **Partially Compliant (PC)**. When part of the requirement has been fulfilled, but additional considerations or analyses are needed to fully address the requirement.
- **Non-Compliant (NC)**. When the requirement was not met based on the design or it has not been addressed in the design yet.

Table 8.6: Deorbit System requirements.

ID	Requirement	Status
RS-01	The system shall reduce the deorbit time by a factor of 5 in comparison to the natural orbit decay.	C
RS-02	The maximum decay time shall be 10 years.	C
RS-03	The system shall be designed for an initial altitude range of 450 km to 650 km.	NC
RS-05	The system shall employ an inflatable solution.	C
RS-06	The system shall be designed as simple as possible.	C
RS-07	The system shall have a high level of reliability.	PC
RS-08	The system shall be compatible with volume production requirements.	NC
RS-09	The system shall allow integration within the existing platform.	NC
RS-11	The system shall have a low mass-to-volume ratio.	C
RS-12	The system shall be able to survive micrometeorite impacts.	NC
RS-13	The system shall incorporate a backup passive activation system.	NC
RS-14	The actuation time shall be tuneable commensurate with the mission lifetime.	NC
RC-01	The system shall be able to deorbit 6U and 12U CubeSat.	C
RC-02	The system in stowed configuration shall not be bigger than 1.5U.	PC
RC-03	The system shall maintain the boom radius of the prototype (1.5 cm).	C
RC-04	The system should maintain the boom length of the prototype (30 cm).	C
RC-05	The system should maintain the boom inclination angle of the prototype (50°).	C

* RS-04 and RS-10 were substituted by the company for RC-01.

The use of a drag sail system deployed by inflatable deployable booms complies directly with **RS-05**. Additionally, drag sail and deployable inflatable structures have both high volume-to-mass ratios, complying with **RS-11**.

The orbital decay target time requirements **RS-01** and **RS-02**, are the base of this study. Part I: Orbital Decay, explained the sail sizing procedure from the beginning, ending with a 0.2 m^2 drag sail area that complies with these requirements.

For **RS-03**, it was determined, as discussed in Section 4.1, that a single fixed sail area does not effectively fit in the entire range of initial altitudes. Hence, the system was designed for an initial altitude of 550 km, where the highest concentration of active payloads is found [17]. Not complying with the requirement.

RC-01 is also part of the host spacecraft mission and configuration definition, defined in Section 4.1.

The system was designed for a 12U CubeSat, representing the worst-case scenario. If the 12U configuration meets the decay target, the 6U configuration will comply as well, as it will experience a faster decay.

The inflatable boom design ensured compliance with **RC-03**, **RC-04**, and **RC-05** by maintaining the designed radius, length, and inclination angle required for the deploying mechanism, as detailed in Section 5.

RC-02 was not addressed in this study but it was considered in the deploy mechanism design. This mechanism was designed to fit in a 1.5U enclosure, but structural analysis is needed to confirm that the system can withstand launch loads in its stowed configuration.

The system complies with **RS-06**, which specifies simplicity, by avoiding actuators and complex mechanisms. This contributes to the overall reliability of the design. However, **RS-07**, which focuses on reliability, was only partially met. While the system was analyzed for mechanical environmental loads in its deployed configuration, additional studies are required to evaluate thermal loads and mechanical loads in the stowed configuration during launch.

Several requirements, including **RS-08** (enclosure design), **RS-09** (manufacturability of the deorbit system), and **RS-13** and **RS-14** (activation system), were not analyzed in this study. Similarly, **RS-12**, which addresses micrometeorite impacts on the system, has been noted for future consideration but was not explicitly addressed in this work.

This evaluation demonstrates that while the system addresses key design and decay requirements, further work is needed to fully comply with all considerations.

9

Conclusions and Recommendations

This chapter summarizes the primary conclusions derived from the preliminary sizing and structural design of the drag sail deorbit system. Additionally, it outlines key recommendations for future research, aimed to improve and expand the present work.

9.1. Conclusions

The primary objective of this research was to advance the understanding and application of drag sail systems for CubeSats in Low Earth Orbit, with a specific focus on systems deployed via inflatable structures. The growing accumulation of space debris poses a significant threat to the long-term sustainability of space activities, and drag sail systems present a passive, post-mission disposal solution that utilizes the low atmospheric density in LEO to accelerate the re-entry and disintegration of non-functional satellites.

This research builds upon an initial design developed by Demcon High-tech Systems in response to ESA tender 1-11988 [16]. The aim of this study is to increase the knowledge based on the following question: **How can an inflatable drag sail system be designed to effectively reduce the orbital decay time of CubeSats in Low Earth Orbit while withstanding the mechanical loads throughout the deorbiting phase?**

The two key areas of research derived from this research question included the sizing of the drag sail to reduce the natural decay time of the host spacecraft by a factor of five, addressed in research sub-questions 1 and 2. And the structural analysis of the design to ensure that the system withstands the mechanical loads experienced during orbital decay, addressed in research sub-question 3.

1. How can a numerical model be developed to estimate the orbital decay time of a CubeSat in Low Earth Orbit?

Orbital perturbations can significantly deviate the trajectory of a satellite from its idealized path. For satellites in LEO, the primary sources of these perturbations include conservative forces, such as the Earth's gravitational field (including oblateness effects) and third-body gravitational influences, as well as non-conservative forces, such as atmospheric drag and solar radiation pressure [69]. To account for these effects, a numerical decay model was developed in Python using the Tudat libraries [11]. This model incorporates all relevant perturbations to simulate the satellite's orbital decay. A key assumption in the model is that the stream flow remains perpendicular to the CubeSat's effective drag surface, thereby neglecting lift and side forces.

LEO satellites have natural decay times predominantly determined by atmospheric drag [73]. A critical challenge in modeling orbital decay lies in accurately estimating atmospheric density and the drag coefficient, both of which are sensitive to varying environmental conditions. Regarding the atmospheric density, two models were compared: the US76 neutral atmospheric model and the NRLMSISE-00 dynamic atmospheric model. The US76 model produced an over-conservative decay time estimate of

22.9 years, nearly twice the 12.6 years decay time predicted by the NRLMSISE-00 model.

The aerodynamic flow regime experienced by a satellite varies along its re-entry trajectory. For the current mission, the system remains in the free molecular flow regime down to an altitude of approximately 120 km. The drag coefficient depends on the aerodynamic regime of the CubeSat during decay. Two approaches were analyzed: one using the actual aerodynamic regime and the other assuming a simplified continuum flow regime with a constant drag coefficient (C_d) of 2.2 based on flat plate theory. The difference in decay time between these models was found to be only 4%. This result indicates that an accurate representation of atmospheric density is more critical than a precise drag coefficient model. Atmospheric density can vary by an order of magnitude between different methods, while the drag coefficient varies by only tenths of a unit in this case, making density the dominant factor in orbital decay predictions

Through validation of the model against real decay data obtained from Two-Line Elements (TLE) of three already decayed CubeSats [8], it was found that using the average outer surface area of the CubeSat as the effective drag area offers a conservative yet reliable estimate for decay prediction. Furthermore, the combination of the NRLMSISE-00 atmospheric density model with the rarefied aerodynamic flow regime and the average outer surface area as the effective drag area proved to be the most accurate approach for modeling the CubeSat's orbital decay.

2. How can be the sail area estimated to meet the project's primary requirement of reducing the CubeSat's natural decay time by a factor of five?

The natural decay time of the host spacecraft was estimated to be 31.4 years. The drag sail was sized to meet the tender's primary objective of a fivefold reduction in the host spacecraft's natural decay, to 6.3 years.

To determine the appropriate size of the drag sail, an analysis was conducted based on the relationship between the area-to-mass ratio of the system and orbital decay time. The analysis revealed an exponential relationship between both variables. By fitting a predictive model to the data, incorporating a 2σ confidence interval to account for potential uncertainties in the input parameters and the model itself, an area-to-mass ratio of 54 cm^2/kg complies with the target decay time. It is important to note that this model is specific to the mission's initial conditions and cannot be directly applied to other scenarios.

The resulting area-to-mass ratio of 54 cm^2/kg yielded a drag sail area of 0.2 m². The sail experienced a maximum drag load of 0.01 N at the lowest point in the decay trajectory (160 km altitude). Additionally, the drag profile exhibited an oscillatory trend, which was analyzed to assess the potential for modal coupling between the system and the external aerodynamic loads during decay.

This research did not address the thermal loads resulting from aerodynamic heating, which could reduce the operational lifespan of the drag sail even if it withstands the mechanical stresses. However, the conservative approximation of the area-to-mass ratio ensured that the system would still meet the target decay time even if the sail disintegrated up to an altitude of 360 km. This finding provides an altitude range where sail failure would not compromise compliance with the mission's primary objective. While a detailed thermal analysis was beyond the scope of this work, these results highlight the importance of future investigations into thermal effects during orbital decay, particularly within this altitude window.

3. How can the drag sail and inflatable deployable booms be designed to withstand the mechanical loads during deployment and decay?

The drag sail system analyzed in this research consists of four inflatable deployable booms, each constructed with two independent layers: an aluminum layer providing structural support and an inner Mylar layer serving as a bladder for effective inflation and rigidization. Both independent layers are joined at their ends by aluminum caps. The drag sail, a square thin Mylar fabric, is attached to the top end caps. Two configurations of the sail were studied:

- **Configuration 1**: A simple sail design, where the fabric carries the full drag load.
- **Configuration 2**: A sail design incorporating tension cables across its diagonals to distribute part of the drag load, thereby reducing the load carried by the fabric.

The booms use strain rigidization to maintain their shape and structural properties after gas leakage. Over-pressurization induces plastic deformation in the aluminum layer, increasing the material's yield strength. However, this technique leads to non-uniform rigidization along the boom length, with reduced stiffness near the end-cap connections due to the deformation constraint imposed by the caps. While this creates localized bending flexibility, it does not compromise the design's functionality, as the majority of the boom remains sufficiently rigidized for the mission.

The two configurations were evaluated based on the following criteria: sail deflection and stress, frequency coupling, and the booms' structural performance under drag loads. The structural analysis shows that:

1. **Deflection**: Configuration 2 showed half the out-of-plane deflection of Configuration 1 (0.95 mm vs. 2.12 mm) due to the tension cables bearing part of the load. However, both deflections are negligible, leading to no reduction in the effective drag area or increase in decay time.
2. **Stress**: The stresses in the sail were lower in Configuration 2 because the tension cables reduced the load on the fabric. However, both configurations maintained stresses well below failure thresholds, ensuring sufficient strength to withstand drag loads.
3. **Frequency Coupling**:
    - The separation between the highest natural frequency of the drag force (1.15E-3 Hz) and the lowest natural frequency of the sail exceeded a factor of 200 in both configurations. This large frequency separation eliminates the possibility of resonance between the sail and the drag load.
    - Regarding the interactions between the sail and boom, Configuration 1 had a vibration mode separation of 4.5 times, while Configuration 2 had a separation of 3 times. These separations are sufficient to prevent coupling between the vibration modes of the two subsystems under external loads.
4. **Structural Margins of Safety**: The structural analysis of the boom under axial compression and bending was conducted, following the directions of the forces applied by the sail. Different inflation pressures were also analyzed to determine the most efficient option.
    - *Bending and Axial Compression:* The analysis revealed that bending is the first failure mode of the system. The most critical load in bending was 1.02 N, while the most critical load in axial compression occurred at 24.16 N.

      Regarding the two sail configurations studied, Configuration 1 showed significantly higher MoS for the booms under both, bending and axial compression. For instance, under the worst-case inflation pressure, Configuration 1 had an MoS in bending of 3.23 compared to 0.88 for Configuration 2, while for axial compression, Configuration 1's MoS was more than 2 times that of Configuration 2 (57.8 vs. 24.16).
    - *Inflation Pressure:* Lower inflation pressures improve the bending performance of the boom, making pressures between 76 kPa and 90 kPa suitable for this design. However, higher inflation pressures are more effective at reducing residual creases after rigidization. This analysis assumed that creases were fully eliminated after rigidization, though in practice, some creases may remain reducing the stiffness of the boom.

      Despite this potential stiffness reduction, the design maintains adequate safety margins for bending performance under the lowest inflation pressure; 5.27 for Configuration 1 and 1.78 for Configuration 2 to account for these imperfections. Testing is ultimately required to determine the optimal inflation pressure that balances crease minimization and bending stiffness.

Based on these results, Configuration 1 was selected as the final design. Its simple structure and higher safety margins for the booms make it more robust and reliable for operation in space. While Configuration 2 offers reduced deflection and stresses, these differences are negligible in terms of overall performance. A full system structural analysis of Configuration 1 demonstrated the capability of the drag sail system to survive mechanical drag loads down to an altitude of 120 km. However, the thermal loads resulting from aerodynamic heating, not studied in this research, may reduce the operational lifespan of the system.

The system demonstrates compliance with the key design requirements addressed in this study: orbital decay performance, sail sizing, and structural stress criteria, although further testing is required to fully validate the latter. Some requirements, such as those related to micrometeorite impacts and thermal analysis, remain partially addressed or left for future studies. Overall, the design shows a clear alignment with the mission objectives and provides a solid foundation for future work.

9.2. Recommendations

The following areas can be expanded upon, following the listed recommendations to continue or improve the present work on the drag sail deorbiting system sizing and structural design:

In the area of the orbital decay modeling:

- Develop a more accurate definition of the orbital decay trajectory, considering that the freestream flow is not always perpendicular to the sail surface. This addition to the orbital decay model will result in improved predictions of the drag profile and trajectory by accounting for the influence of side and lift forces during decay.
- Study the system's stability during orbital decay. Determine if the system has passive stability or if an attitude control system will be required to correct the sail´s pointing during decay.
- Developing a more generalized area-to-mass ratio vs decay time model to accommodate a wider range of mission profiles. This approach could be used as a guideline for drag sail system design. Allowing to determine design parameters quickly, without the need for detailed and computationally expensive decay simulations.

In the area of the material properties:

- Testing of coupon samples of the materials used in the drag sail and booms under the different temperature conditions to validate their mechanical properties used for the simulations.
- Analyze the long-term degradation effects caused by the space environment (radiation, micrometeoroids, and atomic oxygen...) on the materials of the drag sail system.

In the area of structural analysis:

- Evaluate the reliability of the deployment mechanism to ensure successful deployment of the drag sail.
- Determine the ideal inflation pressure that balances crease minimization, and ability to withstand bending and buckling loads.
- Incorporate the impact of folding creases into the structural analysis of the booms. This can be achieved through knockdown factors derived from experimental testing or by modeling the creases as geometric imperfections in finite element simulations.
- Design of the origami folding pattern for the boom, containing the lowest number of folding creases near the boom-cap connection, as it is the weakest point in the structure.
- Conduct experimental testing of the final configuration to correlate the results between test data and simulation results.
- Design the drag sail system´s enclosure and stowed configuration layout to withstand the launch loads.

In the area of thermal loads:

- Estimate the thermal loads experienced by the drag sail during orbital decay, mainly the loads resulting from aerodynamic heating. These thermal effects can significantly impact the operational lifespan of the drag sail system.
- This approach can be extended by developing coupled aerothermal-structural analysis. Providing the results from the combined effects of aerodynamic, thermal, and structural loads during the decay.

References

[1] National Aeronautics and Space Administration. *2023 NASA State-of-the-Art Small Spacecraft Technology Report*. Tech. rep. Ames Research Center, Moffett Field, CA 94035-1000, 2023. URL: https://www.nasa.gov/smallsat-institute/sst-soa/structures-materials-and-mechanisms/.

[2] European Space Agency. *CubeSats*. URL: https://www.esa.int/Enabling_Support/Preparing_for_the_Future/Discovery_and_Preparation/CubeSats (visited on 05/12/2024).

[3] Ronald E. Allred et al. "UV Rigidizable Carbon-Reinforced Isogrid Inflatable Booms". In: *Collection of Technical Papers - AIAA/ASME/ASCE/AHS/ASC Structures, Structural Dynamics and Materials Conference*. Vol. 1. 2002, pp. 25–35. URL: https://www.scopus.com/inward/record.uri?eid=2-s2.0-0036072640&partnerID=40&md5=bc502ec26a6d6f2af54be74b59af3759.

[4] Ansys. *Detailed Ansys STK Capabilities*. URL: https://www.ansys.com/content/dam/amp/2023/november/asset-creation/stk-capabilities.pdf.

[5] Yoseph Bar-Cohen. "Transition of EAP Material from Novelty to Practical Applications – Are We There Yet?" In: *Proc SPIE* (Apr. 2001). DOI: 10.1117/12.432639.

[6] Peter Capozzoli, John Insprucker, and Gwynne Shotwell. "The Falcon 9: A New EELV-Class Man-Rated Launch Vehicle". In: *58th International Astronautical Congress 2007*. Vol. 10. 2007, pp. 6667–6674. URL: https://www.scopus.com/inward/record.uri?eid=2-s2.0-54149099976&partnerID=40&md5=e2bd6f4f3a94f2cc2d9a6a405cab39f2.

[7] Tiziana Cardone. "Hyper Velocity Impacts in Space". In: *AE4ASM523 Design of Spacecraft Structures* (2023).

[8] CelesTrak. *CelesTrak Space Data*. 2024. URL: https://celestrak.org/SpaceData/ (visited on 05/24/2024).

[9] Brad Cotten, Ian Bennett, and Robert E. Zee. "On-Orbit Results from the CanX-7 Drag Sail Deorbit Mission". In: *Small Satellite Conference*. 2017. URL: https://digitalcommons.usu.edu/smallsat/2017/all2017/141/.

[10] Dassault Systèmes. *Abaqus 2016 Documentation*. Abaqus Analysis User's Guide, Chapter 10.11, "Plasticity in Ductile Metals". 2016. URL: http://130.149.89.49:2080/v2016/books/gsa/default.htm?startat=ch10s11.html.

[11] Technical University of Delft. *Tudat Space — tudat.space 0.3.1 documentation*. URL: https://docs.tudat.space/en/latest/index.html (visited on 05/12/2024).

[12] DuPont Teijin Films. *DuPont Teijin Films - Mylar polyester film*. 2024. URL: %5Curl%7Bhttps://stenbacka.fi/wp-content/uploads/sites/3/2016/07/mylar_a_fysikaaliset_ominaisuudet.pdf%7D (visited on 08/15/2024).

[13] Dyneema. *The World's Strongest Fiber*. 2024. URL: %5Curl%7Bhttps://www.dyneema.com/%7D (visited on 08/15/2024).

[14] H. L. Eaker. *Significant Electronic Applications and Experimental Results from Project Echo*. Tech. rep. 19660006764. NASA, Nov. 1965. URL: https://ntrs.nasa.gov/citations/19660006764 (visited on 03/25/2024).

[15] eoPortal. *GeneSat-1 Nanosatellite*. Last updated: May 29, 2012. Accessed: 2024-06-15. 2012. URL: %5Curl%7Bhttps://www.eoportal.org/satellite-missions/genesat#references%7D.

[16] ESA. *In-Orbit Experiment of an Inflatable De-Orbiting Drag Device for Small Satellites (ARTES AT 3E.003)*. URL: https://esastar-publication-ext.sso.esa.int/ESATenderActions/details/68199.

[17] ESA Space Debris Office. *ESA's Space Environment Report 2023*. Tech. rep. European Space Agency, 2023. URL: https://www.esa.int/Space_Safety/ESA_s_Space_Environment_Report_2023 (visited on 03/06/2024).

[18] ESA Space Safety. *ESA Commissions World's First Space Debris Removal*. 2019. URL: https://www.esa.int/Space_Safety/Clean_Space/ESA_commissions_world_s_first_space_debris_removal (visited on 03/07/2024).

[19] ESA-ESTEC. *ECSS-E-ST-10-04C Rev.1, Space Engineering Space Environment*. Tech. rep. European Space Agency, 2021.

[20] Requirements & Standards Division ESA-ESTEC. *ECSS-E-ST-10-04C (Space Engineering, Space Environment)*. Tech. rep. Noordwijk, The Netherlands, Nov. 2008.

[21] Requirements & Standards Division ESA-ESTEC. *Structural Factors of Safety for Spaceflight Hardware (ESA Standard ECSS-E-ST-32-10C Rev.2)*. Tech. rep. Noordwijk, The Netherlands, 2019.

[22] T.G. Farr. "The Shuttle Radar Topography Mission". In: *IEEE Aerospace Conference Proceedings*. Vol. 1. 2000, p. 63. URL: https://www.scopus.com/inward/record.uri?eid=2-s2.0-0034432370&partnerID=40&md5=85bedc275c824b1e5baf4924735e07f3.

[23] R.E. Freeland et al. "Large Inflatable Deployable Antenna Flight Experiment Results". In: *Acta Astronautica* 41.4-10 (1997). Cited by: 119, pp. 267–277. DOI: 10.1016/S0094-5765(98)00057-5. URL: https://www.scopus.com/inward/record.uri?eid=2-s2.0-0031200649&doi=10.1016%2fS0094-5765%2898%2900057-5&partnerID=40&md5=2e857c6453f2292b1fbd44da0df7157f.

[24] R.J. Hamann, J. Bouwmeester, and G.F. Brouwer. "Delfi-C3 Preliminary Mission Results". In: *AIAA Small Satellites Conference 2009*. Ed. by s.n. United States: American Institute of Aeronautics and Astronautics Inc. (AIAA), 2009, pp. 1–11.

[25] K. Hart et al. "Analytically-Derived Aerodynamic Force & Moment Coefficients for Resident Space Objects in Free-Molecular Flow". In: *AIAA Atmospheric Flight Mechanics Conference*. 2014. DOI: https://doi.org/10.2514/6.2014-0728.

[26] HDES. *First MINOS Generator Production Batch*. URL: https://hdes.nl/our-projects/first-minos-generator-production-batch/.

[27] A.E. Hoyt et al. ""Rigidization-on-Command"™ (ROC) Resin Development for Lightweight Isogrid Booms with MLI". English. In: *SAE Technical Papers* (2003). ISSN: 0148-7191. DOI: 10.4271/2003-01-2342.

[28] HPS. *ADEO – Deployable Drag Sails for Deorbit*. 2024. URL: https://www.hps-gmbh.com/en/portfolio/adeo-deployable-dragsails/ (visited on 03/11/2024).

[29] Inter-Agency Space Debris Coordination Committee. *IADC Space Debris Mitigation Guidelines*. Tech. rep. IADC, 2020. URL: https://orbitaldebris.jsc.nasa.gov/library/iadc-space-debris-guidelines-revision-2.pdf (visited on 03/06/2024).

[30] S. Ishida and T. Natori. "Regular Folding Pattern Generation for Deployable Nonaxisymmetric Tubes". In: *ASME Design Engineering Technical Conference*. 2014. DOI: 10.1115/DETC2014-34595.

[31] Christopher H. M. Jenkins. *Gossamer Spacecraft: Membrane and Inflatable Structures Technology for Space Applications*. Progress in Astronautics and Aeronautics; v. 191. Reston: American Institute of Aeronautics and Astronautics, 2000. URL: https://public.ebookcentral.proquest.com/choice/publicfullrecord.aspx?p=3111594.

[32] Les Johnson et al. "NanoSail-D: A Solar Sail Demonstration Mission". In: *Acta Astronautica* 68.5–6 (Mar. 2011), pp. 571–575. ISSN: 0094-5765. DOI: 10.1016/J.ACTAASTRO.2010.02.008.

[33] Alicia Johnstone. *CubeSat Design Specification (1U–12U), Rev. 14.1, CP-CDS-R14.1*. Tech. rep. Cal Poly, San Luis Obispo, CA, 2022.

[34] H. Klinkrad. "Methods and Procedures for Re-Entry Predictions at ESA". In: *Proc. 6th European Conference on Space Debris*. ESA SP-723, August 2013. Apr. 2013.

[35] David Lichodziejewski et al. "Development and Ground Testing of a Compactly Stowed Scalable Inflatably Deployed Solar Sail". In: (May 2004). DOI: 10.2514/6.2004-1507.

[36] Sebastien Lienard et al. *Analysis and Ground Testing for Validation of the Inflatable Sunshield in Space (ISIS) Experiment*. Jan. 2000. URL: https://ntrs.nasa.gov/citations/20000033362 (visited on 03/27/2024).

[37] John Lin, Carl Knoll, and Cliff Willey. “Shape Memory Rigidizable Inflatable (RI) Structures for Large Space Systems Applications”. In: 5 (May 2006). DOI: 10.2514/6.2006-1896.

[38] J. W. Martin. *Materials for Engineering*. Third Edition. Cambridge, England: Woodhead Publishing Limited, 2006.

[39] MatWeb. *MatWeb - Material Property Data*. URL: https://www.matweb.com/.

[40] MatWeb. *MatWeb - Material Property Data - Aluminum 1100-O*. 2024. URL: %5Curl%7Bhttps://www.matweb.com/search/datasheet_print.aspx?matguid=db0307742df14c8f817bd8d62207368e%7D (visited on 08/15/2024).

[41] E. Mooij. *AE48870B - Re-entry Systems*. Delft University of Technology, 9.

[42] D. R. Moss and M. Basic. *Pressure Vessel Design Manual*. Fourth Edition. Oxford, UK: Elsevier Inc., 2013. ISBN: 978-0-12-387000-1.

[43] David Mostaza, Ben Graziano, and Peter Roberts. “Spacecraft Drag Modelling”. In: *Progress in Aerospace Sciences* 64 (Jan. 2014), pp. 56–65. DOI: 10.1016/j.paerosci.2013.09.001.

[44] NASA. “Buckling of Thin-Walled Circular Cylinders”. In: *NASA STI Program Report Series* NASA/SP-8007-2020/REV 2 (Dec. 2019).

[45] NASA. *EcAMSAT (OA-8)*. Accessed: 2024-06-15. 2024. URL: %5Curl%7Bhttps://www.nasa.gov/ames/space-biosciences/ecamsat/%7D.

[46] NASA. *General Mission Analysis Tool (GMAT) User’s Guide*. URL: https://ntrs.nasa.gov/api/citations/20080047410/downloads/20080047410.pdf.

[47] NASA. *The Navigation and Ancillary Information Facility*. URL: https://naif.jpl.nasa.gov/naif/data_generic.html.

[48] NASA.gov. *Echo, NASA’s First Communications Satellite*. 2008. URL: https://www.nasa.gov/image-article/echo-nasas-first-communications-satellite/ (visited on 03/25/2024).

[49] William Navidi. *Statistics for Engineers and Scientists*. Fourth Edition. McGraw-Hill Education, 2014.

[50] Keiko Nomura et al. “Tipping Points of Space Debris in Low Earth Orbit”. In: *International Journal of the Commons* 18.1 (2024), pp. 17–31. DOI: 10.5334/ijc.1275. URL: https://www.scopus.com/inward/record.uri?eid=2-s2.0-85183421330&doi=10.5334%2fijc.1275&partnerID=40&md5=187d1e8fed4a838ad0754a38e8ce7cd2.

[51] National Oceanic, National Aeronautics Atmospheric Administration, and United States Air Force Space Administration. *U.S. Standard Atmosphere, 1976*. Tech. rep. NOAA-S/T 76-1562. Washington, D.C., Oct. 1976.

[52] E. Oñate and Bern Kröplin. *Textile Composites and Inflatable Structures*. Computational Methods in Applied Sciences (Springer); v. 3. Dordrecht: Springer, 2005. DOI: 10.1007/1-4020-3317-6. URL: http://site.ebrary.com/id/10140650.

[53] Richard Pappa, John Lassiter, and Brian Ross. “Structural Dynamics Experimental Activities in Ultra-Lightweight and Inflatable Space Structures”. In: 1263 (June 2001). DOI: 10.2514/6.2001-1263.

[54] Sergio Pellegrino and Julian F. V. Vincent. “How to Fold a Membrane”. In: *Deployable Structures*. Ed. by S. Pellegrino. Vienna: Springer Vienna, 2001, pp. 59–75. ISBN: 978-3-7091-2584-7. DOI: 10.1007/978-3-7091-2584-7_4. URL: https://doi.org/10.1007/978-3-7091-2584-7_4.

[55] J M Picone et al. “NRLMSISE-00 empirical model of the atmosphere: Statistical comparisons and scientific issues”. In: *J. Geophys. Res. Space Phys.* 107 (2002). URL: https://doi.org/10.1029/2002JA009430.

[56] K. Ponnapalli and R. D. Falck. “Obtaining Accurate Derivatives Across Adaptive-Step Integration”. In: *AIAA SciTech Forum 2024* (2024). DOI: 10.2514/6.2024-0160.

[57] Singiresu S. Rao. *Mechanical Vibrations*. Fifth Edition. USA: Prentice Hall, Sept. 2009.

[58] Boris V. Rauschenbakh, Michael Yu. Ovchinnikov, and Susan McKenna-Lawlor. *Essential Spaceflight Dynamics and Magnetospherics*. 1st ed. Dordrecht, The Netherlands: Microcosm Press and Kluwer Academic Publishers, 2003.

[59] ROTH. *Aluminum foil ROTILABO, 30 µm, 500 mm, 100 m*. 2024. URL: %5Curl%7Bhttps://www.carlroth.com/nl/nl/folin/aluminiumfolie-rotilabo/p/2596.1%7D (visited on 08/15/2024).

[60] RS Components. *Mylar Plastic Film, 304mm x 200mm x 0.075mm*. 2024. URL: %5Curl%7Bhttps://nl.rs-online.com/web/p/plastic-film/7850795%7D (visited on 08/15/2024).

[61] SAIC. *space-track.org*. Accessed: 2024-05-08. 2024. URL: %5Curl%7Bhttps://www.space-track.org/%7D.

[62] George Sebestyen et al. *Low Earth Orbit Satellite Design*. en. Cham: Springer International Publishing, 2018. DOI: 10.1007/978-3-319-68315-7. URL: http://link.springer.com/10.1007/978-3-319-68315-7 (visited on 05/25/2024).

[63] Zaria Serfontein et al. "Drag augmentation systems for space debris mitigation". In: *Acta Astronautica* 188 (Nov. 2021), pp. 278–288. ISSN: 0094-5765. DOI: 10.1016/J.ACTAASTRO.2021.05.038.

[64] Space Flight Laboratory. *Space Flight Laboratory, Missions: Nanosatellites*. 2023. URL: https://www.utias-sfl.net/canx-7/ (visited on 03/11/2024).

[65] SpaceX. *Starlink*. URL: https://www.starlink.com/ (visited on 05/25/2024).

[66] Dominik Stiller. "Short-term orbital effects of radiation pressure on the Lunar Reconnaissance Orbiter". In: (2023).

[67] K. F. Tapping. "The 10.7 cm solar radio flux (F10.7)". In: *Space Weather* 11.7 (2013), pp. 394–406. DOI: 10.1002/swe.20064. eprint: https://agupubs.onlinelibrary.wiley.com/doi/pdf/10.1002/swe.20064. URL: https://agupubs.onlinelibrary.wiley.com/doi/abs/10.1002/swe.20064.

[68] Craig Underwood et al. *The InflateSail CubeSat Mission – The First European Demonstration of Drag-Sail De-Orbiting*. 2018. DOI: 978-0-87703-647-0.

[69] David A. Vallado. *Fundamentals of Astrodynamics and Applications*. 4th ed. Hawthorne, CA, USA: Microcosm Press, 2013.

[70] Bing Wang et al. "Space Deployable Mechanics: A Review of Structures and Smart Driving". In: *Materials & Design* 237 (2024), p. 112557. ISSN: 0264-1275. DOI: 10.1016/j.matdes.2023.112557. URL: https://www.sciencedirect.com/science/article/pii/S0264127523009735.

[71] Chun H. Wang and L. A. Carlsson. *Failure Criteria, Bonded Joints and Repairs to Composite Airframe Structures*. Elsevier Inc., 2015. DOI: 10.1016/B978-0-12-417153-4.00002-5.

[72] Bruce Yost. "Small Spacecraft Technology, State-of-the-Art". In: *NASA Ames Research Center, Small Spacecraft Systems Virtual Institute* (2024), pp. 369–390.

[73] Haiquan Yu et al. "Simulation of Orbital Decay of LEO Satellites Due to Atmospheric Drag During Magnetic Storms". In: (2022), pp. 1179–1184. DOI: 10.1109/ICUS55513.2022.9986976. URL: http://dx.doi.org/10.1109/ICUS55513.2022.9986976.

[74] Haiquan Yu et al. "Simulation of Orbital Decay of LEO Satellites due to Atmospheric Drag during Magnetic Storms". In: *2022 IEEE International Conference on Unmanned Systems (ICUS)*. 2022, pp. 1179–1184. DOI: 10.1109/ICUS55513.2022.9986976. URL: http://dx.doi.org/10.1109/ICUS55513.2022.9986976.

[75] Norbert Zehentner. "Kinematic orbit positioning applying the raw observation approach to observe time variable gravity". PhD thesis. Jan. 2017. DOI: 10.13140/RG.2.2.33916.33927.

[76] Ruonan Zhang et al. "Overview and Key Technology of the Membrane Drag Sail for Low Earth Orbit Satellite Deorbit". In: *Space: Science & Technology* 4 (2024), p. 0115. DOI: 10.34133/space.0115. eprint: https://spj.science.org/doi/pdf/10.34133/space.0115. URL: https://spj.science.org/doi/abs/10.34133/space.0115.

A

NRLMSISE-00 Data Adaptation

The F10.7 parameter measures the strength of solar radio emission in a 100 MHz-wide band centered on 2800 MHz, wavelength of 10.7 cm, averaged over an hour [67]. The F10.7 OBS (Observed) parameter refers to the direct measurement from a ground-based station, while the F10.7 ADJ (Adjusted) calibrates the observed value to represent the F10.7 parameter at a distance of 1AU, eliminating the variation in the distance Earth-Sun because of the orbit's eccentricity.

Figure A.1 presents the solar flux F10.7 OBS parameter values obtained from Celestrack [8], covering the period from 1957 to the present day, along with projections of this parameter up to 2041. The 11-year solar cycle is visible in this dataset.

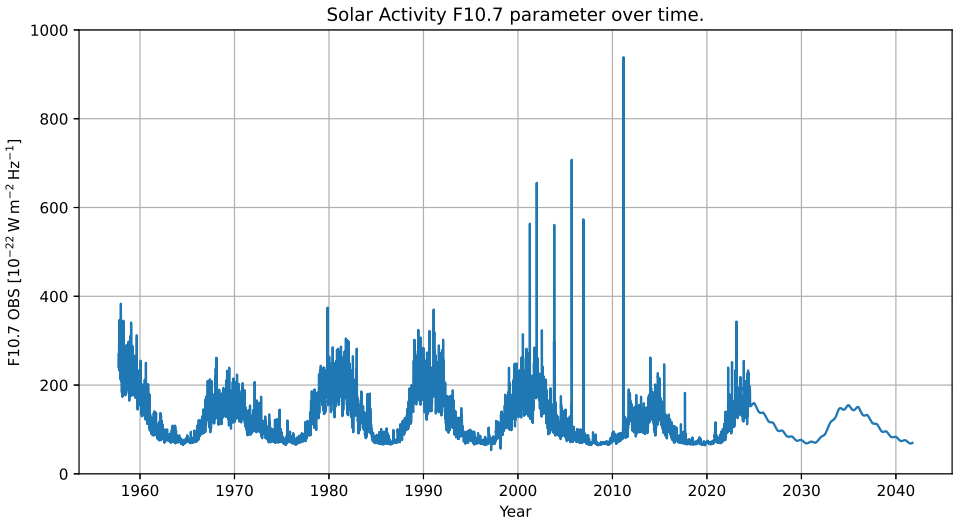

Figure A.1: F10.7 OBS parameter distribution over time [8].

When the Celestrack data was directly incorporated into the orbital decay model, the simulation terminated on May 4, 2001. As shown in Figure A.1, a significant peak in solar flux is observed at this point. Similar unexpected peaks in solar flux F10.7 ADJ parameter were observed. These sudden increases in solar activity likely led to rapid rises in atmospheric density, causing instability in the model and divergence of the solver. Consequently, these peaks were identified as outliers.

The standard score, or Z-score, method was employed to detect these outliers. The Z-score measures the number of standard deviations a given data point is from the mean of the dataset. The Z-score for each data point is calculated using Equation A.1 [49]:

$$Z = \frac{Y_i - \bar{Y}}{\sigma} \tag{A.1}$$

where Y_i represents the solar flux value, $\bar{Y}$ is the mean of the dataset and σ is the standard deviation.

This method identifies outliers by defining a Z-score threshold, beyond which data points are considered outliers. A common threshold used is 3, which includes 99.7% of the data in a normal distribution. However, due to the greater variability in solar activity, a threshold of 5 was selected for this analysis. Figure A.2 illustrates the outliers identified based on this criterion for the F10.7 OBS parameter, the same procedure was done for the F10.7 ADJ parameter.

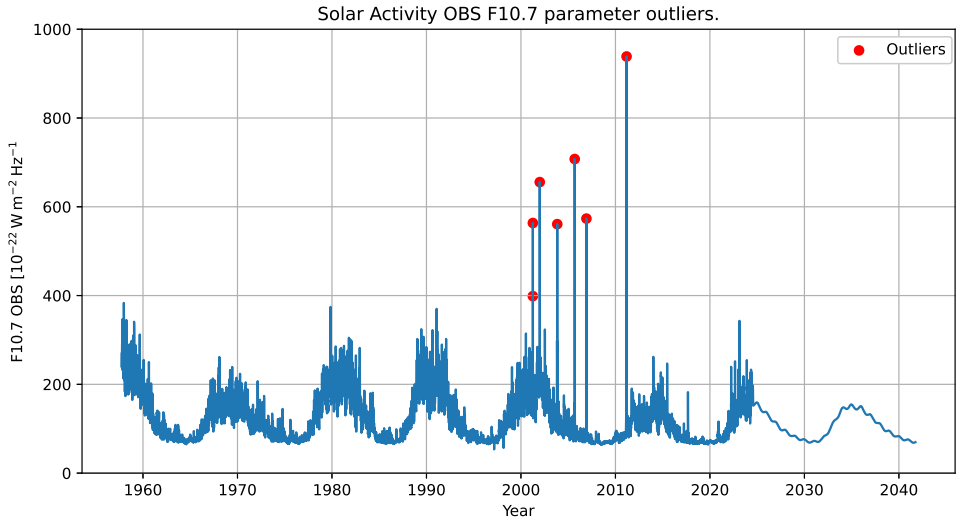

Figure A.2: Outliers with a Z-score over 5 for the F10.7 OBS parameter.

The outlier values were subsequently replaced with the average of the preceding and succeeding data points, yielding the final F10.7 OBS distribution, shown in Figure A.3. This new dataset did not cause divergence in the orbital decay model.

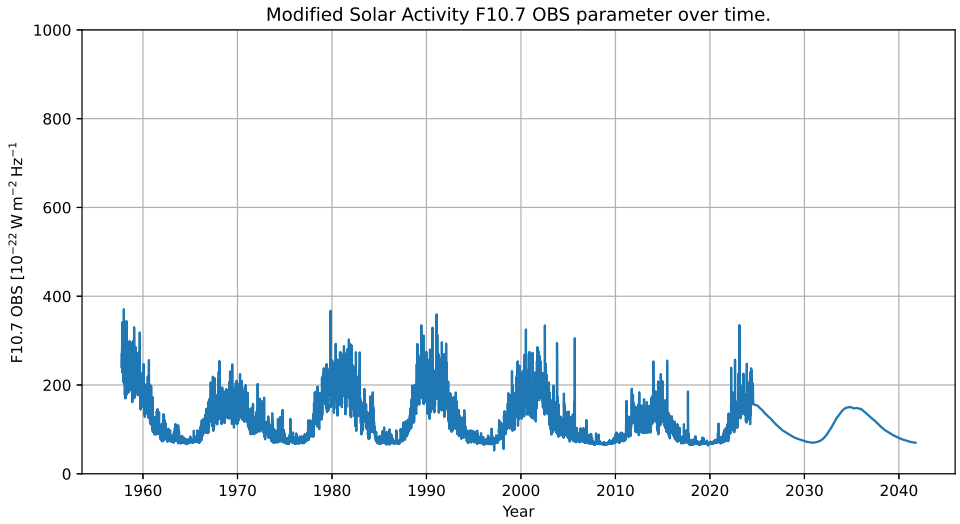

Figure A.3: Modified F10.7 OBS parameter distribution over time.

B

Detailed Explanation of the Reaction Forces in the Sail

This Appendix shows the direction of the applied forces in the boom in more detail. Figure B.1 illustrates the applied forces in the boom in the sail´s coordinate system, which corresponds to the global coordinate system of the model. Because of the double symmetry in the design, the R_x and R_y components have the same magnitude, therefore the resultant of these forces will be along the diagonal of the sail. The plane shown in blue is the plane that cuts the system along the diagonal of the sail.

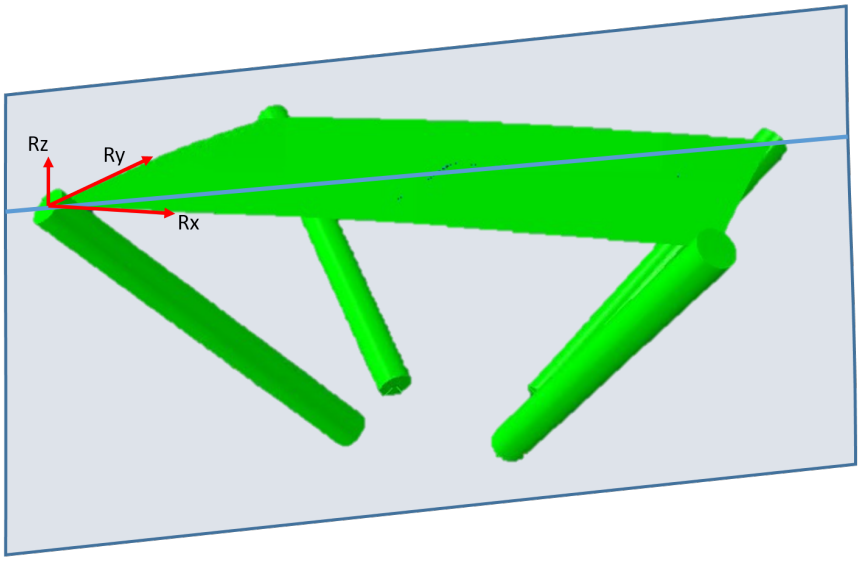

Figure B.1: Applied loads in the boom. Full system view.

Figure B.2 presents the sectional view obtained along the blue cutting plane defined in the previous figure. As the cutting plane goes through the diagonal of the sail, the force components can be simplified in a horizontal force, which is the resultant from R_x and R_y and the vertical force corresponding to R_z.

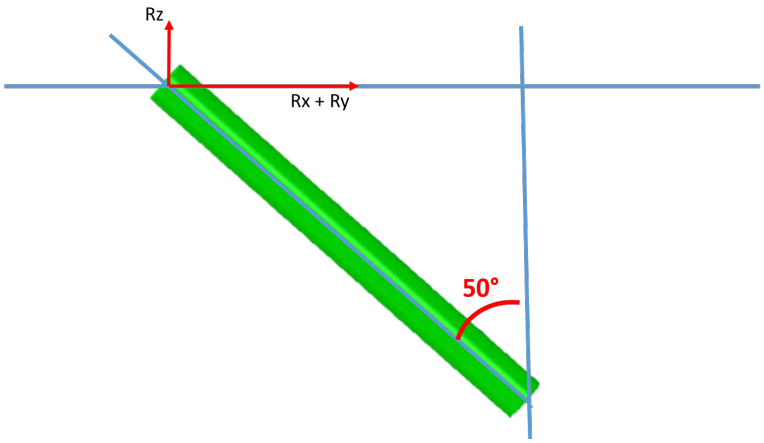

Figure B.2: Applied loads in the boom. Sectional view.

The sectional view in Figure B.3 shows the resultant force in the sail´s coordinate system in red, and the components of this force in the boom´s coordinate system in black.

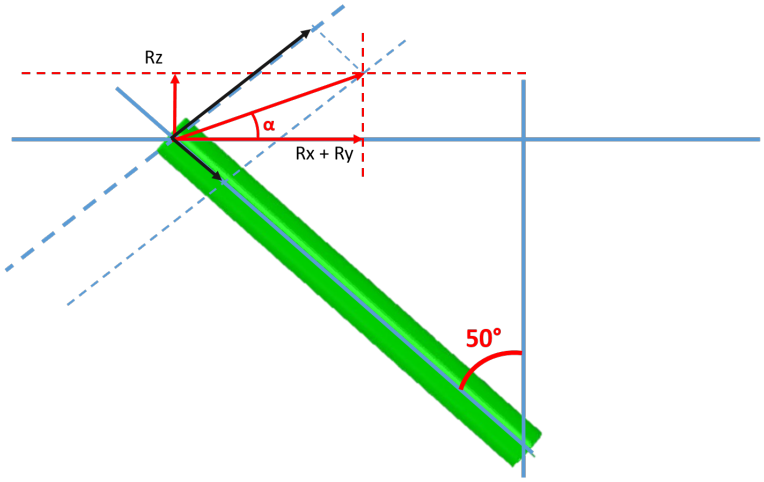

Figure B.3: Resultant applied force in the sail´s coordinate system its vertical and horizontal components in the boom´s coordinate system.

The criteria to determine if the vertical force in the boom´s coordinate system will be in tension or compression is defined in Equation B.1.

$$\delta = \arctan(\frac{R_z}{R_x + R_y}) \tag{B.1}$$

if $\delta > 50°$ compression

if $\delta < 50°$ tension

For Configuration 1 in the full system model and the sail model, these values are $\delta = 1.4$ and $\delta = 1.2$ respectively. Analogously for Configuration 2, these values are $\delta = 1.3$ and $\delta = 1.3$ respectively. Therefore in all configurations, the vertical force applied to the boom in the boom´s coordinate system is in compression.

The negative vertical component of $R_x + R_y$ in the boom´s coordinate system is greater than the positive vertical component of R_z in the boom's coordinate system. This is the reason why the overall vertical force in the boom´s coordinate system is in compression.

C

Re-design of the Boom to Strengthen the Design

The most structurally demanding study case is the boom´s inflation pressure of 1.25 times the yield pressure under the hot case condition. This case was chosen to study the redesign of a stronger boom. Five redesign options were analyzed:

1. **Decreasing the length of the boom.** Shortening the boom will reduce the bending moment applied by the load, therefore increasing its stiffness in bending. Shortening the boom does not directly impact its resistance in shell buckling, but a shorter boom will result in fewer folding creases and imperfections.
2. **Use 3003 aluminum alloy.** This alloy is ductile enough to produce thin film layers while having a higher yield strength. A higher yield strength will directly improve the boom's capacity to withstand bending and compressive loads, increasing the maximum load the material can withstand before reaching the yield point.
3. **Increase the thickness of the cross-section.** Increasing the thickness of the boom increases the second moment of area (moment of inertia), thus increasing the bending stiffness and raising the load-bearing capabilities of the boom in compression.
4. **Increasing the boom radius**. As was the case with the increased thickness, increasing the outer radius of the boom will increase the moment of inertia, allowing for higher loads in bending and compression before yielding.
5. **Stiffener using shape memory materials.** To enhance the structural integrity of the boom, a helicoidal stiffener made from shape memory materials (SMMs) could be embedded along its length. This stiffener would remain compact during stowage, and deploy in response to specific environmental triggers, such as temperature or UV radiation. The deployment of these SMMs alongside the inflation of the boom allows for an increase in stiffness when the boom reaches its operational state.

Of the five design options outlined, only the first three were modeled and studied. Option four was excluded because Requirement RC-03 specifies that the boom must retain the radius of the initial prototype, a constraint driven by the design of the deployment mechanism. Additionally, Requirement RC-02 states that the system, in its stowed configuration, must not exceed a volume of 1.5U. Thus, even if RC-03 was disregarded, significantly increasing the boom radius could prevent the structure from fitting within the specified enclosure. Requirement RC-04 states that the boom's length and inclination angle should match those of the prototype, though these parameters allow for some degree of modification.

Option five was initially set aside due to the complexities involved in designing the stiffener. A well-characterized temperature profile of the mission environment is needed to ensure that the shape memory material activates only during deployment. Unintentional activation during the stowed configuration

could pose significant risks to the CubeSat's mission. Additionally, testing of the deployment speed of the shape memory structure will be needed to ensure it does not damage the aluminum layer during deployment.

Thus a reduction of the length of the boom to 0.25 m (L =0.25 m), a new aluminum alloy Al3003 (Al3003) with higher yield strength, and an increase in the aluminum thickness of 1.5 times the initial thickness (1.5t) were studied. Tables C.1 and C.2 provide the MoS of the applied bending and compression loads for the three redesign options under the hot case scenario, for a 1.25 P_y inflation pressure.

For the options involving the new material with enhanced yield strength and the increased thickness of the boom, the yield pressure was recalculated following Equation 5.5. For the 3003 aluminum alloy boom $P_y = 88$ kPa, and for the boom with a thickness 1.5 times that of the initial design $P_y = 111$ kPa. Consequently, the study inflation pressures for these two cases are 110 kPa and 139 kPa, respectively, representing 1.25 times the recalculated yield pressures. The shorter boom, however, did not require a recalculation of the yield pressure.

Table C.1: Margins of Safety of the three stronger boom cases for the worst case scenario under bending.

	1.5t	**Al3003**	**L = 0.25 m**
	139 kPa	**110 kPa**	**92 kPa**
P_B **[N]**	1.505	1.225	1.19
P_{BH} **[N]**	3.06	2.41	2.39
Drag force in-plane Conf.1 [N]	0.24		0.16*
Drag force in-plane Conf.2 [N]	0.54		0.36*
MoS P_B **Conf.1**	5.27	4.10	6.44
MoS P_{BH} **Conf.1**	11.76	9.03	13.94
MoS P_B **Conf.2**	1.79	1.27	2.31
MoS P_{BH} **Conf.2**	4.67	3.46	5.63

Table C.2: Margins of Safety of the three stronger boom cases for the worst case scenario under axial compression.

	1.5t	**Al3003**	**L = 0.25 m**
	139 kPa	**110 kPa**	**92 kPa**
P_{SB} **(I) [N]**	36.48	29.54	24.42
Drag force out-of-plane Conf.1 [N]	0.28		0.33*
Drag force out-of-plane Conf.2 [N]	0.63		0.75*
MoS P_{SB} **(I) Conf.1**	129.27	104.50	73.01
MoS P_{SB} **(I) Conf.2**	56.90	45.89	31.56

* The 0.25 m boom case has an angle w.r.t. the vertical of 65°, thus the change in the applied drag load.

Table C.3 shows the first natural frequency of the three stronger booms.

Table C.3: Margins of Safety of the six boom cases studied under the axial compression drag loads for the two sail configurations.

	1.5t	**Al3003**	**L = 0.25 m**
	139 kPa	**110 kPa**	**92 kPa**
Natural Frequency [Hz]	67.88	54.77	72.57

C.1. Trade-off

All redesign cases have a wider MoS to account for the not modeled creases on the boom that can reduce its local stiffness, therefore a trade-off of the 3 designs was performed to determine the best redesign option. The requirements analyzed, how they will be scored and their weight in the final design decision are:

- **MoS in Bending Analysis:** Increasing the bending MoS is crucial for structural reliability, as a higher MoS indicates the structure can withstand greater loads before yielding. Scoring criteria are as follows: a score of 3 if the MoS is within the range [3-2], 2 if it is within the range [2-1], and 1 if it is lower than 1. This requirement has a weight of 30% in the trade-off, as it addresses the primary reason for structural concerns in the boom.
- **Mass Increase:** Minimizing mass is critical in space applications. This criterion will score 3 if the mass increase is less than 1%, 2 if the increase is under 5%, and 1 if the increase is below 10%. This requirement has a weight of 20%, although a minimal increase in the boom´s weight is expected in the three redesign options.
- **Manufacturability:** This criterion assesses the feasibility of manufacturing changes compared to the prototype. A score of 3 indicates manufacturability equal to or easier than the prototype, 2 indicates moderately more complex manufacturing, and 1 indicates significantly higher complexity. This requirement holds a 10% weight, as the manufacturing process will likely undergo refinement after finalizing the design.
- **Stiffness and Dynamic Behavior (S and D):** Improved stiffness will reduce vibrations and oscillations, even though the boom will primarily remain static after deployment. The scoring is as follows: 3 if the first natural frequency increases between 20% and 50%, 2 if it increases between 0% and 20% and 1 if the natural frequency decreases from the original design. This requirement has a weight of 10%, considering that the original design already demonstrated adequate dynamic performance, avoiding coupling with sail modes.
- **Compatibility with Deployment Mechanism:** This criterion evaluates the new design's integration with the existing deployment mechanism. It scores 3 if no changes to the deployment mechanism are required, 2 if only minor modifications are needed, and 1 if a full redesign is necessary. This requirement is weighted at 30%, reflecting its critical importance to the company's specifications.

Table C.4: Trade-off of the strengthening boom redesign options.

	1.5 t	**Al3003**	**L=0.25 m**
MoS P_B	1.79	1.27	2.31
Score	2	2	3
Mass	4.16E-2	4.09E-2	4.01E-2
% w.r.t. original	1.03	1.01	0.99
Score	3	3	3
Manufacturability (Score)	3	3	3
S and D (Score)	67.88	54.77	72.75
% w.r.t. original	17.54	-5.16	25.65
Score	2	1	3
Integration (Score)	3	3	1
Total Score	**3.3**	**2.4**	**2.7**

Table C.4 presents the results of the trade-off analysis, with **the increase in thickness selected as the preferred option for redesigning the boom**. This option can also be further iterated if additional strength is required, up to the limit at which the boom folding remains feasible.